NTNU

Norwegian University of
Science and Technology

Control of Offshore Passive Platform System Voltage and Frequency through Control of Onshore Back-to-Back Voltage Source Converters

Kristin Malene Høvik

Master of Science in Energy and Environment

Submission date: June 2011

Supervisor: Tore Marvin Undeland, ELKRAFT

Co-supervisor: Jan Arild Wiik, ABB Oil, Gas and Petrochemicals, Department of Strategic R&D

Temesgen Haileselassie, ELKRAFT

Norwegian University of Science and Technology
Department of Electric Power Engineering

Problem Description

In 2009, the petroleum industry was responsible for 26% of the total CO_2 and NO_x emissions in Norway. 90% of these emissions were due to power production. A reduction of these emissions would greatly decrease the total emissions of the country. One of the suggested solutions for reducing the emissions of offshore platforms is to supply them with electricity from shore.

This thesis work should be focused on study of available control methods to ensure proper passive system control so that the need of a gas turbine on oil platforms can be significantly reduced. A control system for the full back-to-back voltage source converter configuration should be implemented, tuned and tested for worst-case load changes on the passive platform system.

Assignment given January 17th, 2011
Professor Tore Undeland

Preface

This master thesis documents my work during the spring semester of the 5th and final year of my master study in Energy and Environmental Engineering, at Norwegian University of Science and Technology (NTNU) in Trondheim. The master thesis was initiated by ABB Oil, Gas and Petrochemicals, Department of Electrical Systems.

This semester has been very valuable for me. My thesis work has challenged me in many ways and it has prepared me for new challenges in my future work in this field.

Due to the wide scope of this thesis, the report has not been focused on providing long derivations of equations and principles found in other literature. Citations for where the full derivations are found are provided throughout the thesis.

MATLAB® Simulink™ SimPowerSystems™ was used for all modeling and simulations in this thesis work. Running the full system simulations on the NTNU server with the only SimPowerSystems license available has been a challenge, due to very long simulation times. This has limited the amount of simulations and testing that could be done in the time available for the master thesis work. Future work with the SimPowerSystems™ models is suggested to be done on a server with a faster processor.

Many people have contributed to this thesis work with help, support, and encouragement. I would first like to express my gratitude to my main adviser, Professor Tore Undeland for giving me the opportunity to work on a master thesis in the field of power electronics. It has been an honor to be his master student. My co-adviser, Temesgen Haileselassie deserves my sincere thanks for all the help he has given me, even in the evenings when he was getting ready to leave for home. I would also like to express my sincere gratitude to Raymundo Torres Olguin, for all the help and advice he has given me throughout my research. His support has been invaluable.

I would also like to thank my adviser at ABB Strategic R&D for Oil, Gas and Petrochemicals, Dr.Eng Jan Wiik that has used time from his already hectic schedule to help me with my thesis.

I could not have submitted this thesis without the help of my dear friend, Eric Severson. He has inspired me to work harder and I am very grateful for the time he used to proof read my thesis. My fellow master students have created a good working environment. I am also very grateful for the encouragement of my parents and sisters. At last I want to thank my fiancé Jan Kristian Bjerke, without whom I could not have done this. He has always been available for long phone calls discussing my system, providing encouragement, and ideas.

Trondheim, 13.06.2011
Kristin Malene Høvik

Summary

This thesis work shows implementation and testing of existing control strategies in a novel offshore passive platform configuration. Control of the platform voltage and frequency is done through control of a shore-based back-to-back voltage source converter configuration, when the frequency on shore differs from the frequency on the platform. An 80 km HVAC-cable and transformers separates the shore-based back-to-back voltage source converters from the platform installation. The system is modeled and simulated in MATLAB® Simulink™ SimPowerSystems™.

The grid-side voltage source converter is applied conventional cascaded controllers, with an inner current control loop and outer loops controlling the DC-link voltage and the flow of reactive power from the grid.

Two different control strategies were implemented for the platform-side voltage source converter, denoted as control strategy 1 and 2. Control strategy 1 controls the platform voltage magnitude, while keeping the frequency fixed, and is implemented with a simple PI-controller. Control strategy 2 controls both platform voltage magnitude and frequency, and was based on a cascaded control configuration, similar to that of a weak-grid system, implemented for the passive platform system.

Both control strategies were implemented for the platform system and tested for three worst-case changes of platform load: loss of all loads, increase of passive load and large induction motor starting. The platform steady-state and transient voltages and frequency were evaluated based on the requirements for voltage and frequency defined in IEC 61892: standard for mobile and fixed offshore units, electrical installations.

Control strategy 1 was tested for both normal and autonomous operation, when a constant DC-link voltage was applied. It was also tested for full back-to-back voltage source converter configuration, with the grid-side system converter controlling the DC-link voltage and flow of reactive current from the grid. In all the three configurations, control strategy 1 failed to meet the system requirements set by the IEC 61892 standard for allowable voltage magnitude transients during loss-of-all-load and large-induction-motor-start.

Control strategy 2 was tested with constant DC-link voltage when platform voltage measurements were available. The simulation results show no visible voltage or frequency transients for any of the three load change tests applied, and the system operation satisfies the IEC 61892 requirements for all the worst-case load change tests. The platform voltage and frequency are independent of the load dynamics, which is a desirable quality when controlling the voltage on a complex platform configuration. Control strategy 2 shows promising potential for controlling the platform voltage and frequency from shore. However, further research and testing must be done before this control strategy can be utilized in a real platform system.

The proposed system controlled by control strategy 2 would allow significantly reducing the usage of low efficiency, high emission gas turbine driven synchronous generator that are the standard power source on oil platforms today. Reducing the usage of the gas turbine, for power production on offshore oil and gas platforms, could reduce the total CO_2 and NO_x emissions of the petroleum sector considerably.

Sammendrag

Denne masteroppgaven viser implementering og testing av to eksisterende kontrollsystemer, i en ny passiv plattformkonfigurasjon. Kontroll av platformspenning og -frekvens ble gjort gjennom kontroll av en en landbasert "back-to-back" VSC konfigurasjon, som forsyner en offshore plattform med kraft fra land, gjennom en 80 km HVAC-kabel. Frekvensen på land er ulik frekvensen på plattformen. Systemet er modellert og simulert i MATLAB® Simulink™ SimPowerSystems™.

Omformeren i B2B-konfigurasjonen som blir forsynt med kraft fra nettet ble implementert med kaskadekontrollere for å kontrollere DC-linkspenningen og reaktiv effektflyt fra nettet.

To kontrollmetoder ble implementert for omformeren på plattformsiden av den landbaserte B2B-VSC konfigurasjonen, og angis som kontrollstrategi 1 og 2.

Kontrollstrategi 1 kontrollerer RMS-spenningen på plattformen, og holder frekvensen konstant. Strategien er implementert ved hjelp av en enkel PI-kontroller. Kontrollstrategi 2 kontrollerer både RMS-spenningen og frekvens på plattformen. Denne kontrollmetoden er basert på en kaskadekontroll, lik konvensjonell kaskadekontroll implementert for svake nett.

Begge kontrollstrategiene ble implementert for plattformsystemet og tested for tre "worst-case" lastendringer: tap av all last, økning i passiv last og direkte start av stor induksjonsmotor. De resulterende platformspenning- og frekvenstransientene ble evaluert basert på krav til spenning og frekvens definert i IEC 61892: "Standard for mobile og stasjonære offshore enheter, elektriske installasjoner".

Kontrollstrategi 1 ble tested for både normal og autonom operasjon, når konstant DC-link spenning ble påtrykt. Strategien ble også tested for det fulle "back-to-back" VSC-systemet. Kontrollstrategien greier ikke å regulere plattform spenningen innenfor de grensene som er satt av plattformsystemkravene for alle lastendringstestene.

Kontrollstrategi 2 ble testet for konstant DC-linkspenning, når målinger av plattformspenningen var tilgjengelige. Simuleringene viser at verken platformspenningen eller frekvensen blir påvirket av de store lastendringene på plattformen, og at kontrollsystemet tilfredstiller IEC 61892 kravene for spenning og frekvens for alle lastendringstestene. Plattformspenningen og -frekvensen er uavhengig av lastdynamikken, noe som er en svært god egenskap for offshore installasjoner som ofte har kompleks last. Kontrollstrategi 2 viser basert på dette stort potensiale for kontroll av plattformspenning og frekvens fra land. Implementering av kontrollstrategien i et ekte system krever derimot mer forskning.

Systemet foreslått i denne masteroppgaven, med kontrollstrategi 2 implementert, vil gjøre redusert bruk av den konvensjonelle gassturbinen på offshore plattformer, med lav virkningsgrad og høye utslipp, mulig. Redusert bruk av gassturbiner for kraftproduksjon på plattformer kan redusere de totale utslppene av CO_2 og NO_x fra petroleumssektoren.

Contents

List of Tables

List of Figures

1 Introduction

1.1 Electrification of Offshore Oil and Gas Installations

In 2009, the petroleum industry was responsible for 26% of the total CO_2 and NO_x emissions in Norway [1]. 90% of these emissions were due to power production [2]. A reduction of these emissions would greatly decrease the total emissions of the country. This is needed as Norway has made a commitment, through the European Union, to reduce emissions by 20% by year 2020 [3].

One of the suggested solutions for reducing the emissions of offshore platforms is to supply them with electricity from shore [1]. The Norwegian Government imposed a tax on CO_2 and NO_x emissions for the petroleum industry in January 1991 [2]. This tax is designed to make electrification of offshore oil platforms more economically feasible. In February 1996, the Norwegian government voted to require that all new oil field development plans provide an analysis of powering the proposed installations. This overview must compare the two cases: 1) where all energy requirements are met with power from shore; 2) where all energy requirements are met with generators powered by gas turbines on the platform. The variables to be compared in each case are the generation efficiency and the costs required [1].

Several platforms on the Norwegian continental shelf have been powered from shore since this law came into action. Below are several examples:

The Troll A platform was the first offshore platform on the Norwegian continental shelf to be powered from shore. It is situated 65 km from shore and is powered through an HVAC-cable with a transmission capability of 17.5 MW and a transmission voltage of 52 kV-AC [4]. In 2005, two additional HVDC-cables, each with a transmission capability of 40 MW, were added to supply the Troll A platform [5]. This was implemented with HVDC Light™, a VSC-HVDC technology patented by ABB [6].

The Ormen Lange gas field, located 120 km off the coast of Norway, consists of subsea located equipment only [7]. The field was supplied with power from shore through a long step-out power supply of 65 MW, and with a rated voltage of 120 kV-AC. A subsea mounted variable speed drive (VSD) keeps the voltage variations and stability of the power supply system at an acceptable level and supplies subsea equipment as compressors and pumps [8].

The Valhall field, situated 292 km south-west from the coast of Norway was, due to its large distance from shore, powered through a HVDC-cable with a voltage level of 150 kV-DC and a transfer capability of 78 MW. The VSC-station was

placed on a new platform and is powering the 6 platforms in the Valhall field. This system was ready for commercial operation in 2010 [9], and the HVDC-technology used was HVDC Light™.

The Gjøa field, located 100 km from shore, contains a semisubmersible platform which is powered through a HVAC-cable, with a transfer capability of 40 MW. This field has been in commercial operation since 2010.

The Goliat field, situated about 100 km from shore, is planned to contain a floating oil platform for production, and will also be supplied through an HVAC-cable [10].

The financial profitability and the positive environmental consequences of supplying offshore platforms with power from shore have been debated. In [11] it is stated that the costs of supplying offshore platforms with power from shore are, for most projects, significantly larger than the cost of the CO_2-tax imposed.

A reduction in CO_2 - and NO_x –emissions depends on how the supplied power is produced. It is commonly understood that supplying the offshore platforms with Norwegian hydropower is unrealistic, which means that the oil platforms could be supplied with imported power from coal power plants. To make electrification of offshore platforms beneficial to the environment, the platforms should be supplied with power produced from renewable energy sources or efficient gas power plants [11].

The financial profitability for electrification of offshore platforms is not dependent on the CO_2-tax cost exclusively. The gas that was previously used as fuel is made available for processing and sale, or for reinjection to increase oil production [4]. In addition to this the gas turbines supplying the platforms tend to need frequent maintenance, which imposes large maintenance costs.

In 2003-2004, platforms in the Saudi Arabian oil field Abu Safah was powered through an HVAC-cable of 50 km, with a transfer capability of 100 MVA, and a voltage level of 115 kV-AC [10] [12]. The Qatar Petroleum owned PS4-platform and the gas processing plant on Halul island is going to be powered from an HVAC-cable and a HVDC-system respectively [9]. The operators of these platforms are not influenced by the Norwegian Government imposed taxes, and powering the platforms from shore was profitable despite this.

Several challenges must be overcome before power from shore will be advantageous for all offshore platforms, both financially and environmentally. This makes research on this topic, both to develop new technologies and to improve available technologies, very important and forms the basis of the research done in this master thesis work.

1.2 Available Technologies for Powering Offshore Installations with Power from Shore

As seen in section 1.1, there are two main technologies used for power transmission to offshore installations; HVDC and HVAC. The technology that is

chosen for a particular project depends on the distance from shore, required power transmission capability, space available on the platform and the estimated costs for each of the technologies.

HVDC systems consist of an AC to DC converter, feeding DC power into a cable, and a converter at the end of the cable, transforming from DC- to AC- power. Two technologies are available for converting AC to DC or DC to AC; line commutated current source converters (LCC/CSC) or voltage source converters (VSC). HVDC in combination with line commutated converters or thyristor converters is referred to as "conventional HVDC" or "HVDC Classic" [13]. HVDC in combination with VSC is generally referred to as VSC-HVDC, HVDC Light™ or HVDC PLUS™ [6, 14].

Space and total weight of offshore oil and gas installations is limited. In the Norwegian petroleum industry a rule of thumb for fixed platforms has been that 1 tonne of equipment requires 10 tonnes of construction material for support [4]. The relation for floating installations can be higher [4]. Equipment used on offshore oil platforms therefore needs to be light weight and compact. The LCC introduces large amounts of harmonics and consumes reactive power. Due to this, it needs large and heavy filters and reactive power compensators. Therefore this is not a desirable solution for offshore platforms.

The VSC consists of forced commutated switches; devices for which turn-on and turn-off can be controlled. It uses pulse width modulation (PWM) to modulate the wanted voltage magnitude and phase angle of the output voltage, and hence has two degrees of freedom for control [15]. It allows independent and fast control of active and reactive power, and does not need any reactive power compensation device. The transistors used depend on the required power rating. For applications as of those studied in this thesis, insulated gate bipolar transistors (IGBTs) could be used [16]. The VSC introduces very little harmonics and does not need large filters, it is compact and light weight, and it can feed weak or passive grid systems. All of these qualities make it a good candidate for powering offshore installations [6]. The VSC-HVDC technology is therefore the only HVDC-technology that has been used for electrification of offshore platforms. The drawbacks of the VSC are that the transistors have lower power rating than the thyristors used in the CSC, and are more expensive. The power losses are also larger than for the CSC because of high switching frequency [16].

A VSC-HVDC scheme for powering an offshore platform with power from shore is shown in Figure 1-1. The transmission system is isolated from the platform grid and the onshore grid due to the VSCs, this eliminates a need for synchronization of the systems. The HVDC-cable, transmitting the DC power to the platform, always operates at unity power factor since there is no production or transmission of reactive power. The distance of power transmission is not limited by any power stability limit, and hence the power can be transmitted over long distances [17].

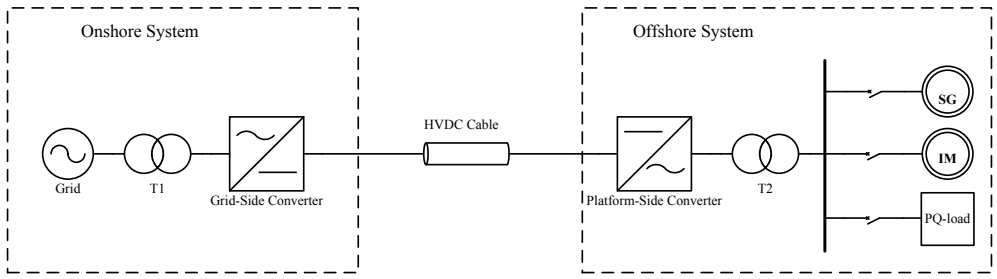

Figure 1-1 VSC-HVDC configuration for electrification of offshore installations

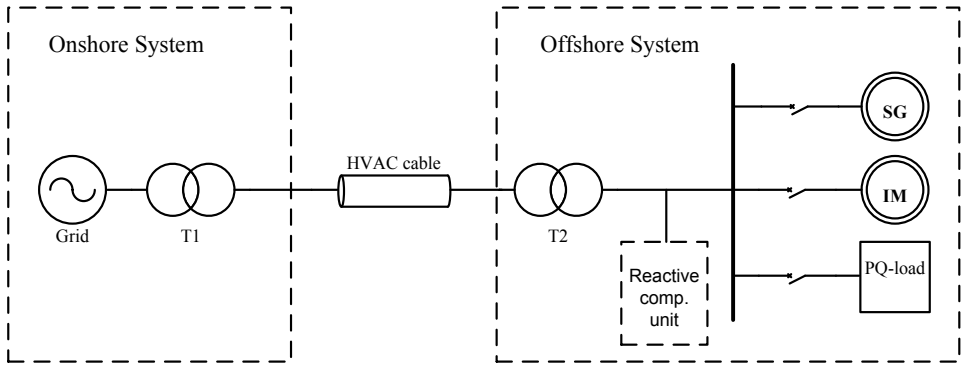

Figure 1-2 HVAC configuration for electrification of offshore installation

HVAC transmission has also been used for powering offshore installations, and a possible HVAC-system configuration for powering an offshore platform with electricity from shore is shown Figure 1-2. The HVAC configuration usually consists of transformers on each end of the cable, and some reactive power compensation device. HVAC cables produce and transmit reactive power, have skin effect that contributes to losses, and a stability limit that is inversely proportional to the length of the line [17]. Transmission length and power rating are factors that will limit the possibilities for usage of HVAC transmission. Developments in cable technology have increased both the power transmission capability and the feasible lengths of transmission for HVAC [18] and is shifting the "break-even costs"-crossing between the HVAC and the HVDC technologies.

From the platform electrifications presented in section 1.1 it can be seen that HVAC has been used for distances up to 120 km [8], and for power ratings up to 100 MVA [12]. VSC-HVDC, for powering offshore platforms, has been used for distances up to ~300 km [9], and for power ratings up to 300 MW [6].

1.3 System Description

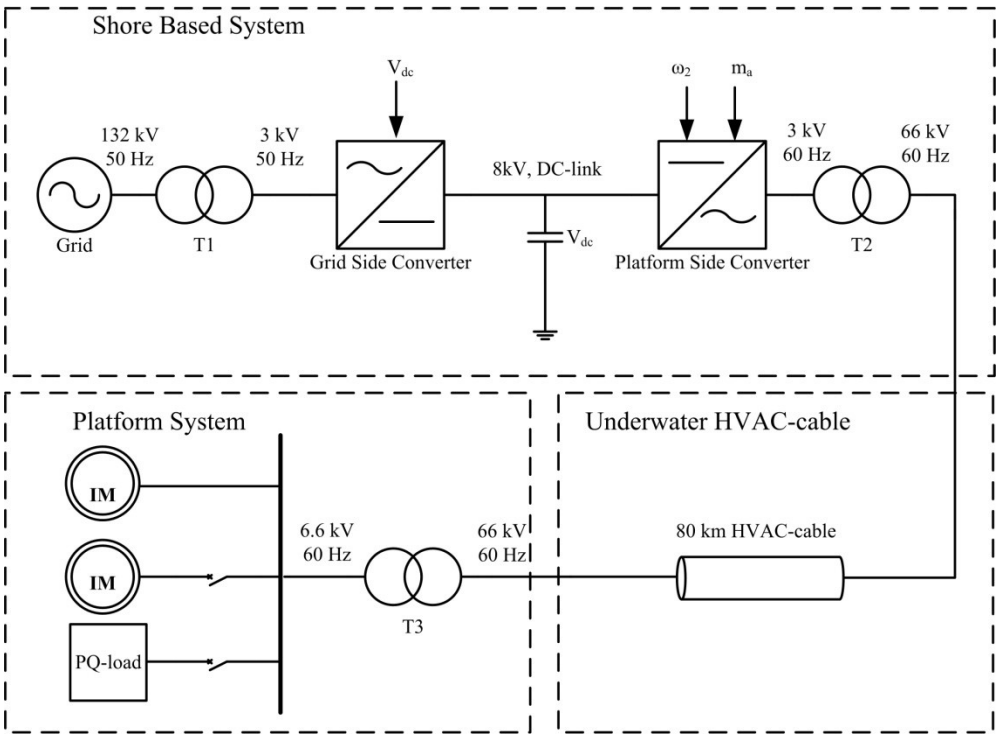

Figure 1-3 Configuration for electification of the oil platform system studied in this master thesis work

The proposed system is an offshore platform system supplied with power from shore through an 80 km underwater HVAC-cable. The configuration can be seen in Figure 1-3. The onshore stiff grid is feeding a shore-based back-to-back (B2B) VSC through a transformer. The platform-side VSC has a voltage level of 3 kV which is transformed to 66 kV and is supplying power to the HVAC-cable.

The lack of a synchronous generator on the platform for voltage and frequency regulation makes the system a passive grid, that is a system totally dependent on the voltage output of the platform-side VSC [19].

The proposed system only requires a step-down transformer, a cable connector and protection relays on the platform, which is advantageous for existing platform installations with very limited space. The solution provides the controllability of the VSC-HVDC, and makes maintenance of the B2B-VSC easier, since it is based on shore.

This thesis work should be considered a study to ensure proper passive system control so that the need of a gas turbine on the platform can be eliminated. This would reduce emissions of CO_2 and NO_x and reduce the need of maintenance of the gas turbine [20]. The controllers implemented in the study of this system can also be

used to ensure acceptable platform operation in “islanded mode,” that is if the synchronous generator is lost.

1.4 Scope of work

This thesis work is focused on modeling the system shown in Figure 1-3 as realistically as possible for the purpose of controlling the offshore platform voltage from shore. All modeling and simulations will be done in MATLAB® Simulink™.

The converters and the DC-link will be implemented as an average model. The HVAC-cable will be modeled by a single pi-equivalent cable model, which is proven to be an accurate for the frequency range to be considered. The platform load will be modeled by using induction machines and passive load components available in SimPowerSystems™, a Simulink™ toolbox.

The control strategies implemented for each of the VSC are based on existing control strategies that are modified and implemented in this system.

The grid-side converter will be used to control the DC-link voltage and to keep the reactive current absorbed from the grid equal to zero.

The platform-side converter will control the platform voltage and frequency. The main objective will be to keep the platform voltage and frequency at an acceptable level for possible platform load changes. Two platform voltage control strategies will be implemented in the system.

The first control strategy studied, denoted as control strategy 1, controls the platform voltage magnitude, while keeping the frequency fixed. A power management system (PMS) provides voltage measurements for the closed loop voltage controller on shore. In cases where the connection to the PMS system is lost, voltage measurements would no longer be available. Modeling of a steady-state platform voltage estimator will therefore be done to make sure platform voltage is kept within an acceptable range for autonomous operation. Control strategy 1 will be tested for measured platform voltage and estimated platform voltage.

The second platform voltage control strategy to be implemented and tested, denoted as control strategy 2, controls both the platform voltage magnitude and frequency.

Both control strategies will be tested separately, assuming a constant DC-link voltage. In addition to this, control strategy 1 will be tested when connected to the grid side-system, in the full B2B-VSC configuration.

The full B2B-VSC systems will be detailed topologies that can form the basis of a new way of connecting power from shore to offshore platform systems, controlling the platform voltage and frequency from shore, without requiring a lot of new equipment on the platform. A system as such would allow for removal of the low efficiency, high emission gas turbine driven synchronous generator that are the standard power source on oil platforms today.

The requirements for acceptable platform operation and control are defined in Table 1-1 and provide the control objectives for the platform voltage and frequency

control systems. The requirements are based on the IEC 61892 standard for mobile and fixed offshore units, electrical installations [21].

Cost of the solution and a study of where it might be applicable will not be evaluated in this thesis work.

Table 1-1 Platform system requirements for acceptable operation and control

Req. No.	Requirement Title	Description	Value
1	Steady-state voltage	Deviations from nominal steady-state voltage permitted for the system	$+6\%, -10\% * V_n$
	Transient voltage	Deviations from nominal steady-state voltage permitted during system transients, and permitted duration of transients	$\pm 20\% * V_n$ $t_{rec} < 1.5\ s$
2	Steady-state frequency	Deviations from nominal steady-state frequency that is permitted for the system	$\pm 5\% * f_n$
	Transient frequency	Deviations from nominal steady-state frequency during system transients, and allowable duration of transients	$\pm\ 10\% * f_n$ $t_{rec} < 5\ s$
3	Stable operation	Stable system operation during normal operation and normal system transients	Not Applicable

1.5 Report Outline

In this chapter a through description of the technologies available for electrification of offshore oil platforms has been given. The proposed system that has been described and the scope of work have been defined.

Chapter 2 provides the relevant theory for modeling the grid-side system, HVAC-cable, platform load and converters is given. An overview of conventional control methods available for VSC-control is also provided. At last the per-unit system used throughout the thesis is defined.

Chapter 3 describes the control strategies chosen for the grid- and platform-side converter systems, and provides the mathematical models for the controllers.

The methods used for tuning of the controllers and the results from the controller reference step change tests are given in chapter 4.

The mathematical model of the platform steady-state voltage estimator developed is given in chapter 5.

Chapter 6 provides the results from the system simulations. The ability of the platform voltage estimator to accurately estimate the platform voltage will be evaluated through load change tests, when no platform voltage controller is implemented. Control strategy 1 will be applied for control of the platform system, and simulations for both normal and autonomous operation will be run. The platform system will also be connected to the grid-side system, in the full B2B-VSC configuration. All the systems will be tested for three worst-case load changes on the platform. Control strategy 2 will then be applied to control the platform side system, and tested for the three load change tests.

The results are discussed in chapter 7, and the conclusion and further work proposed is given in chapter 8.

In the appendices additional system parameters, the MATLAB Simulink SimPowerSystem simulation models and simulation results will be provided.

In appendix D, the paper, "Kraftelektronikkens rolle ved elektrifisering av eksisterende offshore installasjoner, med kraft fra offshore vindpark og kraft fra land" is attached. The paper was written in cooperation between the author and the master student Atle Årdal, for the Norwegian Electro Technical Society conference in March 2011. The paper provides an overview over existing offshore electrification projects. It also describes two options for electrification of offshore oil and gas platforms: power from shore and power from offshore wind farms. Results from testing a platform system powered from shore through HVAC-cable for sudden loss of the synchronous generator, without controlling the shore VSC, are provided.

2 System Modeling

The modeling of the proposed system components, that form the basis of the implementation of the system in MATLAB® Simulink™, will be presented in this chapter.

The system to be modeled and implemented is shown in Figure 1-3 and repeated in Figure 2-1 for the reader's convenience. Simulations of this system requires accurate models for the grid-side converter, the DC-link and platform-side converters, which are responsible for supplying the platform system with power. The power is supplied through an HVAC-cable of 80 km; the model for this will also be presented here. Representation of loads for oil and gas platforms will be discussed, and the oil platform load model will be presented. The transformers used in the simulation model are from the SimPowerSystems™ toolbox and are not considered an important part of the thesis study, therefore will not be further discussed.

Relevant theory, equations and figures will be provided, and the model simplifications that are made will be presented.

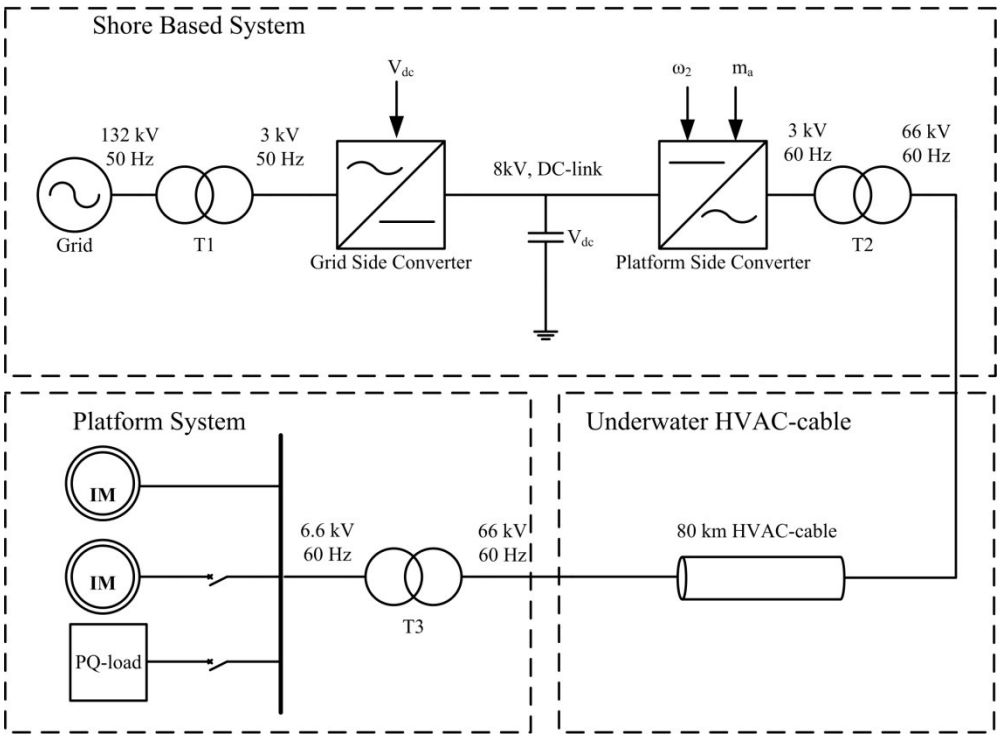

Figure 2-1 Configuration for electrification of offshore platform system studied

2.1 The Clarke and Park Transform

Three-phase induction machines have sinusoidal distributed three-phase windings which create a radially distributed magnetic field in the machine air gap. Each of the phase windings creates a magnetic field that peaks along its phase's axis. The three phase windings can be represented by three windings separated by 120 degrees each aligned with its phase's axis [22]. They can also be represented by two-phase windings or even rotating two-phase windings. This forms the basis of the Clarke- and Park-transform [13]. These transforms are frequently applied to modeling and control of synchronous machines and induction machines, but also for other three-phase quantity control systems, because it makes decoupled control of active and reactive currents possible, which will be shown in a later chapter in this thesis.

All three-phase systems considered in this chapter are assumed to be balanced, and hence the zero sequence components are not included in the equations provided.

Three phase quantities can be expressed as follows

$$\begin{aligned} V_a(t) &= V_m \sin(\omega t + \phi) \\ V_b(t) &= V_m \sin(\omega t + \phi - 120^o) \\ V_c(t) &= V_m \sin(\omega t + \phi + 120^o) \end{aligned} \tag{2-1}$$

where V_m is the line-to-line, RMS voltage magnitude and ϕ is the initial phase shift. The three phase quantities can be represented by a space vector. Space vectors will throughout this thesis work be represented with an arrow. The space vector is defined as follows [22]

$$\vec{V}(t) = \sqrt{\frac{2}{3}}\left(V_a(t) + V_b(t)e^{-j120} + V_c(t)e^{j120}\right) \tag{2-2}$$

The voltage space vector can be defined relative to other reference frames than the three-phase frame. The Clarke-transform represents three-phase quantities relative to a two-phase reference frame αβ. The α-axis is aligned with the a-axis of the three-phase system, and the β-axis is leading the α-axis by 90 degrees [22], see Figure 2-2.

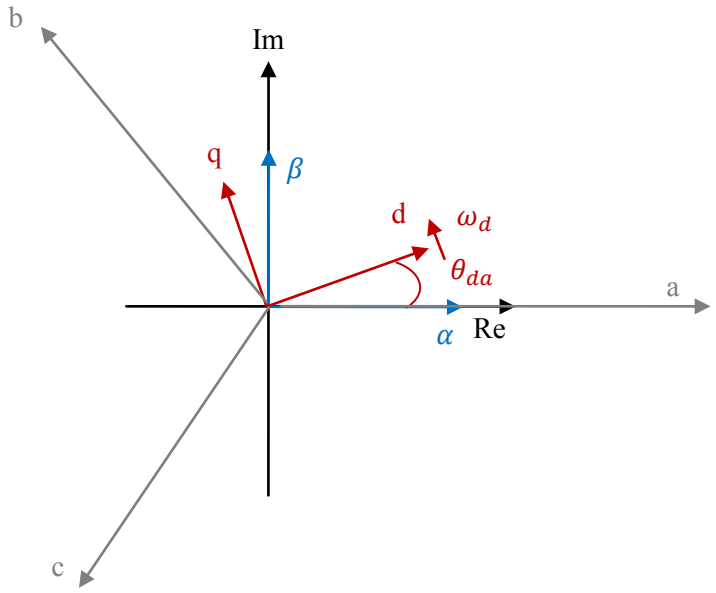

Figure 2-2 Relation between three-phase-, αβ- and dq-reference frame

The Clarke-transform from the three-phase reference frame to the fixed αβ reference frame is given as follows [22]

$$\begin{bmatrix} x_\alpha \\ x_\beta \end{bmatrix} = k * \begin{bmatrix} 1 & -\frac{1}{2} & -\frac{1}{2} \\ 0 & \frac{\sqrt{3}}{2} & -\frac{\sqrt{3}}{2} \end{bmatrix} * \begin{bmatrix} x_a \\ x_b \\ x_c \end{bmatrix} \tag{2-3}$$

where *x* represents current, voltage, flux linkage and other three-phase quantities, *k* is a constant that will be defined later in this section.

The Park-transform, also called the dq-transform, represents three-phase quantities relative to a synchronously rotating two-phase reference frame dq, see Figure 2-2. There are several different practices for orientation of the two-phase axes of the Park transform. Equations for aligning the d-axis with the three phase system a-axis at time t = 0, while the q-axis is leading by 90 degrees is the practice of [22]. This practice for axis orientation will be used in this thesis work, unless otherwise stated. In [23] an axis orientation where the q-axis is aligned with the three-phase system a-axis, while the d-axis is leading by 90 degrees is used. This transform results in the same equations as of those presented here, but the ordering of d and q will be opposite. Another variation of the axis orientation is with the d-axis is aligned with the system a-axis, but the q-axis is lagging by 90 degrees [24]. The equations for the dq-transform of a system with these axis orientations will have opposite signs for all sin-terms than the equations presented here.

The relation between the $\alpha\beta$- frame and the dq-frame, can be seen in Figure 2-2, and is given as follows [22]

$$X_{dq} = X_{\alpha\beta} e^{j\theta_{da}} \tag{2-4}$$

θ_{da} is the angle between the rotating d-axis and the fixed α-axis, that is changing with time, and can be expressed by $\omega_d * t$, where ω_d is the rotational speed of the dq-axes.

Equation (2-4) and Euler's formula gives the following relation on matrix form between the αβ-components and the dq-components

$$\begin{bmatrix} x_d \\ x_q \end{bmatrix} = \begin{bmatrix} cos\,\theta_{da} & sin\,\theta_{da} \\ -sin\theta_{da} & cos\,\theta_{da} \end{bmatrix} * \begin{bmatrix} x_\alpha \\ x_\beta \end{bmatrix} \tag{2-5}$$

Three-phase quantities can also directly be transformed to the dq-reference frame; this is illustrated by Figure 2-3, where the dq-components of the rotating voltage space vector $\vec{V}$ are shown.

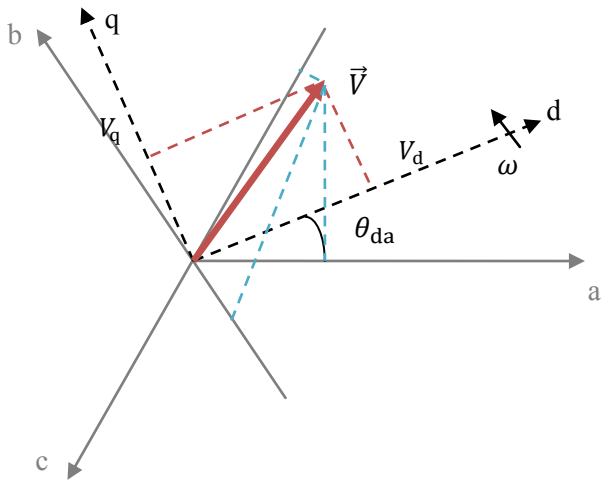

Figure 2-3 Space vector $\vec{V}$ represented by both abc- and dq- axis components

The direct abc- to dq-transform is given by the following equation

$$\begin{bmatrix} x_d \\ x_q \end{bmatrix} = k * \begin{bmatrix} cos\theta_{da} & cos\left(\theta_{da} - \frac{2\pi}{3}\right) & cos\left(\theta_{da} + \frac{2\pi}{3}\right) \\ -sin\theta_{da} & -sin\left(\theta_{da} - \frac{2\pi}{3}\right) & -sin\left(\theta_{da} + \frac{2\pi}{3}\right) \end{bmatrix} * \begin{bmatrix} x_a \\ x_b \\ x_c \end{bmatrix} \tag{2-6}$$

The inverse transform is found as follows

$$\begin{bmatrix} x_a \\ x_b \\ x_c \end{bmatrix} = k * \begin{bmatrix} cos\ \theta_{da} & -sin\theta_{da} \\ cos\left(\theta_{da} - \frac{2\pi}{3}\right) & -sin\left(\theta_{da} - \frac{2\pi}{3}\right) \\ cos\left(\theta_{da} + \frac{2\pi}{3}\right) & -sin\left(\theta_{da} + \frac{2\pi}{3}\right) \end{bmatrix} * \begin{bmatrix} x_d \\ x_q \end{bmatrix} \quad (2\text{-}7)$$

The Park transform can be voltage invariant, meaning that the voltage magnitudes are the same for the three phase quantities and the dq-quantities. For the voltage invariant transform, k is set to $^2/_3$ [13]. The transform can also be done power invariant, meaning that the power is the same for the three-phase quantities and the dq-quantities. For the power invariant transform, k is set to $\sqrt{^2/_3}$ [13]. Unless otherwise stated, the voltage invariant transform will be used in this thesis work.

2.2 Grid-Side Model

The grid-side system consists of the stiff grid connected to the grid side converter through a transformer. The stiff grid has a constant voltage and a constant frequency of 50 Hz, and is modeled as a stiff three-phase voltage source. To simplify modeling and calculations the transformer is represented by a small resistance and an inductance in series [25], and the grid voltage V_g is assumed to have the same base as the converter voltage V_c. The grid-side system model can be seen in Figure 2-4, and the parameters used for calculations and simulations can be found in Table 2-1.

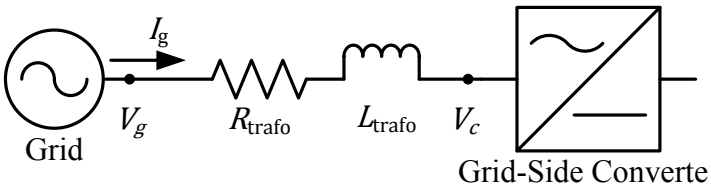

Figure 2-4 Grid-side model

Table 2-1 Grid-side parameters

Description	Value	Unit
$\boldsymbol{V_{c,base}, V_{g,base}}$	3	kV
$\boldsymbol{R_{trafo}}$	0.01	pu
$\boldsymbol{L_{trafo}}$	0.15	pu

2.3 Voltage Source Converter Models

Due to its advantageous properties, as described in section 1.2, the three-phase voltage source converter (VSC) is the essential component of most new flexible AC-transmission system (FACTS) devices. Recently, this has been frequently used in HVDC-transmission configurations.

This section will provide a description of the VSC model used for the system simulations and the equations for dimensioning the DC-link quantities. The advantages of the two degrees of freedom for control of the output signal of the VSC will be shown. The two levels of VSC control will be discussed and a brief summary of second level control strategies available for the VSC will be provided.

2.3.1 VSC Model Used for Simulations

The converter can be represented at different levels of detail: full switching models, switching models with ideal switches or average models.

An average converter and DC-link model is chosen for this particular system study. The average model assumes that the switching frequency is infinite, which means that the output voltage of the converter is a pure sinusoidal wave, and hence all harmonics are neglected. It also neglects switching and conduction losses.

This average converter model reduces the computational time for simulations considerably, and since neither harmonics nor switching losses are going to be studied, the average model provides acceptable accuracy for this thesis study.

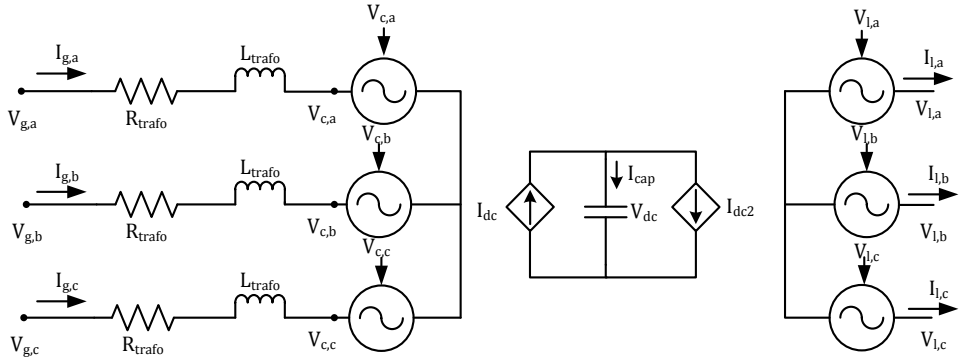

Figure 2-5 Back-to-back voltage source converter average model

The average converter and dc-link model used can be seen in Figure 2-5, where the converters are in B2B-configuration. The voltage source converter models consist of controllable voltage sources and a DC-link with controllable current sources. The voltage sources and current sources are controlled based on the power conservation equation, that is power needs to be conserved between the AC-and DC-sides of the converter at all times. For the converter system on the left side in Figure 2-5, this can be expressed as follows [19]

$$P_c = P_{\mathrm{dc}} \tag{2-8}$$

This can be rewritten with dq-component voltages and currents as

$$\frac{3}{2}\left(V_{gd} i_{gd} + V_{gq} i_{gq}\right) = V_{\mathrm{dc}} I_{\mathrm{dc}} \tag{2-9}$$

neglecting the losses through the transformer inductance and resistance. The current relation for the DC-link circuit is given as follows

$$I_{\mathrm{dc}} = I_{\mathrm{cap}} + I_{\mathrm{dc2}} \tag{2-10}$$

Where I_{dc} is the current consumed from or supplied to the DC-system, from the grid-side system, I_{cap} is the current through the DC-link capacitor, and I_{dc2} is the current consumed by or supplied to the platform-side system.

The power conservation equations for the converter system on the right side of Figure 2-5 is given as follows

$$P_{\mathrm{dc}} = P_l \tag{2-11}$$

This can also be rewritten as

$$V_{\mathrm{dc}} I_{\mathrm{dc2}} = V_{la} i_{la} + V_{lb} i_{lb} + V_{lc} i_{lc} \tag{2-12}$$

which can be written with dq-components as follows

$$V_{\mathrm{dc}} I_{\mathrm{dc}} = \frac{3}{2}\left(V_{ld} i_{ld} + V_{lq} i_{lq}\right) \tag{2-13}$$

These equations give the complete average model of the B2B-VSC system used for simulations in Simulink™ SimPowerSystems™.

2.3.2 DC-link parameters

The parameters for the DC-link rated voltage and capacitor need to be chosen carefully to get the desired converter operation. The rated voltage has to be chosen so that it is able to control the output voltage to be sinusoidal [26].

The dc-voltage level is calculated based on the rated voltage on the AC-side of the converter, and its maximum modulation index, as follows [16]

$$V_{\mathrm{dc}} = \frac{2\sqrt{\frac{2}{3}}V_{\mathrm{base,RMS}}}{m_a} \tag{2-14}$$

where $V_{\mathrm{base,RMS}}$ is the AC-side base RMS-voltage, while m_a is the converter modulation index. To avoid over modulation, the modulation index should not be larger than one [16]. The modulation index is defined as the magnitude of the signal that is compared to the carrier signal, when carrier based modulation of switching is done [16]. Due to the average converter model implemented in this thesis work, PWM will not be done. The modulation index is therefore set to be the magnitude of the VSC output voltage, and denoted as $|V_l|$, from now on.

The size of the capacitor chosen for the DC-link affects the steady-state voltage ripple, transient over voltages and the ability to rapidly control the power flow through the DC-link [26], and should therefore be carefully chosen. The DC-link capacitor for this system will be chosen based on the capacitor time constant, defined as the time it takes to charge the capacitor from zero to rated voltage. The equation for the capacitor time constant is given as follows [27]

$$\tau = \frac{\left(\frac{1}{2}CV_{\mathrm{dc}}^2\right)}{S_n} \tag{2-15}$$

where V_{dc} is the rated dc-link voltage, C denotes the capacitor and S_n is the rated power of the converter. A time constant τ of less than or equal to 5 ms is considered to give acceptable voltage ripple, small transient over voltage and fast control of active and reactive power, and is suggested by [27].

The DC-link values for the system studied in this thesis are calculated based on equations (2-14) and (2-15), and are summarized in Table 2-2.

Table 2-2 DC-link parameters used for modeling and simulations

Description	**Value**	**Unit**
Rated DC-voltage, V_{dc}	8	kV
DC-link capacitor, C	16	mF

2.3.3 Control Strategies for VSCs

The voltage source converter uses pulse width modulation (PWM) for generating the VSC output signal. This means that both the converter output voltage magnitude and the phase angle can be independently controlled [28] and that the VSC has two degrees of freedom for control.

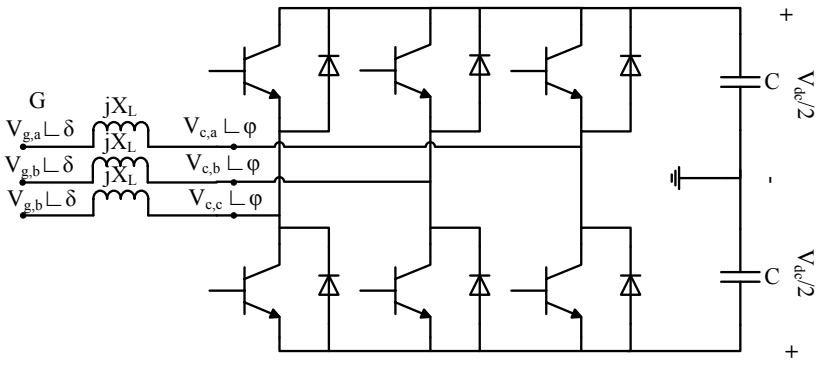

Figure 2-6 VSC configuration with IGBT switches

The VSC configuration can be seen in Figure 2-6, and the active power supplied or consumed at the terminal G, can be calculated as follows [25]

$$P = \frac{V_g V_c}{X_L} \sin(\phi - \delta) \tag{2-16}$$

The reactive power consumed or supplied at terminal G can be calculated as follows [25]

$$Q = \frac{V_g V_c \cos(\delta - \phi)}{X_L} - \frac{V_g^2}{X_L} \tag{2-17}$$

From these equations it can be seen that since the PWM can control both the converter output voltage magnitude V_c and the angle ϕ independently, the active and reactive power flows can be controlled almost independently [28].

The VSC uses pulse width modulation (PWM) to generate the desired output signal of the converter. To be able to provide the desired output signal, modulation of the converter switching needs to be done. There are several methods for modulation of the converter switching, some examples are: sinusoidal-PWM and space vector PWM [29] [30]. There is also a need for external VSC controllers to generate the output voltage reference for the switch modulation. There are several conventional control strategies available for external control of VSC.

In this thesis work an average VSC model is used, as described in section 2.3.1, and there is no need for switch modulation for the converter. Therefore only methods for external control of the VSC will be described in this thesis work.

The external control strategy chosen depends on which type of AC-network the VSC is connected to, and the control objectives for that particular system.

There are mainly three types of AC-networks: stiff grids, weak grids and passive grids. In a stiff grid the voltage and frequency are constant at the point of common connection (PCC), for all changes of active and reactive power flow [19]. In a weak

grid, the voltage and frequency at the PCC reacts to changes in active and reactive power flow. Weak grids are usually associated with long transmission lines, that have considerable resistive voltage drops [19]. A passive grid is a network where the voltage in the PCC is exclusively dependent on the voltage applied by a converter or a voltage source [19]. In such a system, the load is passive, and hence does not consist of any type of source.

Five different control strategies for VSC, when connected to one of the AC-networks presented above, were listed in [19] as follows:

- Type 1: Vac and frequency control (VSC connected to passive grid)
- Type 2: Constant P-Vac control (VSC connected to weak grid)
- Type 3: Vac-Udc control (VSC connected to weak grid)
- Type 4: P-Q-control (VSC connected to stiff grid)
- Type 5: Q-Udc control (VSC connected to stiff grid)

Control strategy of type 2-5 uses cascade control, with an inner current control loop, and an outer control loop depending on the specific type of control strategy. The park transform, presented in section 2.1 is used for this control strategy. The control strategies used in this thesis work will be elaborated in chapter 3 .

2.4 HVAC Cable

The HVAC cable parameters are determined in this section, before the critical length of the cable is calculated and the reactive power production is discussed. The HVAC-cable model used for simulations is also presented.

2.4.1 Cable Parameters

Three-core, cross-linked polyethylene (XLPE) HVAC cables have been used for several offshore electrification projects [10], and are assumed to be the type of HVAC-cable used for electrification of the offshore platform in this thesis study. The XLPE cables can be continuously loaded to a conductor temperature of $90^{o}C$, and the main cable losses are ohmic and occur in the conductor and metallic screen [31].

The cable parameters used are based on [31], and given in Table 2-3.

Table 2-3 Cable parameters

Description	**Value**	**Unit**
Rated power	40	MVA
Rated voltage	66	kV-LL
Cable length	80	km
$\boldsymbol{R_{\text{cable}}}$ **resistance per unit length**	0.10	Ω/km
$\boldsymbol{L_{\text{cable}}}$ **inductance per unit length**	0.4	mH/km
$\boldsymbol{C_{\text{cable}}}$ **capacitance per unit length**	0.2	μF/km

2.4.2 Critical Cable Length and Power Transmission Capability

Underground or underwater high voltage AC power cables store and release electrical energy with voltage variations, like a shunt capacitor. This generates capacitive current, which increases linearly with the length of the cable. The charging current can, for long HVAC-cables, get so large that the the thermal current rating limit is reached for the cable. This will limit the capacity of the cable to supply active power to the load [32]. The critical length of an HVAC-cable can be defined as the cable length where the capacitive current produced by the cable is at the maximum thermal capacity of the cable. This is the length at which no active power can be transferred without overloading the cable. The critical cable length can be calculated as follows [32]

$$L_{\text{critical}} = \frac{I_{\text{rated}}}{\omega C} \frac{\sqrt{3}}{V_{\text{rated}}} \tag{2-18}$$

where ω is the angular frequency of the system, C is the capacitance of the line per km, I_{rated} is the rated current of the system and V_{rated} is the rated voltage of the system.

The critical length of the HVAC-cable calculated based on the parameters listed in Table 2-3, and the apparent power rating of 40 MVA and voltage rating of 66 kV-LL, gives a critical cable length of 121 km, which is 41 km longer than the planned length of the cable. If needed, the critical length of the cable can be increased by over dimensioning the current capacity of the cable.

The maximum active power transmission capability of a cable, for a certain apparent power input, is based on the general equation for apparent power, and is given as follows [32]

$$P_L = \sqrt{S_G^2 - (\omega C L V^2)^2} \tag{2-19}$$

where S_G is the apparent power fed into the cable, ω is the angular frequency of the system, C is the capacitance per km of the cable, L is the length of the cable and V is the voltage level of the cable. The term representing the reactive power of the cable in equation (2-19) is constant for a constant voltage level, and a given line length. For the parameters defined in Table 2-3, with the rated voltage of 66 kV, the reactive power term is equal to ~26 MVAr, which means that if the cable system should be able to supply 40 MW at full platform load, the system needs to be dimensioned for approximately 47 MVA. Another solution for reducing this reactive power tern would be to introduce a reactive power compensation device such as a phase reactor.

The platform load will be defined in section 2.5, and it can be seen there that the equipment will not only consume active power, but also some of the reactive power produced by the cable. Over dimensioning of the system for 47 MVA is therefore not considered necessary in this case. This is however a matter that should be taken into careful consideration when determining the cable and equipment rating for supplying offshore systems with power from shore through HVAC-cables.

2.4.3 Modeling of the HVAC-cable

There are two main approaches to modeling of transmission lines and cables; distributed parameters and lumped parameters [33]. The distributed parameter models tend to be more accurate than the lumped parameter models. Lumped parameter modeling is done by modeling the cable as pi-equivalents, which is an approximate of the distributed parameter model.

A lumped parameter pi-equivalent cable model will be used in this thesis work, because it provides an acceptably accurate model of the behavior of the distributed parameters at each end of the cable. The circuit diagram for a single pi-equivalent circuit can be seen in Figure 2-7. Depending on the application and what is studied, the pi-equivalent circuit will be modeled with either SimPowerSystems™ impedance, resistance and capacitance, or with the SimPowerSystems™ single phase pi section line defined in [34]. The parameters specified in Table 2-3 are the input of the SimPowerSystems™ cable model, in addition to specifying the number of pi-equivalent circuits.

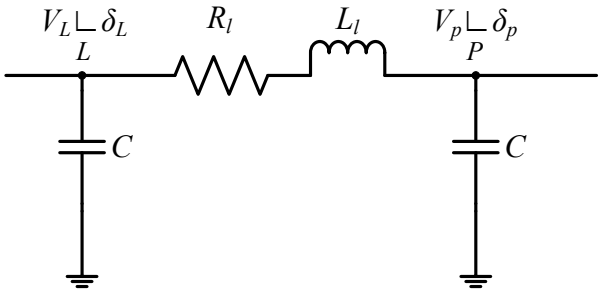

Figure 2-7 Single pi-equivalent circuit

Though the HVAC-cable is meant to carry power with a frequency of 60 Hz, due to switching transients and harmonics it will in reality be carrying frequencies in the kHz range as well. In this thesis work switching of the transistors is neglected, as described in section 2.3.1, fault analysis with protection relay switching is not considered and hence switching transients will not have an impact on the system nor the cable in the simulations. This means that the cable model used for the simulations need not be accurate at high frequencies.

The number of cascaded pi-equivalent circuits needed can be calculated based on the following equation for the frequency range of which the cable model needs to be accurate [34]

$$f_{max} = \frac{Nc}{8l_{\text{tot}}} \tag{2-20}$$

where N is the number of pi-equivalent circuits, c is the propagation speed in km/s and l_{tot} is the total length of the line in km.

The propagation speed on the line can be can simplified be calculated as follows [25]

$$c = \frac{1}{\sqrt{LC}} \tag{2-21}$$

where L is the cable inductance and C is the cable capacitance, both expressed in Henry and Farad per unit length of the cable respectively.

For the cable parameters given in Table 2-3, the propagation speed is 111,803 km/s. The maximum frequency, of which a cable model with one pi-equivalent will be accurate, is calculated with equation (2-20). A one pi-equivalent model will be acceptable for frequencies up to 174 Hz. This is considered sufficient due to the previously explained simplifications made for the converter switching and no fault studies. Hence a cable model of one pi-equivalent circuit can and will be used for simulation in this thesis work.

2.5 Oil Platform

The main part of the power supplied to an offshore oil and gas platforms is consumed by electric motors driving pumps, compressors or other equipment on the platform [4]. Other electrical load that is consuming electric power are heaters for the production process, lighting, comfort heating and auxiliary equipment [4]. Based on this, the platform load is modeled by a large squirrel cage induction motor representing an accumulated model of induction motors on the platform; a smaller squirrel cage induction motor for testing of direct on line (DOL) starting on the platform; and passive PQ-load that represents process heating, lighting, comfort heating and auxiliary equipment. Though synchronous motors are also used for driving loads on platforms, this will not be included in the oil platform load model.

The total load of an oil platform depends on a range of things, such as the size of the field, whether water or gas injection is done, the amount of processing of the oil and gas done on the platform and which type of transportation system the platform uses for the oil and gas. The total load can vary from <100kW from small wellhead platforms to >100 MVA for large oil and gas platforms [4].

The equipment for supplying power to the platform system studied in this thesis are all rated for 40 MVA, but the total load of the platform is set to 35 MVA. This is done because it is assumed that the equipment is rated for an increase of platform load in the future.

Table 2-4 Platform load used for simulations

Description	Value	Unit
Accumulated induction motor model	23	MVA
Induction motor for DOL-starting	8	MVA
Passive constant PQ-load	4	MVA
Total platform load	***35***	***MVA***

2.5.1 Induction Motors

Induction motors are, as mentioned in section 2.5, the component on offshore platforms consuming the main part of the power. The way they are connected on the platform depends on the size of the machine and the short circuit current capability of the network. Induction machines of ratings up to 8 MVA are generally directly connected on the platform [4]. Induction motors with larger ratings than this are connected through variable speed drives (VSD), making soft-starting possible [4].

Both the directly connected and the VSD-connected induction motors are represented by the accumulated induction machine in this platform model. This is a simplification because most VSD on existing platforms are thyristor converters that will introduce considerable amounts of harmonics on the platform.

2.5.1.1 Mathematical Representation of the Induction Motor

A squirrel cage induction machine can be represented by a set of electrical equations for stator and rotor voltage and electrical torque, and a set of mechanical equations to represent the mechanical behavior of the machine. To simplify modeling and control the park transform, presented in section 2.1, is used to transform the three-phase machine equations into the qd-plane.

The induction machine model used for simulations is from the SimPowerSystems™ toolbox [35], where the mathematical model of the induction machine is based on [23], and will be presented here. The induction machine stator voltages are given in matrix form as follows

$$\begin{bmatrix} V_{sq} \\ V_{sd} \end{bmatrix} = R_s \begin{bmatrix} i_{sq} \\ i_{sd} \end{bmatrix} + \frac{d}{dt} \begin{bmatrix} \lambda_{sq} \\ \lambda_{sd} \end{bmatrix} + \omega_q * \begin{bmatrix} 0 & 1 \\ -1 & 0 \end{bmatrix} * \begin{bmatrix} \lambda_{sq} \\ \lambda_{sd} \end{bmatrix} \qquad (2\text{-}22)$$

where V_{sq} and V_{sd} are the stator voltages, i_{sq} and i_{sq} are stator currents and λ_{sq} and λ_{sd} are the stator flux linkages. ω_q is the angular velocity of qd-reference frame in electrical rad/s, and is generally chosen to be equal to the synchronous speed [22].

The rotor voltage equations are given as follows

$$\begin{bmatrix} V_{rq} \\ V_{rd} \end{bmatrix} = R_r \begin{bmatrix} i_{rq} \\ i_{rd} \end{bmatrix} + \frac{d}{dt} \begin{bmatrix} \lambda_{rq} \\ \lambda_{rd} \end{bmatrix} + (\omega_q - \omega_r) * \begin{bmatrix} 0 & 1 \\ -1 & 0 \end{bmatrix} * \begin{bmatrix} \lambda_{rq} \\ \lambda_{rd} \end{bmatrix} \quad (2\text{-}23)$$

where V_{rq} and V_{rd} are the rotor voltages, i_{rq} and i_{rq} are rotor currents and λ_{rq} and λ_{rd} are the rotor flux linkages. For a squirrel cage machine, the rotor voltages are zero, due to the shorted squirrel cage bars. ω_r is the rotor angular velocity in electrical rad/s, which makes the term $(\omega_q - \omega_r)$ equal the slip speed in electrical rad/s.

These equations can be represented by the equivalent circuits in Figure 2-8.

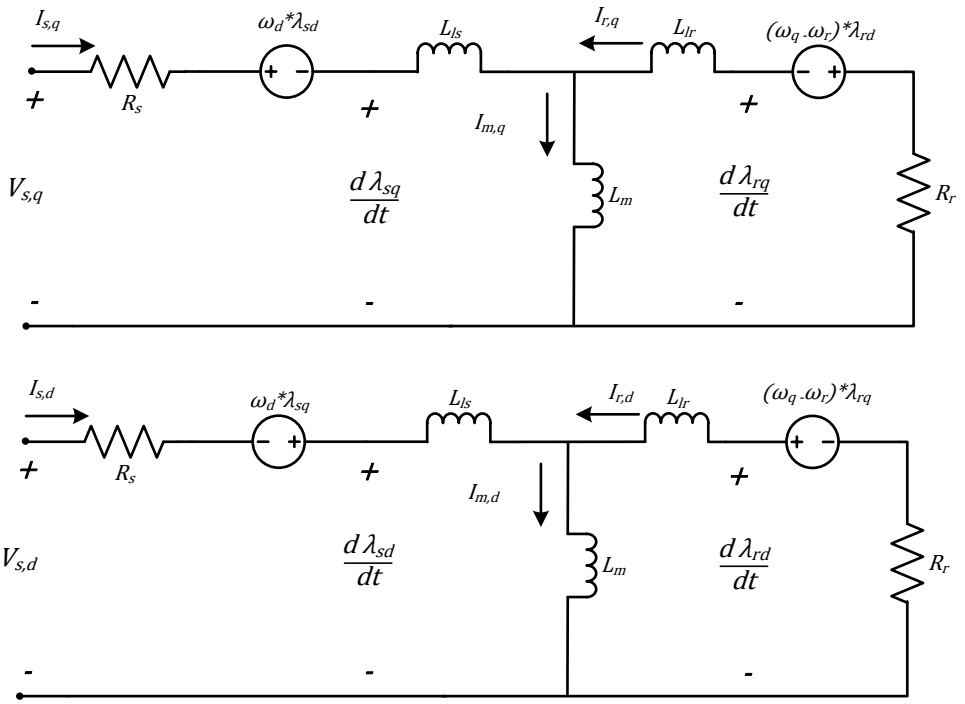

Figure 2-8 Induction motor qd-winding equivalent circuit [22] [35]

The electrical torque on the stator is given by the following equation [23]

$$T_e = \frac{3}{2} p(\lambda_{sq} i_{sd} + \lambda_{sd} i_{sq}) \quad (2\text{-}24)$$

The swing equation completes the mathematical model, and is given as follows

$$\frac{d}{dt}\omega_m = \frac{1}{2H}\left(T_m - F\omega_m - T_e\right) \tag{2-25}$$

Where ω_m is the mechanical angular speed, H is the combined rotor and load inertia constant, F is the combined rotor and load viscous friction coefficient and T_m is the mechanical shaft torque [23]. The mechanical speed is the derivative of the mechanical angular position θ_m.

This mathematical model is the full dynamic induction machine model. For steady-state operation, the time derivative terms can be cancelled, and the induction machine equivalent circuit seen in Figure 2-8 can be simplified by removing the voltage sources.

The parameters used for the two induction machines can be found in appendix A.

2.5.1.2 Induction Motor Load Profile

The mechanical load profile has great impact on the motor operation. The load profile used for modeling is dependent on what the motor is expected to drive in a real system. Some applications of the induction machines on platforms are driving gas recovery compressors, cooling medium circulation pumps, sea water lift pumps and crude oil export pumps.

In [36] the mechanical load profiles are divided in 4 torque profile groups

1) $T_{m1}(\omega) = a + b\omega^{-1}$
2) $T_{m2} = k$
3) $T_{m3}(\omega) = a + b\omega$
4) $T_{m4}(\omega) = a + b\omega^2$

The first group is for loads that need a constant power applied. The second group is for loads that need constant torque, for example machinery in conveyor belts. The third group is for machinery used for material processing; in rollers. The forth mechanical load profile is for machinery using centrifugal force, for example centrifugal pumps.

The fourth load profile is the most similar to the load an induction machine would be driving on an oil platform, and hence is the load profile used for modeling of the induction machine load. This will be implemented by measuring the angular speed of the machine, and feeding the squared angular speed with the system dependent parameters a and b into the mechanical load input of the machine model.

2.5.2 PQ-load

The passive PQ-load used in simulation to represents process heating, lighting, comfort heating and auxiliary equipment is modeled as a constant impedance load at constant frequencies. The only available load model in the SimPowerSystems 2010b toolbox is a constant impedance load; this will be utilized for the entire

passive PQ-load model. A more representative model for the platform load could be to model the process and comfort heating as impedance, while modeling the auxiliary equipment and lighting as a constant PQ-load.

The impedance of the load is defined as follows

$$Z_{\text{load}} = R_{\text{load}} + j\omega L_{\text{load}} \tag{2-26}$$

It can be seen that the platform PQ-load is assumed to be strictly resistive and inductive, and does not have a capacitive component. The active power consumed by the load can be calculated as follows

$$P_{\text{load}} = \frac{V_p^2}{R_{\text{load}}} \tag{2-27}$$

The reactive power consumed by the load is found as follows

$$Q_{\text{load}} = \frac{V_p^2}{\omega L_{\text{load}}} \tag{2-28}$$

2.6 Per Unit system

Per unit (pu) values for modeling and simulation of systems simplifies comparison between parts of the system with different ratings, eliminating the need to work with large values in calculations and simplifying the VSC control. The equations used to calculate the base values used to determine the system per unit values will be provided in this section. All simulation system and controller models will be implemented based on these per unit value definitions.

2.6.1 AC-System Base Values

The base values of a system, are usually defined as the rated values for apparent power, voltage, current and impedance. The apparent power rating should be set to one value for the entire system for simplification of per unit calculations. The voltage levels, and hence the rated voltages varies throughout a system. Base values need to be calculated for each part of the system with a separate voltage rating.

The system base values of a specific voltage level are calculated as follows, where all voltages and currents are RMS-values unless otherwise stated

$$I_{\text{base}} = \frac{S_{\text{base},3\phi}}{\sqrt{3}V_{\text{base,LL}}} = \frac{S_{\text{base},1\phi}}{V_{\text{base,LN}}} \tag{2-29}$$

The base value for the impedance is used as the base value for the resistance and reactance, and is found as follows [25]

$$Z_{\text{base}} = \frac{V_{\text{base,LL}}}{\sqrt{3}I_{\text{base}}} = \frac{V_{\text{base,LN}}}{I_{\text{base}}} \tag{2-30}$$

Base values for inductances and capacitances are calculated in various ways throughout the literature, the base value calculation used in this thesis, unless otherwise stated, is defined as follows

$$L_{\text{base}} = \frac{Z_{\text{base}}}{\omega_b} \tag{2-31}$$

The base value for the capacitance

$$C_{\text{base}} = \frac{1}{\omega_b Z_{\text{base}}} \tag{2-32}$$

In this thesis work dq-reference frame control will be done, which creates a need for base values for the system dq-quantities as well as for the three phase quantities. The dq-transform is, as previously stated, chosen to be voltage invariant, which makes it convenient to define their base values as follows [37]

$$V_{\text{base,d}} = V_{\text{base,q}} = \hat{V}_{\text{base,LN}} = \frac{\sqrt{2}}{\sqrt{3}}V_{\text{base,LL}} \tag{2-33}$$

It can be seen that the dq-voltage bases are set to the line-to-neutral peak voltage. The corresponding base values for the dq-currents are given as follows [37]

$$I_{\text{base,d}} = I_{\text{base,q}} = \hat{I}_{\text{base}} = \sqrt{2}I_{\text{base}} \tag{2-34}$$

It can be seen from the equation above that the dq-current base is set to the peak base current.

2.6.2 DC-Link Base Values

The base values for the DC-link circuit are defined based on the AC-system base values. The rated DC-link power is set equal to the AC-side rated power, as follows

$$S_{\text{base},3\phi} = S_{\text{DCbase}} \tag{2-35}$$

The base value for the DC-link voltage is chosen based on the per unit system used in [37], where the DC-link voltage is set to 2 times the AC-side line-to-neutral peak voltage as follows

$$V_{\text{DC,base}} = 2\sqrt{\frac{2}{3}}\, V_{\text{base,LL}} \tag{2-36}$$

By inputting equation (2-35) in the expression for the base DC-power in equation (2-34) and solving for the DC-current the following expression for current is obtained

$$I_{\text{DCbase}} = \frac{3}{4}\sqrt{2} I_{\text{base}} \tag{2-37}$$

The base value for the DC-link impedance is found as follows

$$Z_{\text{DCbase}} = \frac{V_{\text{DCbase}}}{I_{\text{DCbase}}} \tag{2-38}$$

3 Control Strategy

The system to be controlled was presented in section 1.3, and modeled in chapter 2 . The mathematical modeling and implementation of the control systems for the B2B-VSCs placed on shore is presented in this chapter.

The main purpose of the B2B-VSC controller is to regulate the offshore platform voltage and frequency. For proper operation, the controller also needs to keep the DC-link voltage constant, and to limit the reactive power drawn from the onshore grid. The control strategies implemented for each of the VSC are based on existing control strategies, modified for this system configuration.

The control objectives of the system are defined as follows:

- To keep the voltage of the DC-link constant for changes and disturbances on the grid side, and for changes of active and reactive power consumed on the platform side
- To maintain unity power factor at the grid terminals
- To keep the voltage on the platform within an acceptable range defined in Table 1-1 for all realistic changes in platform load, and for load dynamics
    - When platform voltage measurements are available
    - For autonomous operation
- To keep the platform side frequency within the acceptable range defined in Table 1-1
- To maintain stability for normal system operation in steady-state and during normal system transients

The grid side converter is connected to the stiff grid at the PCC, and the grid side VSC is chosen to control the DC-link voltage and the reactive power Q absorbed from the grid. This is the type 5 controller, defined in section 2.3.3.

The platform side converter is connected to a passive grid at the PCC, and hence the voltage set by the converter output is the only voltage that will influence the platform system voltage. The platform voltage and frequency will be controlled by controlling the platform side VSC output voltage and frequency, and hence the platform side VSC-controller will be the Type 1 controller, defined in section 2.3.3.

Two approaches for platform voltage control will be presented in this chapter, and later implemented, tuned and tested

In section 2.3.1, the average model used for the VSC is described. No switching modulation scheme will be implemented, and the output quantities of the controllers are directly controlling the VSC output voltage, either through controlling the converter output RMS voltage magnitude $|V_l|$, or though controlling the signal directly.

All controllers are implemented based on the per-unit system defined in section 2.6. The controller models are implemented and simulated in MATLAB® Simulink™.

3.1 Grid-Side Converter Control

The control objectives for the grid side VSC control system is to keep the DC-link voltage constant, and to make sure no reactive power Q is consumed from the grid. The control strategy implemented is based on the active system control strategy in [38] and is a cascade controller where the outer control loops are reactive power and DC-link voltage controllers that provide inner current control loops with their references. The inner current control loops sets the converter output voltage.

An overview of the grid side converter control system to be modeled and implemented is shown in Figure 3-1.

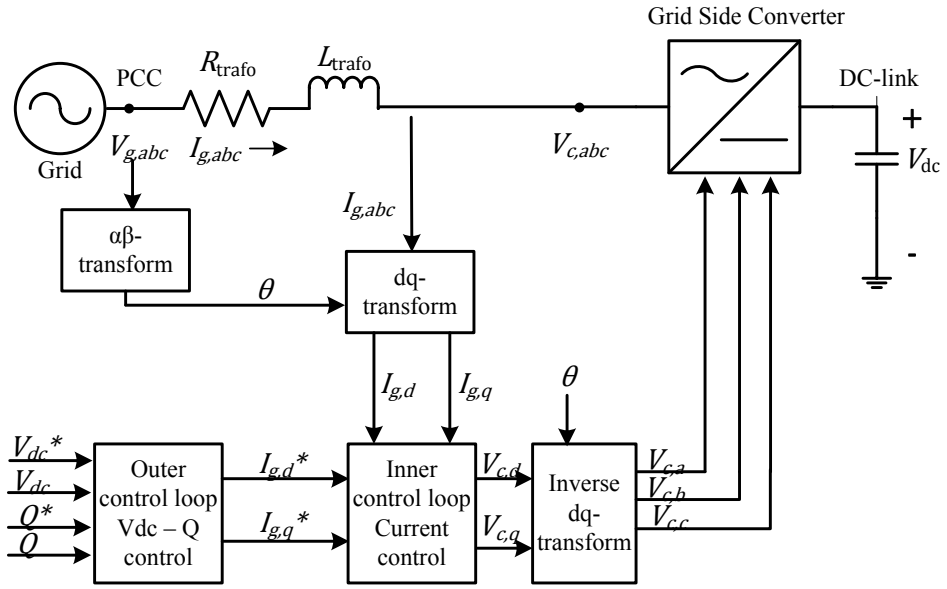

Figure 3-1 Grid side converter control system overview

3.1.1 Inner Control Loop

The inner control loop is controlling the current on the line between the PCC and the VSC, by controlling the voltage at the converter terminals.

The three phase currents flowing through the transformer equivalent resistance and impedance $i_{g,abc}$ are measured expressed as space vector $\overrightarrow{i_g}$ before it is transformed to the synchronously rotating dq-frame. Due to the fixed frequency of the grid, three-phase currents will have a constant frequency and, when referred to the synchronously rotating dq-reference frame, they will be DC-quantities.

The grid voltage $V_{g,abc}$ and the converter voltage $V_{c,abc}$ can also be expressed as space vectors $\overrightarrow{V_g}$ and $\overrightarrow{V_c}$, based on equation (2-1) and (2-2). $\overrightarrow{V_g}$ is aligned with the dq-reference frame d-axis, and the angle between the rotating d-axis and the phase a-axis of the grid voltage is defined as θ_{da}. The grid voltage q-axis component will at all times be equal to zero, due to the stiff grid frequency.

The mathematical model of the grid side system is found by the equation of the voltage drop on the line between the PCC and the VSC, as follows

$$\overrightarrow{V_g} - \overrightarrow{V_c} = R_{\text{trafo}}\overrightarrow{i_g} + L_{\text{trafo}}\frac{d\overrightarrow{i_g}}{dt} \tag{3-1}$$

The voltage invariant dq- transform, provided in section 2.1 is used to transform the space vector equation to the dq-plane. The d-component equation is given as follows

$$V_{gd} - V_{cd} = R_{\text{trafo}}i_{gd} + L_{\text{trafo}}\frac{di_{gd}}{dt} - \omega_d L_{\text{trafo}}i_{gq} \tag{3-2}$$

and the q-component equation is given as

$$V_{gq} - V_{cq} = R_{\text{trafo}}i_{gq} + L_{\text{trafo}}\frac{di_{gq}}{dt} + \omega_d L_{\text{trafo}}i_{gd} \tag{3-3}$$

The obtained current differential equation can be expressed on matrix form as follows [22]

$$L_{\text{trafo}}\frac{d}{dt}\begin{bmatrix} i_{gd} \\ i_{gq} \end{bmatrix} = \begin{bmatrix} V_{gd} \\ V_{gq} \end{bmatrix} - \begin{bmatrix} V_{cd} \\ V_{cq} \end{bmatrix} - R\begin{bmatrix} i_{gd} \\ i_{gq} \end{bmatrix} + \omega_d L_{\text{trafo}}\begin{bmatrix} 0 & 1 \\ -1 & 0 \end{bmatrix}\begin{bmatrix} i_{gd} \\ i_{gq} \end{bmatrix} \tag{3-4}$$

As can be seen from equation (3-4), the d and q-components are coupled. To enable decoupled control of both i_{gd} and i_{gq}, they need to be fed forward. Decoupled control of the current d- and q-control enables decoupled control of the DC-link voltage and reactive power. The grid voltage V_g is also fed forward. The resistance multiplied by the current term need not to be fed forward, since it is contributing to the damping of the system.

The system controller is based on this, expressed as follows

$$\begin{bmatrix} V_{cd} \\ V_{cq} \end{bmatrix} = \omega_d L_{\text{trafo}} \begin{bmatrix} 0 & 1 \\ -1 & 0 \end{bmatrix} \begin{bmatrix} i_{gd} \\ i_{gq} \end{bmatrix} + \begin{bmatrix} v_{gd} \\ v_{gq} \end{bmatrix} + K_{p,i} \begin{bmatrix} e_d \\ e_q \end{bmatrix} + K_{i,i} \int_0^t \begin{bmatrix} e_d \\ e_q \end{bmatrix} dt \quad (3\text{-}5)$$

where e_d and e_q are the errors fed into the controller, $K_{p,i}$ is the proportional gain of the controller, $K_{i,i}$ is the integral gain of the controller. The resulting inner current control loop block diagram can be seen in Figure 3-2.

Equation (3-4) and (3-5) describes the full mathematical model of the system and the controller.

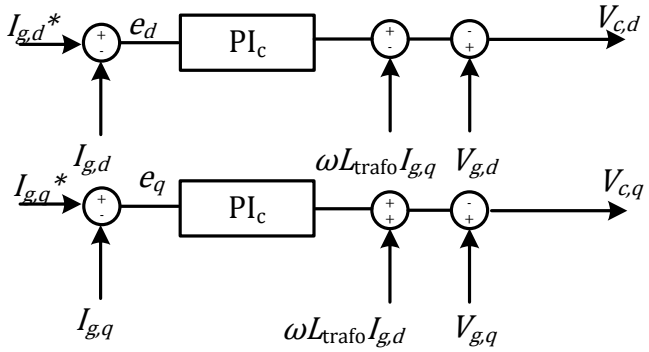

Figure 3-2 Inner current control loop block diagram

3.1.2 Outer Control Loop

The outer control loops are controlling the DC-link voltage and the reactive power at the PCC, by applying references for the d-and q-component inner current control loops respectively. By aligning the grid voltage space vector $\overrightarrow{V_g}$ with the dq-reference frame d-axis, it will be shown that the DC-link voltage can be controlled by controlling the d-axis current, while the reactive power can be controlled by controlling the q-axis current.

3.1.2.1 DC-voltage control

For developing a control strategy for DC-link voltage control, a mathematical model for the relation between the AC and the DC-side of the grid side converter system is needed. This relation can be described based on the power conservation equations and the equation for the DC-link voltage, as follows [38]

$$I_{\text{cap}} = C \frac{dV_{dc}}{dt} \quad (3\text{-}6)$$

where C is the DC-link capacitance and I_{cap} is the current running through the DC-link capacitor.

Equation (2-10) substituted into equation (2-9), when V_{gq} is known to be zero gives

$$\frac{3}{2}V_{gd}i_{gd} = V_{\mathrm{dc}}(I_{\mathrm{cap}} + I_{\mathrm{dc2}}) \tag{3-7}$$

Equation (3-6) can be substituted into (3-7)

$$\frac{3}{2}V_{gd}i_{gd} = V_{\mathrm{dc}}\left(C\frac{dV_{\mathrm{dc}}}{dt} + I_{\mathrm{dc2}}\right) \tag{3-8}$$

This can be rearranged to the following form

$$\frac{dV_{\mathrm{dc}}}{dt} = \frac{3}{2}\frac{V_{gd}}{CV_{\mathrm{dc}}}i_{gd} - \frac{V_{\mathrm{dc}}}{CV_{gd}}I_{\mathrm{dc2}} \tag{3-9}$$

There is a strong correlation between the DC-voltage V_{dc} and the AC-system d-axis current i_{gd}, and hence the DC-link voltage should be controlled using the d-axis current component. The relation between them is, as can be seen from equation (3-9), not linear. The system can be linearized around the reference values by Taylor series expansion [28]. The linearized system is based on gross assumptions, and is only a simplification of the real system model. The linear system can be expressed as follows

$$\frac{dV_{\mathrm{dc}}}{dt} = \frac{3}{2}\frac{V_{gd,0}}{CV_{\mathrm{dc,ref}}}i_{gd} \tag{3-10}$$

where the term $\frac{V_{gd,0}}{V_{\mathrm{dc,ref}}}$ is assumed to be constant. This gives a linear relation between the DC-link voltage and the grid current, and PI-controllers could be used for control of the DC-link voltage.

The DC-controller provides the inner active current control loop with its reference. The line current should not however be set larger than the rated current of the grid side system. To avoid this, a current limiter or saturator is set to limit the active current as follows

$$i^*_{d,\max/\min} = \pm 1 \tag{3-11}$$

The outer DC-voltage control loop can be seen in Figure 3-3.

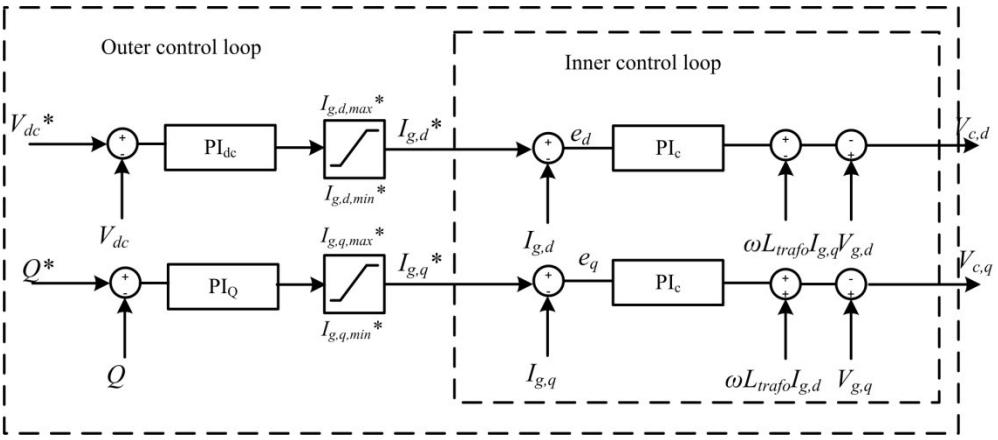

Figure 3-3 Grid side VSC control block diagram

3.1.2.2 Reactive power control

The purpose of the reactive power control is to keep the reactive power consumed by the converter system equal to zero at the PCC. The reactive power supplied or consumed at the PCC can be expressed relative to the dq-reference frame, with the voltage space vector of the grid voltage space vector $\overrightarrow{V_g}$ aligned with the d-axis, making the q-component V_{gq} equal to zero [13].

$$Q = -\frac{3}{2} v_{gd} i_{gq} \tag{3-12}$$

This shows that the reactive power can be controlled directly through controlling the reactive current component i_{gq}.

The difference between the reactive power reference and the measured reactive power at the PCC is fed into a PI-controller, with the reactive current reference i_{gq}^* as the output of the controller. There is no need for any feed-forward compensation terms for the reactive power controller.

The reactive power controller is providing the inner reactive current control loop with its reference. The total rated current of the grid side system should not be set above its rated value. Therefore a dynamic current limiter or saturator will be set to satisfy the following condition, based on the measured active current reference i_d^* [19]

$$i_{q,\max/\min}^* = \pm\sqrt{{i_{d,\max}^*}^2 - {i_d^*}^2} \tag{3-13}$$

The full grid side converter control system obtained through the control strategies presented in this chapter can be seen in Figure 3-3.

3.2 Platform Side Converter Control

The control objectives of the platform side converter controller are to maintain the platform voltage and frequency within the acceptable range defined in Table 1-1, for all realistic changes in platform load. This will be done through the type 1 controller defined in section 2.3.3. The platform load is defined in section 2.5 and consists of a passive load, an accumulated induction machine model and a smaller induction machine. The load is non-linear and unknown at time t, which poses challenges for the voltage and frequency controllers. They have to be able to regulate the voltage and frequency during changes in active and reactive power consumed on the platform due to induction machine starting, and other frequent load changes. Without proper control the performance and even the stability of the passive network with varying non-linear load can be jeopardized.

This control problem has formerly been addressed with several control strategies. Classical control methods, based on simple PI-controllers, where the voltage magnitude is controlled and the frequency is fixed have been proposed by [38, 39], and are applied in several other publications. In [40] a voltage control strategy based on the steady-state equations of the VSC passive system side is proposed. The passive system load is assumed to be a constant impedance load. The VSC output voltage is controlled by controlling the load voltage d-and q-components, through PI-controllers, and compensating terms for the filter inductance steady-state voltage drop are included in the model. A classical voltage and frequency control approach with a current mode control scheme, a synchronous dq-reference frame and a phase lock loop (PLL) has been suggested in [41]. A dynamic VSC passive system side mathematical model is applied; with variable frequency feed forward compensation terms for decoupled control of the voltage d-and q-components fed into the inner current control loop. The load is assumed to be unknown and possibly non-linear. In [42], a fuzzy controller strategy has been proposed for VSC voltage control in passive systems, the load is assumed to be a known RL-load. A robust control strategy is proposed in [43], where a RLC-load with uncertain parameters are defined as a frequently changing load.

Adaptive control or robust control methods could ensure stability and performance for variable loads or load changes. However, this is considered to be out of the scope of this thesis, and classical control methods for controlling the platform voltage and frequency are the only control methods considered.

Two different approaches for voltage and frequency control of the platform passive network will be presented here. The first control system to be modeled and implemented is a simple platform voltage magnitude controller that is based on the control strategy described in [38, 39]. The second voltage control strategy is a based on [41]. Throughout this thesis the voltage control strategies will be called control strategy 1 and control strategy 2. The control tuning will be presented in chapter 4 .

3.2.1 Control Strategy 1

Control strategy 1 is illustrated by Figure 3-4, and shows that the platform RMS-voltage is controlled by controlling the shore converter output RMS-voltage $|V_l|$. The platform load is unknown, and there are two ideal transformers and an 80 km HVAC-cable between the platform side VSC and the platform.

There is a stiff frequency applied to the system ωt, and hence no frequency control is implemented.

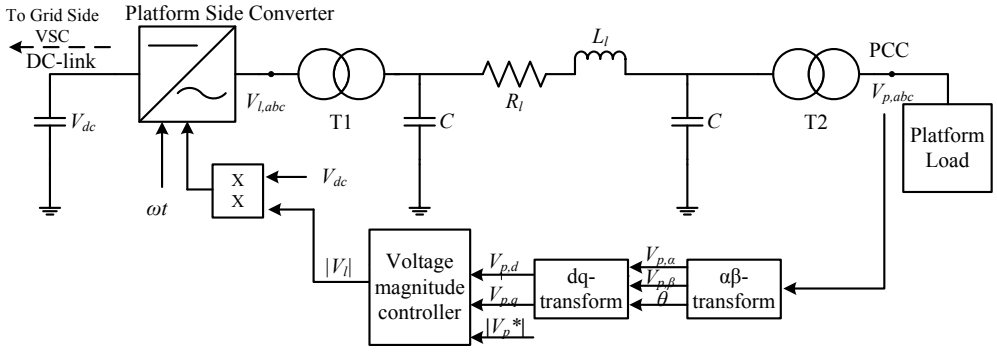

Figure 3-4 Platform-side converter control strategy 1

It can be seen from Figure 3-4 that the platform voltage is measured, and the Clarke-transform provides the αβ-components of the platform voltage and the voltage phase angle θ. This is used to transform the platform voltage to dq-components where the d-axis is aligned with the three-phase system a-axis, and the q-axis is leading by 90 degrees, see section 2.1. The platform voltage is aligned with the reference frame d-axis.

The voltage control method is, as previously stated, based on controlling the RMS platform voltage. Early RMS-value calculation methods were based on calculating the RMS-value over one period of the voltage waveform, which would introduce a time delay of one period at the input to the controller [39]. Now it is more common to use the instantaneous RMS-value, which is calculated based on the voltage space vector [39]. The voltage space vector can, as described in section 2.1, be decomposed into $V_{p,d}$ and $V_{p,q}$ components. The instantaneous RMS voltage, $|V_p|$ can after this transform be expressed as follows

$$|V_p| = \sqrt{v_{p,d}^2 + v_{p,q}^2} \tag{3-14}$$

The voltage magnitude control strategy was chosen based on the steady-state mathematical modeling of the system in [39]. It has been modified to fit the proposed system, and is presented below.

Equation (2-14) can be rewritten to express the platform side shore based converter output voltage [16]

$$V_{\mathrm{l,LL,RMS}} = \frac{\sqrt{3}}{2\sqrt{2}} |V_l| V_{\mathrm{dc}} \tag{3-15}$$

If the total line impedance in steady-state is expressed by Z_{line} and the platform load can by Z_L, the relation between the platform voltage and the converter output voltage is found to be

$$V_{\mathrm{p,LL,RMS}} = \frac{Z_{\mathrm{line}}}{Z_L + Z_{\mathrm{line}}} V_{\mathrm{l,LL,RMS}} \tag{3-16}$$

Equation (3-15) substituted into equation (3-16) gives the following expression [39]

$$V_{\mathrm{p,LL,RMS}} = \frac{\sqrt{3}}{2\sqrt{2}} \frac{Z_{\mathrm{line}}}{Z_L + Z_{\mathrm{line}}} |V_l| V_{dc} \tag{3-17}$$

The DC-link voltage is controlled by the grid side converter and assumed to be constant, the converter output RMS-voltage magnitude $|V_l|$ is the controlling variable, and V_p is the controlled variable. Equation (3-17) shows that the relation between $|V_l|$ and V_p in steady-state is linear, and hence a PI-controller can be used to control the platform voltage [39].

The difference between the calculated instantaneous RMS platform voltage and the reference platform voltage is applied to a simple PI-controller, where the VSC output RMS- voltage $|V_l|$ is the output of the controller, see Figure 3-5.

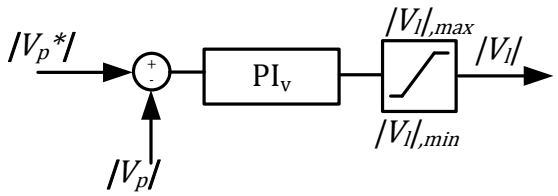

Figure 3-5 Platform voltage controller block diagram

Generation of the reference voltage signal for the controlled voltage sources is illustrated in Figure 3-6, and is based on the signal modeling done in [19] for passive network AC-voltage control.

The applied angle ωt is increasing linear with time, and the angular frequency is constant.

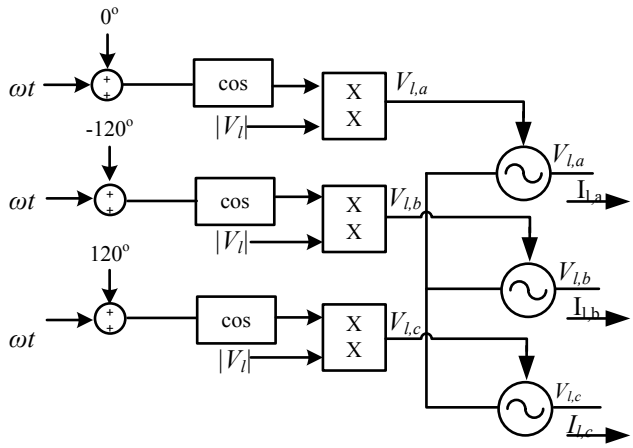

Figure 3-6 Generating platform side converter controlled voltage source input signal

There are several weaknesses in this controller model when it is applied for the system studied in this thesis. The mathematical model is based on steady-state equations assuming a linear relation between the shore voltage and the platform voltage. This is not valid for non-linear loads and load switching transients. The load of an oil platform is complex, and the control model does not include any compensation for load dynamics. Tests will show if the control strategy will be able to recover the voltage during and after transients within the required limits defined in Table 1-1.

3.2.2 Control Strategy 2

Control strategy 2 is a cascaded control strategy, consisting of an inner current control loop; controlling the platform-side shore based VSC output voltage $V_{l,abc}$, outer voltage control loops; providing the inner current control loops with their references, and a third outer control loop; controlling the platform angular frequency. A phase lock loop (PLL) is also implemented for providing the platform voltage phase angle θ to the voltage dq-transform. The control strategy is illustrated in Figure 3-7.

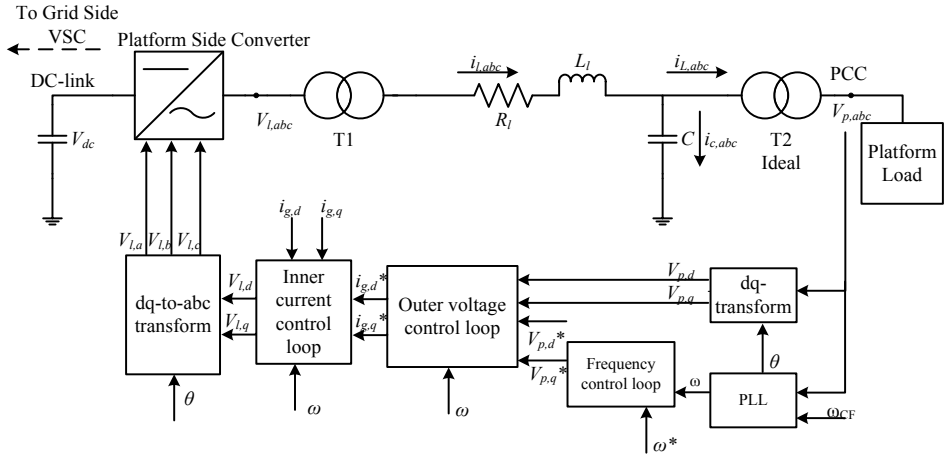

Figure 3-7 Platform voltage control strategy 2

This control strategy has previously been implemented and tested in [41], for controlling the voltage at the node of the VSC output filter capacitance. Implementation of this control strategy in a system as the proposed system, for controlling the voltage above a capacitor on an oil platform, separated from the shore based VSC by an 80 km HVAC-cable and transformers, has not been found in literature.

Control strategy 2 controls both the platform voltage magnitude and frequency, and the control strategy is based on conventional control strategies that would be implemented for a weak grid system. This is particularly advantageous for electrification of an oil platform, because most platforms that are provided with power from shore would have a synchronous generator operating on the platform for process heat or backup. Expensive additional equipment for controlling the system when the synchronous generator is disconnected might not be considered. This control strategy would only require small modifications in the weak grid control system to allow for passive system control, which would make it possible to reduce the usage of, or for eliminating the low efficiency, high emissions gas turbine on the platform.

This section will provide the mathematical models for each of the cascaded control loops and the phase lock loop. Tuning results will be provided in section 4.2.2.

3.2.2.1 Phase Lock Loop

A phase lock loop (PLL) is used to track the phase and frequency of the platform voltage, that is used for voltage and frequency control of the passive platform system. The PLL implemented is based on the synchronous reference frame (SRF) PLL described in [44] and is expanded to include the feed-forward center frequency

term, introduced in [45]. The PLL presented in [45] is proven to have better performance while also having better noise rejection in variable frequency systems.

The PLL configuration is illustrated by Figure 3-8, and it can be seen that the three-phase voltage is transformed to the dq-reference frame, using the estimated phase angle. When the voltage q-component is equal to zero, the phase angle is equal to the actual phase angle of the voltage. The desired system frequency is fed-forward after the PI-control block. This feed forward frequency is called the center frequency ω_{CF}, and is ~377 rad/s for this system. Due to the feed-forward frequency term, the PI-controller only has to eliminate the phase angle error, and not the frequency variations [45].

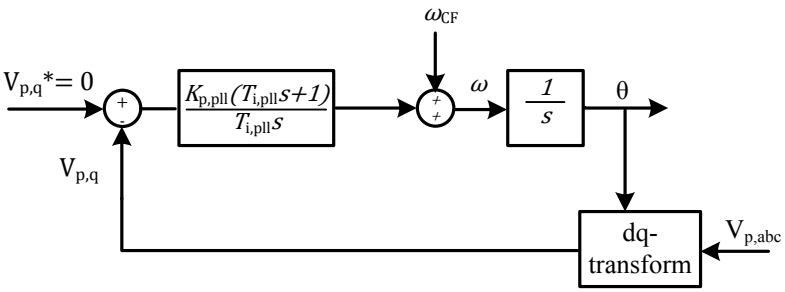

Figure 3-8 Block diagram of PLL

3.2.2.2 Inner Current Control Loop

The inner current control loop used for this controller has the same structure and mathematical model as inner current control loop developed for DC-link voltage and reactive power control, with a few exceptions.

Since the shore transformer is non-ideal, it introduces impedance and resistance to the line equivalent circuit. This should be taken into account when developing the differential equations for the line current. The total impedance is denoted as L_{tot} and is expressed as follows

$$L_{\text{tot}} = L_{\text{cable}} + L_{\text{T1}} \tag{3-18}$$

The total resistance is denoted as R_{tot} and is expressed as follows

$$R_{\text{tot}} = R_{\text{cable}} + R_{\text{T1}} \tag{3-19}$$

The differential equations for the dq- line currents flowing on the platform system line are therefore given as follows

$$L_{\text{tot}} \frac{d}{dt} \begin{bmatrix} i_{l,d} \\ i_{l,q} \end{bmatrix} = \begin{bmatrix} V_{l,d} \\ V_{l,q} \end{bmatrix} - \begin{bmatrix} V_{p,d} \\ V_{p,q} \end{bmatrix} - R_{tot} \begin{bmatrix} i_{l,d} \\ i_{l,q} \end{bmatrix} + \omega L_{\text{tot}} \begin{bmatrix} 0 & 1 \\ -1 & 0 \end{bmatrix} \begin{bmatrix} i_{l,d} \\ i_{l,q} \end{bmatrix} \tag{3-20}$$

It can be seen from this equation that the current d- and q-components are coupled. To allow for decoupled control, these terms are fed forward. The frequency of the passive platform system is not fixed as it is on the grid side system, and the current feed-forward compensating terms are dependent on the varying frequency. Since the frequency controller should maintain the frequency at an allowable range for the system, the fixed angular frequency of 377 rad/ s is used in the feed-forward terms this current control loop as well. The platform voltage terms are also fed forward. The total resistance multiplied by the current term need not to be fed forward, since it is contributing to the damping of the system.

A PI-controller will be used for the current control loop, and the full current controller is expressed by the following equation

$$\begin{bmatrix} V_{l,d} \\ V_{l,q} \end{bmatrix} = -\omega L_{\text{tot}} \begin{bmatrix} 0 & 1 \\ -1 & 0 \end{bmatrix} \begin{bmatrix} i_{l,d} \\ i_{l,q} \end{bmatrix} + \begin{bmatrix} v_{p,d} \\ v_{p,q} \end{bmatrix} + K_{p,i} \begin{bmatrix} e_d \\ e_q \end{bmatrix} + K_{i,i} \int_0^t \begin{bmatrix} e_d \\ e_q \end{bmatrix} dt \qquad (3\text{-}21)$$

(3-20) and (3-21) complete the inner current control loop of control strategy 2. The block diagram of the current controller can be seen in Figure 3-9.

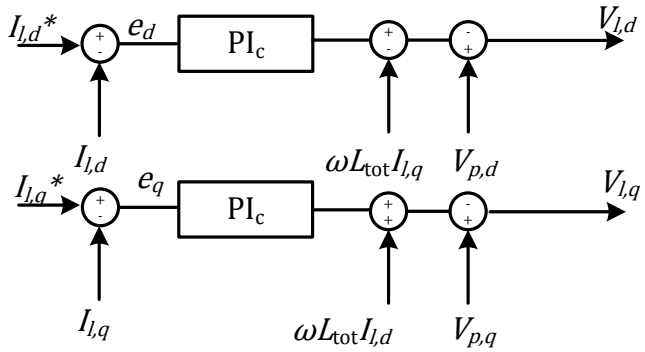

Figure 3-9 Block diagram for inner current control loops

3.2.2.3 Outer Voltage Control Loop

The platform system model used for developing the mathematical model of the outer voltage control loops is shown in Figure 3-10. The pi-equivalent cable model has been modified for implementation of control strategy 2, by removing the shore based pi-equivalent capacitance. This is done because the controlled current is the current flowing into the platform-side pi-equivalent capacitance node. If the shore-side pi-equivalent capacitance was there, the VSC output current would not be equivalent to the current to be controlled. This would require modification of the control structure, which is suggested as future work.

The shore transformer is non-ideal, while the platform transformer is assumed to be ideal. The platform voltage $V_{p,abc}$ is going to be controlled by controlling $I_{l,abc}$, that is the current flowing through the cable lumped parameters L_l and R_l. $I_{L,abc}$ is the current consumed by the platform load and $I_{c2,abc}$ is the current consumed by the platform side lumped capacitor C_{l2}.

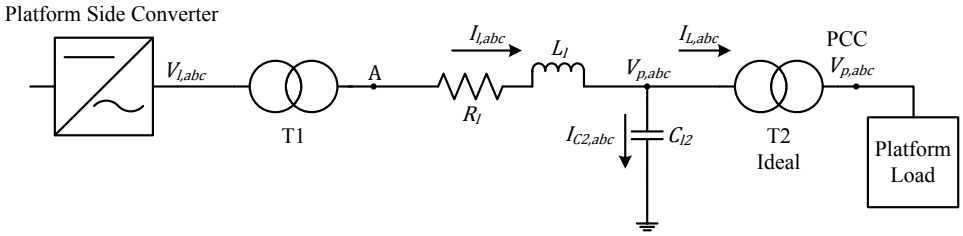

Figure 3-10 System model used for developing controller equations for voltage control strategy 2

All three-phase quantities are transformed with respect to the rotating dq-reference frame. As explained in section 3.2.2.1, the platform q-axis voltage component $v_{p,q}$ is forced to zero by the PLL, the platform voltage q-component is also used to control the platform frequency. The platform d-axis voltage $v_{p,d}$ will be controlling the platform voltage magnitude.

Control of $v_{p,d}$ and $v_{p,q}$ in this manner is not straight forward due to many factors. $v_{p,d}$ and $v_{p,q}$ are coupled, the relation between the controlled current $i_{l,dq}$ and the voltages is highly non-linear, the load current $i_{L,dq}$ are functions of both $v_{p,d}$ and $v_{p,q}$. It is also shown in [41] that the dynamics of a simple RL-load or RLC-load is non-linear and of high dynamic order [41]. The load on a platform system is much more complex than RLC-loads, and hence would introduce complex current dynamics.

The control scheme that is presented here, developed by [41], has shown to largely overcome these issues, and is therefore of interest for the purpose of passive system platform voltage and frequency control.

The platform voltage space vector $\overrightarrow{V_{p,abc}}$, is the voltage over the lumped capacitance. The equation for voltage over a capacitor is expressed as follows

$$C_{l2}\frac{d\overrightarrow{V_{p,abc}}}{dt} = \overrightarrow{I_{l,abc}} - \overrightarrow{I_{L,abc}} \tag{3-22}$$

This can be expressed with respect to the d-axis as follows

$$C_{l2}\frac{dV_{p,d}}{dt} = \omega_2 C_{l2} V_{p,q} + I_{l,d} - I_{L,d} \tag{3-23}$$

The q-axis equation is given as follows

$$C_{l2}\frac{dV_{p,q}}{dt} = -\omega_2 C_{l2} V_{p,d} + I_{l,q} - I_{L,q} \tag{3-24}$$

It can be seen from (3-23) and (3-24) that the d- and q-axis voltage components are coupled. These terms will be fed forward and multiplied with the fixed variable frequency of 377 rad/s and the capacitance. This is done to allow for decoupled control. The frequency of the passive system is not fixed, and hence the voltage feed-forward decoupling terms are dependent on the variable frequency. Since the frequency controller should maintain the frequency at an allowable range for the system, the fixed angular frequency of 377 rad/ s is used in the feed-forward terms of the outer voltage loops.

The load currents are also fed forward to mitigate the impact of load dynamics on the system, which may have a significant influence on the system stability and performance for some types of platform loads.

The transient terms of (3-23) and (3-24), when transformed to the Laplace domain, are proved to be negligible if the time constant of the inner current control loop is small enough [41]. The relationship between the d- and q- axis platform voltage and the dq-line current can then be assumed to be linear, and hence PI-controllers can be used to ensure fast and stable response of the outer control loop.

The outer voltage control loops can therefore be expressed as follows

$$\begin{bmatrix} I_{l,d} \\ I_{l,q} \end{bmatrix} = \omega_2 C_{l2} \begin{bmatrix} 0 & -1 \\ 1 & 0 \end{bmatrix} \begin{bmatrix} V_{p,d} \\ V_{p,q} \end{bmatrix} + \begin{bmatrix} i_{L,d} \\ i_{L,q} \end{bmatrix} + K_{p,v} \begin{bmatrix} e_d \\ e_q \end{bmatrix} + K_{i,v} \int_0^t \begin{bmatrix} e_d \\ e_q \end{bmatrix} dt \tag{3-25}$$

These equations complete the outer loop control model for the system shown in Figure 3-10.

The block diagram of the cascaded control system with the inner and outer control loops are shown in Figure 3-11. The reference for the d-axis voltage $v_{p,d}^*$, is set to the desired platform voltage magnitude. The reference for the q-axis voltage $v_{p,q}^*$ is provided by the outer frequency control loop described in section 3.2.2.4.

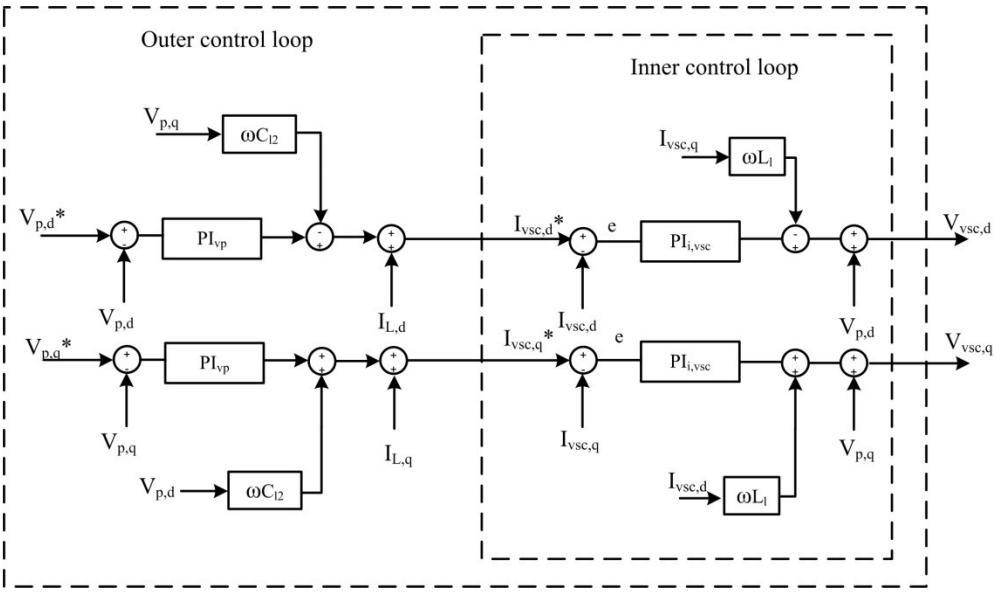

Figure 3-11 Block diagram of outer platform voltage controller, and inner current controller

The pi-equivalent cable model is only a simplified model of a real HVAC-cable, as was discussed in section 2.4.3. The capacitors only model the behavior of the cable at each end, and there are no physical capacitors on shore or on the platform. To be able to apply this voltage control strategy to a real system as such, a physical capacitor should be added at the platform side. If the current and voltage that the shore VSC must provide in order to obtain the desired current at the platform physical capacitor could be calculated, the voltage $V_{p,abc}$ over the capacitor could be controlled. The realistic platform side system model is shown in Figure 3-12.

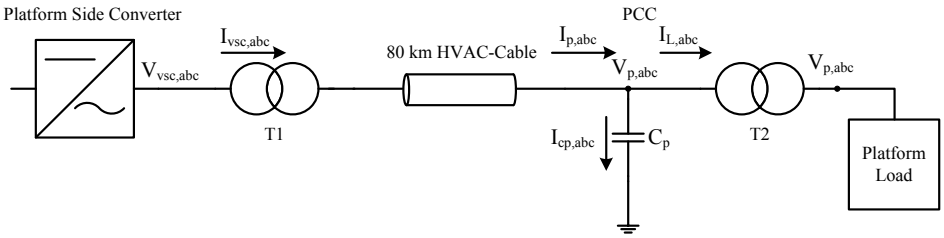

Figure 3-12 Realistic platform side system model

The VSC current output can be calculated if the dynamic relation between the shore VSC current and the current at the end of the 80 km HVAC-cable can be estimated. This relation is simplified as follows

$$I_{\mathrm{p,abc}} = I_{\mathrm{vsc,abc}} - I_{\mathrm{cable,abc}} \tag{3-26}$$

where $I_{\mathrm{p,abc}}$ is the measured current flowing into the PCC, $I_{\mathrm{vsc,abc}}$ is the current applied by the VSC on shore, and $I_{\mathrm{cable,abc}}$ is the current absorbed or supplied by the capacitive cable.

Dynamic and accurate estimation of the cable current $I_{cable,abc}$ would require an accurate mathematical model of the cable. This estimation is considered to be out of the scope of this thesis and is suggested as future work to make the controller applicable for a real platform system.

3.2.2.4 Frequency controller

The frequency control loop provides the q-axis control loop voltage $v_{p,q}$ with its reference. Due to the integrator in the PLL, the frequency controller only needs a proportional gain to control the frequency to a set reference ω^* of 377 rad/s, without any steady-state error [41]. The simple block diagram of the frequency controller can be seen in Figure 3-13.

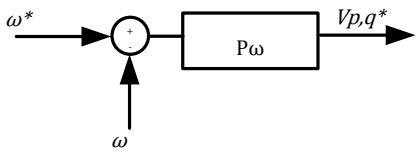

Figure 3-13 Block diagram for frequency controller, providing the platform voltage q-component with its reference

4 Tuning of Controllers

This chapter presents the tuning techniques applied for tuning of the controllers that were modeled in chapter 3 All the controllers to be tuned are based on PI-controllers, operating alone or in cascaded configurations. For a PI-controller there are two parameters to be tuned: proportional gain K_p, and integral time T_i. These parameters need to be set so that the speed of response and stability, for both small and large system disturbances are acceptable. Controllers that can track their references for large variations in platform load, fluctuations in the active and reactive power drawn, are more important than optimal performance for some system conditions.

The methods used for determining the PI-control parameters for each of the respective control configurations will be presented here. The system response for step changes in the references will be shown, and the controller performances will be evaluated.

Tuning of the grid-side VSC controllers will be presented in section 4.1, and the results from the tuning of the platform side VSC control strategies will be presented in section 4.2.

4.1 Tuning of Grid Side VSC Controllers

Tuning of the cascade control system with the inner current control loop, the outer DC-voltage and the outer reactive power control loop will be done in this section. Cascaded control requires the inner control loop to have a faster speed of response than the outer control loop. Therefore the inner current control loop is tuned to achieve fast response, while the outer control loops are tuned to achieve a stable system, with good regulation [28].

The “modulus optimum” criterion is used to tune inner current control loop, while the “symmetrical optimum” criterion will be used for tuning the outer DC-voltage loop. The outer reactive power control loop controller parameters will be determined based on testing a large range of controller parameters, and studying the system response for a step change test in the reactive power reference.

4.1.1 Inner Current Control Loop

The modulus optimum tuning criterion can be used to determine the control parameters of a PI-controller, when the plant consists of two poles in the left half plane (LHP), one of which is considerably smaller, and hence closer to the right half plane (RHP).

Modulus optimum is achieved through using the PI-controller to cancel the largest time constant of the system, which is equivalent to the pole closest to the RHP, while the closed loop gain is larger than unity for as large frequencies as possible [37].

For the system studied in this thesis the switching frequency of the VSC is, as previously described, assumed to be infinite. The average converter model used assumes infinite switching frequency. If the control parameters are dimensioned for a specific switching frequency the controller will be valid for both average converter models and switching converter models with this specific frequency. This is desirable, and the switching frequency is set to 1 kHz for determining the modulus optimum parameters.

As presented in section 3.1.1, the *dq*-transform of the three-phase currents results in DC-quantities that are controlled through feeding the error between the reference and the measured value through a PI-controller. The full linearized control scheme is shown in the block diagram shown in Figure 4-1.

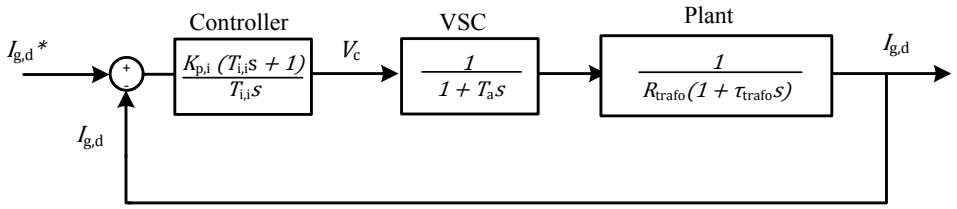

Figure 4-1 Reduced block diagram of grid-side current control scheme

The base value calculations of the values used to calculate the controller parameters are, with one exception, the same as the base values used throughout this thesis report, presented in section 2.6. The exception is for the inductance, where the per unit calculation is done as follows

$$L_{\text{pu}} = \frac{L_{\text{real}}}{Z_{\text{base}}} \tag{4-1}$$

Usage of this base value gives seconds as the result when calculating the system time constant with per unit values.

It can be seen in Figure 4-1 that the VSC is modeled as a time delay $T_a = \frac{1}{2*f_a}$, where f_a is the switching frequency of the VSC. The plant is the transfer function between the converter output voltage and current in the grid side system. This is expressed as follows

$$G_P(s) = \frac{1}{R_{\text{trafo}}}\left(\frac{1}{1+\tau_{\text{trafo}}s}\right) \tag{4-2}$$

where τ_{trafo} is the time constant of the LR-circuit defined as follows

$$\tau_{\text{trafo}} = \frac{L_{\text{trafo,pu}}}{R_{\text{trafo,pu}}} \tag{4-3}$$

The VSC time constant T_a is much smaller than the plant time constant τ_{trafo}, due to the high switching frequency. This means that the pole introduced by the VSC is further left than the pole introduced by the plant model, and the controller should be set to cancel the effect of the time constant of the plant rather than the time constant of the VSC.

The PI-controller integral time, based on the modulus optimum criterion is given as follows [37]

$$T_i = \tau_{\text{trafo}} \tag{4-4}$$

The proportional gain of the PI-controller is given as follows [37]

$$K_{p,pu} = \frac{\tau_{pu} R_{\text{trafo,pu}}}{2T_a} \tag{4-5}$$

In Simulink™, the integrator gain constant K_i is implemented. This value can be calculated based on the proportional gain and the integral time constant, as follows

$$K_i = \frac{K_p}{T_i} \tag{4-6}$$

The values obtained for the current control loop, calculated based on the equations presented above, are given in Table 4-1.

Table 4-1 PI-controller parameters for inner current control loop

Description	$K_{p,i}$ **[pu]**	$T_{i,i}$ **[s]**
Modulus optimum calculated, controller values	0.4879	0.04396

The current controller with the modulus optimum obtained parameters is tested for a step change in the respective d-and q-axis current references. At time t = 0.1 s, there is a step change in the d-axis current reference from 0 to 0.6 pu.

The resulting grid-current response can be seen in Figure 4-2. The d-axis current is tracking its reference within 5 ms, with no overshoot. The influence of the d-axis current step-change in the q-axis current component is very small.

At time t = 0.12 s, there is a step change in the q-axis current reference from 0 to 0.3 pu. The q-axis current is tracking its reference within 5 ms, with no overshoot.

The influence of the q-axis current step change in the d-axis current component is not visible. Based on these results it can be concluded that decoupled control of the d- and q-axis grid-current is successfully implemented. The current control loops have shown to provide fast tracking of its reference, with no overshoot.

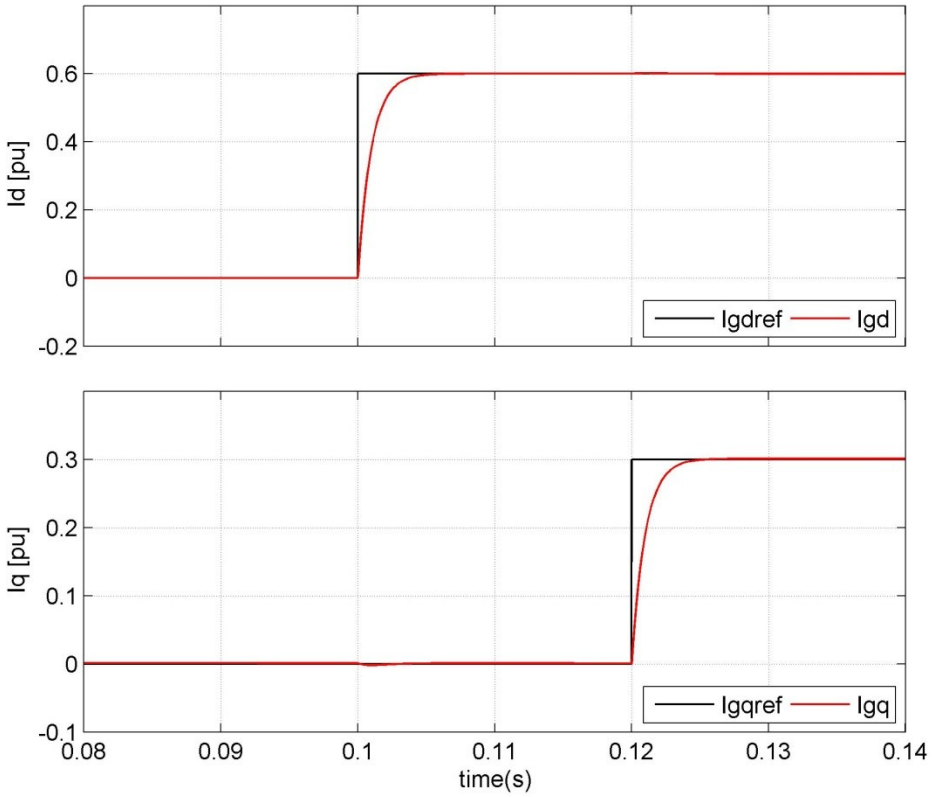

Figure 4-2 Grid current response for changes in the d- and q-current component references

4.1.2 Outer Control Loop

4.1.2.1 DC-voltage controller

For representing the DC-control loop on linear form the inner current control loop, presented in section 4.1.1, is simplified to an equivalent time delay T_{eq}. The value for the equivalent time delay has been found to vary in literature. For this system it is set to $4T_a$ in [37]. The outer DC-control loop cannot have an integral time constant smaller than this value.

The plant model is represented based on the power conservation equations, and the DC-link capacitance voltage equation, both given in section 2.3. This can be seen in the reduced block diagram for the DC-voltage control scheme, presented in Figure 4-3.

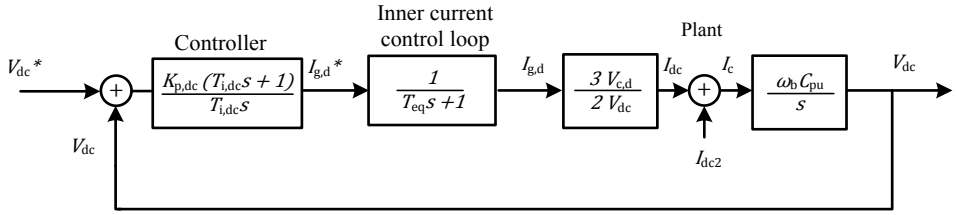

Figure 4-3 Reduced block diagram for DC-voltage control scheme

The open loop system transfer function, ignoring the feed forward term, is given as follows

$$G_{\mathrm{DC,OL}} = K_p \left(\frac{T_{i,dc}s+1}{T_{i,dc}s}\right)\left(\frac{1}{T_{eq}s+1}\right)\left(\frac{3V_{c,d}}{2V_{dc}}\right)\frac{\omega_b C_{pu}}{s} \tag{4-7}$$

The open loop transfer function in (4-7) has a multinomial polynomial in the denominator and the number of integrators are 2. If the controller parameters were set to cancel the inner current control loop time constant, there would be two poles at the origin and the system would be unstable. The symmetrical optimum method is specially suitable for determining the control parameters for a system as such [46], and is therefore applied here.

The smallest integral time constant that should be used for the controller is given by the symmetrical optimum method as follows [28]

$$T_{i,dc} = a^2 T_{eq} \tag{4-8}$$

The constant parameter a influences the pole placement of the closed loop transfer function and hence the damping factor. Both $a = 2$ and $a = 3$ are used in literature [37] [46], $a = 3$ is chosen for this controller. As seen from equation (4-8), a larger value for a gives a slower controller since the integral time increases with the square of a. A larger a also gives a larger phase margin [37].

The controller gain for the DC-link controller can be given as follows [37]

$$K_{p,dc,pu} = \frac{\left(\frac{1}{\omega_b C_{pu}}\right)}{\frac{V_{c,d}}{V_{dc}}\sqrt{T_{i,dc}T_{eq}}} \tag{4-9}$$

The parameters for the system DC-voltage controller are calculated based on the equations presented, and given in Table 4-2.

Table 4-2 PI-controller values for outer DC-voltage control loop

Description	$K_{p,dc}$ **[pu]**	$T_{i,dc}$ **[s]**
Symmetrical optimum, DC-voltage controller values	4.267	0.018

The grid-side system with the DC-voltage controller is tested for a step change in the DC-voltage reference from 1 pu to 1.5 pu, at time t = 0.3 s. This test is done to study the performance of the DC-controller. For normal operation the controller will have a constant reference, equal to 1 pu, since its task is to keep the DC-voltage at a constant level.

The step change test is applied for the system, first with the integral time $T_{i,dc}$ kept constant at 0.018 s, while the proportional gain $K_{p,dc}$ of the controller is varied to see the influence the proportional gain has on the step response. The result can be seen in Figure 4-4, where proportional gains below and above the symmetrical optimum criterion determined value shows larger overshoots and slower reference tracking. The step response with the symmetrical optimum obtained parameters provides the fastest step response, that tracks the reference within 0.06 s and with an overshoot of 25%, which is the smallest overshoot of all the proportional gains tested.

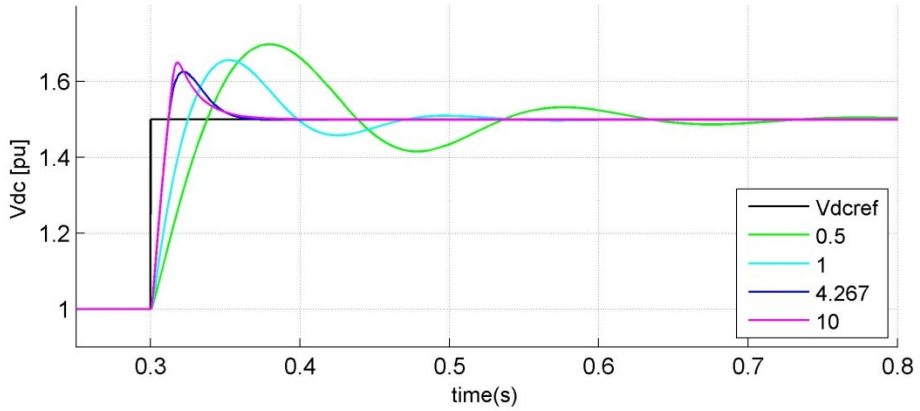

Figure 4-4 DC-controller step response for different controller proportional gains Kp, when Ti = 0.018

The step response test is then applied for the system, with the proportional gain kept constant at 4.267, while the integral time is varied. The symmetrical optimum calculated time constant is the smallest time constant that can be applied to the system, and hence only larger time constants are tested.

Figure 4-5 shows that the larger time constants provide slower tracking, but smaller overshoots. The symmetrical optimum calculated values overshoot of 25%

is not of concern since the DC-bus voltage reference is kept constant in a real system. For charging of the DC-bus capacitor the overshoot could be limited by ramping the voltage up to its reference value instead of introducing the large step change in dc-link voltage reference. The symmetrical optimum obtained values are therefore kept as the DC-link voltage controller parameters.

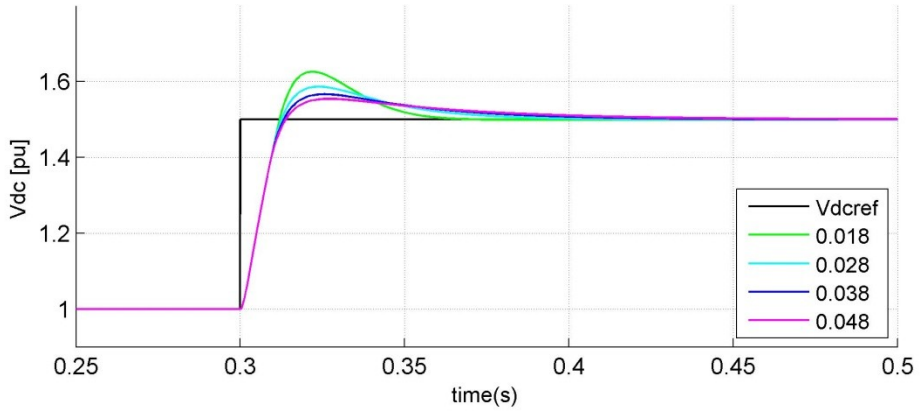

Figure 4-5 DC-voltage controller step response for different integral times Ti, when Kp = 4.267

4.1.2.2 Reactive power controller

The block diagram for the reactive power controller is presented in Figure 4-6, it consists of the PI-controller, the simplified current time delay which is defined in section 4.1.2.1. The plant model only consists of the grid d-axis voltage component, due to the simple relation between reactive power and the reactive current $i_{g,q}$, given in equation (3-15).

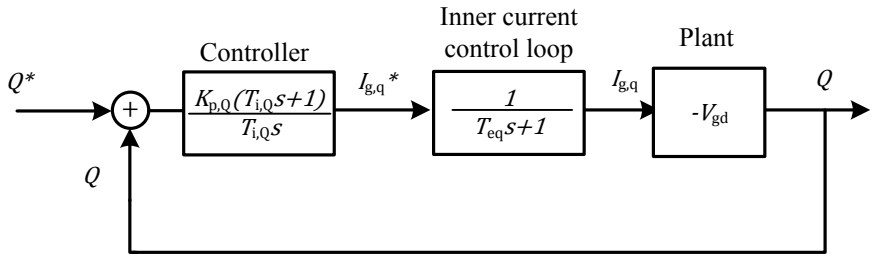

Figure 4-6 Block diagram for reactive power control scheme

The open loop transfer function for this system is given as follows

$$G_{Q,OL} = K_{p,Q}\left(\frac{T_{i,Q}s+1}{T_{iQ}s}\right)\left(\frac{1}{T_{eq}s+1}\right)(-v_{g,d}) \qquad (4\text{-}10)$$

This transfer function shows that if the reactive power control parameters are set to cancel the current control time delay, the resulting transfer function has one pole at zero, which will give a marginally stable system. This means that the modulus optimum method should not be applied for the system.

There is not straight forward to apply the symmetrical optimum method for this system [37, 46], since it is not on the general form described in [46]. Developing a mathematical tuning method for this controller is considered to be out of the scope of this thesis. The controller parameters will therefore be determined based on testing of a large range of different parameters for proportional gain $K_{p,Q}$ and integral time constants $T_{i,Q}$.

The reactive power controller is tested for a step response in its reactive power reference from 0.5 pu to 0 pu, for various proportional gains $K_{p,Q}$, while the integral time T_{iQ} of the reactive power controller is kept constant at 0.018 s. This integral time is the smallest that can be applied to the outer reactive power control loop, due to the inner current loop delay, defined in section 4.1.2.1. This is not a realistic test of the system behavior, since the reactive power reference will be zero at all times during normal system operation. The test is done to illustrate the ability of the controller to track the reference.

The system response to a step in the reactive power reference can be seen in Figure 4-7. The smaller the proportional gain is, the slower the tracking of the reference is. The largest proportional gain shown, $K_{pQ} = 20$ gives the fastest response**.** The increase of proportional gain from 10 to 20, gives a marginally faster response of less than 0.01 s. An increase of $K_{p,Q}$ beyond 40 gives an unstable system that is not able to track the reactive power reference.

Due to the focus of the robustness of the controller, instead of optimal reference tracking, the proportional gain of 10 is chosen for the reactive power controller.

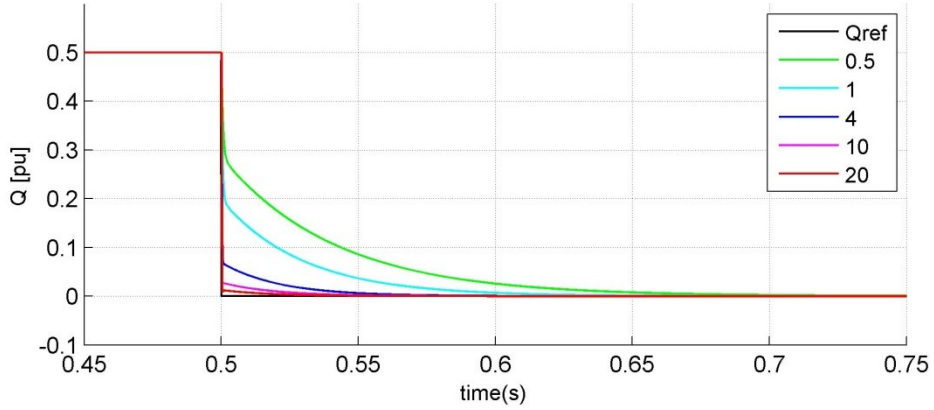

Figure 4-7 Reactive power controller step response for different controller proportional gains, when the integral time $T_{i,Q}$ is set to 0.018 s

The controller is then tested for a step response in the reactive power reference, when the controller proportional gain is kept constant to 10, and the integral time is varied. The results are presented in Figure 4-8, where it can be seen that the larger the time constant, the slower the reference tracking.

Based on these results, the integral time constant is set to 0.018 s. This provides a reference tracking in 0.08 s, with no overshoot. The reactive power controller parameters used are summarized in Table 4-3.

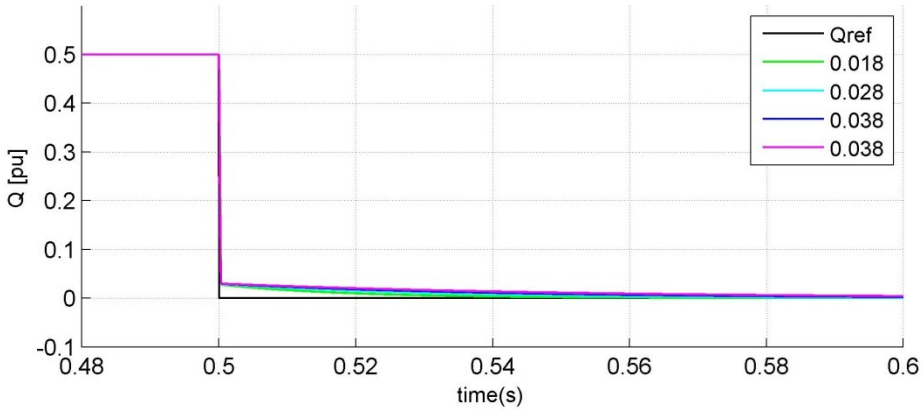

Figure 4-8 Reactive power controller step response for different integral time constants, when the controller proportional gain $K_{p,Q}$ is set to 10

Table 4-3 PI-controller parameters for reactive power controller

Description	$K_{p,Q}$ **[pu]**	$T_{i,Q}$ **[s]**
Reactive power controller values	10	0.018

4.2 Tuning of Platform Side VSC Controllers

The main objective of the platform side VSC controllers is to maintain the voltage and frequency of the platform system to its rated values, for all realistic changes in load. The platform load model is described in section 2.5, and due to load switching on the platform, the load is unknown at a random time t. This makes linearization of the platform load for tuning of the controller very difficult. As discussed in section 3.2, adaptive control or robust control methods with gain scheduling could ensure stability and optimal operation for a wide range of platform loads. However, this thesis is focused on using classical control methods, and adaptive and robust control methods are considered out of the scope. The PI-controllers used for platform voltage and frequency control are expected to regulate the platform voltage and frequency for a large range of load conditions, when only one proportional gain K_p and one integral time constant T_i is set. The main focus for the tuning of control strategy 1 and 2 is therefore to obtain controllers that will maintain stable systems for large load changes, while recovering the platform voltage within 1.5 seconds and the frequency within 5 seconds, as defined in the system requirements Table 1-1.

The platform load will during the tuning tests will consist of a 23 MVA induction machine operating in steady-state, with a power factor of 0.8, and a passive load of 2 MW. The results from the step change tests in the respective controller references will be shown and evaluated in this section.

4.2.1 Control Strategy 1

The block diagram of the system consisting of control strategy 1, the VSC and the plant can be seen in Figure 4-9. As described in section 4.2, determining the platform voltage controller parameters based on this model is not straight forward, due to the unknown platform load at time t.

The tuning of control strategy 1 will therefore be done through studying the response for a step change in the voltage magnitude reference $|V_p^*|$ for a large amount of proportional gains $K_{p,v}$, while keeping the integral time $T_{i,v}$ constant. When an appropriate value for the proportional gain is chosen, the system will be tested for various integral times, and the integral time $T_{i,v}$ providing the desired response will be determined.

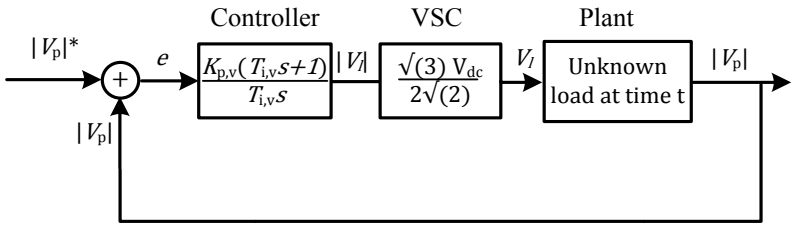

Figure 4-9 Block diagram for control strategy 1 controlling the voltage of the platform system

The integral time constant $T_{i,v}$ of the controller should not be smaller than the total time delay of the transformers and the HVAC-cable model. Simplifying the transformers and HVAC-cable to an RL-circuit, the total time delay based on the transformer leakage inductances and the cable accumulated RL-parameters is given as follows

$$\tau = \frac{L}{R} = \frac{32.238\ mH}{8.0018\ \Omega} \sim 0.004\ s \tag{4-11}$$

This gives the following restriction on the integral time constant

$$T_{i,v} > 0.004\ s \tag{4-12}$$

The initial controller integral time constant $T_{i,v}$ is initially set to 0.03 s, while the controller proportional gain is varied.

The system is applied a step change in the platform voltage magnitude reference $|V_p^*|$ at time 2 s, from 1 pu to 1.3 pu.

The system response for proportional gains of 0.1 and 0.08 can be seen in Figure 4-10 , larger proportional gains introduce oscillations in the response and thus are not suitable. Smaller gains than 0.08 give a slower response, and are therefore not depicted. It can be seen that the proportional gain of 0.1 provides a faster response than the proportional gain of 0.08. Since the proportional gain of 0.1 provides the fastest response without giving an overshoot, this gain is chosen for the controller.

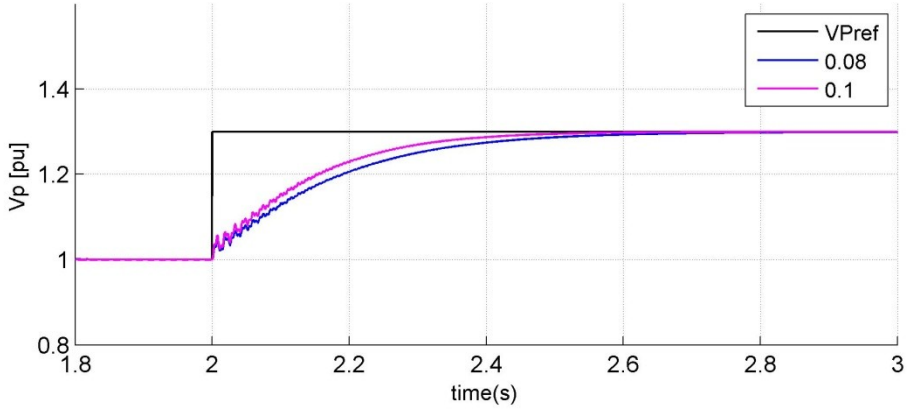

Figure 4-10 Voltage step response for system, tested for different proportional gains $K_{p,v}$, when the integral time $T_{i,v}$ is kept constant at 0.03 s

The controller is then tested for the same step change in reference, for various integral time constants $T_{i,v}$, when the proportional gain is kept constant at 0.1. The result from the test can be seen in Figure 4-11. The results show that the smaller the time constant is, the faster the reference voltage is tracked. The overshoot increases with a decreasing integral time constant. The controller should ensure system stability for large changes of load, and an overshoot in the response is not desirable. The integral time constant providing the fastest response, while not having an overshoot is 0.02 s, and is the integral time chosen for the controller.

The controller parameters determined based on this tuning are summarized in Table 4-4. The controller response, with these parameters tracks the reference within ~ 0.35 s, with no overshoot.

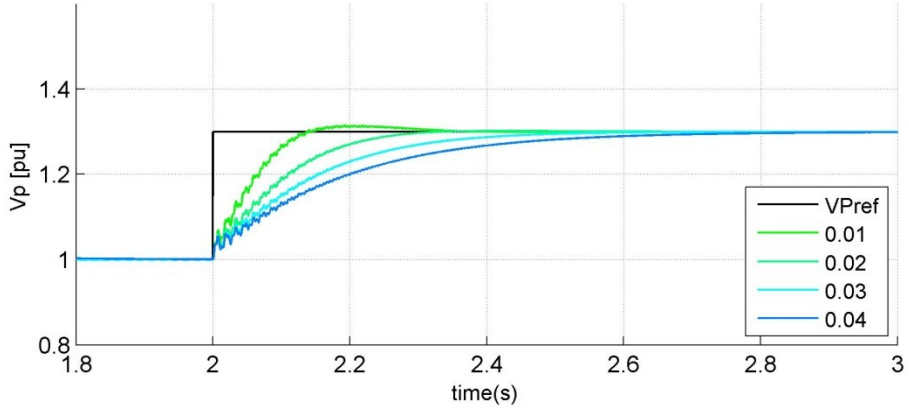

Figure 4-11 Voltage step response of system for various integral times, while the proportional gain is kept constant at 0.1

Table 4-4 PI-controller parameters for the control strategy 1

Description	$K_{p,v}$ **[pu]**	$T_{i,v}$ **[s]**
Platform voltage controller values	0.1	0.02

4.2.2 Control Strategy 2

Control strategy 2, as described in section 3.2.2, consists of an inner dq-current control loop, outer dq-platform voltage control loops and a third outer frequency control loop, providing the platform q-axis voltage control loop with its reference. A PLL is also implemented to track the platform frequency and phase angle.

Cascaded control requires the inner control loop to have a faster speed of response than the outer control loops. Therefore the inner current control loop should be tuned to achieve fast response, while the outer control loops should be tuned to achieve a stable system, with good regulation.

Conventional control tuning techniques starts to tune the inner control loop, moving outwards. This approach was also used for tuning of this cascaded controller. The inner current control loop of control system 2 cannot operate without the outer control loops, without applying fixed frequency to the system. The initial tuning of the inner current control loop was done when the frequency was fixed, and the results had to be adjusted for the full cascaded loop, since the real system operates with variable frequency. Thus the results from tuning of the inner current control loops with fixed frequency were not directly applicable for the real system and will not be shown here.

The full cascaded controller will be tested for step changes in the outer loop references; ω^* and V_p^*, and the resulting response of the dq-currents $i_{vsc,d}$ and $i_{vsc,q}$ and the q-axis voltage $V_{p,q}$ are plotted.

The parameters used in the PLL, determined using the Wiener method, are also provided.

4.2.2.1 Phase Lock Loop

The transfer function of the phase lock loop PI-controller is expressed as follows

$$PI_{PLL} = K_{p,pll}\frac{T_{i,pll}s + 1}{T_{i,pll}s} \tag{4-13}$$

An equivalent block diagram of the system can be developed based on the phase lock loop system shown in Figure 3-8. The relation between the phase angle error and the q-axis voltage can be expressed as follows

$$v_{p,q} = V_p \sin\delta \tag{4-14}$$

where V_p is the amplitude of the platform voltage and $\delta = \theta - \theta'$, where θ' is the platform voltage phase angle, and θ is the desired phase angle. Assuming δ is very small, the equation can be linearized and rewritten as follows [44]

$$v_{p,q} \cong V_p\delta \tag{4-15}$$

Based on these equations, the equivalent block diagram of the PLL can be seen in Figure 4-12 [45].

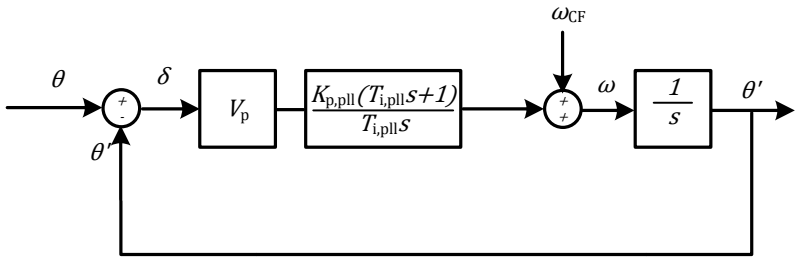

Figure 4-12 Equivalent block diagram of PLL

The general form of the second order transfer function is given as follows

$$H(s) = \frac{2\varsigma\omega_n s + \omega_n^2}{s^2 + 2\varsigma\omega_n s + \omega_n^2} \tag{4-16}$$

where ς is the damping ratio, and ω_n is the natural frequency.

The closed loop transfer function of the PLL can, based on this, be expressed on general form as follows

$$G_{cl} = \frac{V_p K_{p,pll} s + \frac{V_p K_{p,pll}}{T_{i,pll}}}{s^2 + V_p K_{p,pll} s + \frac{V_p K_{p,pll}}{T_{i,pll}}} \tag{4-17}$$

The relation between the PI-controller parameters and the damping ratio and the natural frequency can be used to tune the PLL. The square of the natural frequency is given as follows

$$\omega_n^2 = \frac{V_p K_{p,pll}}{T_{i,pll}} \tag{4-18}$$

The damping ratio is given as follows

$$\varsigma = \frac{V_p K_{p,pll}}{2\omega_n} \tag{4-19}$$

The method that is most frequently used to determine the PLL parameters is the Wiener method [44]. Determining the stochastic information required to use the Wiener method is a complex process, and is considered to be out of the scope of this thesis. Since the system frequency parameters resembles the parameters used in [44], the damping ratio and the natural frequency used there will be used to determine the PI-controller gain and time constants for the PLL implemented for control strategy 2. The damping ratio is therefore set to

$$\varsigma = \frac{1}{\sqrt{2}} \tag{4-20}$$

and the natural frequency is set to

$$\omega_n = 628\, rad/s \tag{4-21}$$

The voltage input of the system will be in per unit values. Therefore the voltage V_p is set to 1 pu for calculating the controller parameters. The PI-controller parameters calculated based on this are summarized in Table 4-5.

Table 4-5 PI-controller parameters for PLL

Description	$K_{p,pll}$ **[pu]**	$T_{i,pll}$ **[s]**
PLL, Wiener method based tuning	888	0.00225

4.2.2.2 The Cascade Controller

The parameters of the cascaded controllers are determined during the implementation of the cascade controller. The inner current control loop parameters are given in Table 4-6, while the outer voltage loop parameters are provided in Table 4-7. The frequency proportional gain is given in Table 4-8. These parameters are used for the cascaded controllers when the step response tests are done.

Table 4-6 Inner current control loop parameters

Description	$K_{p,iv2}$ **[pu]**	$T_{i,iv2}$ **[s]**
Inner current control loop	45	0.0004

Table 4-7 Outer voltage control loop parameters

Description	$K_{p,v2}$ **[pu]**	$T_{i,pv2}$ **[s]**
Outer voltage control loop	5	0.01
Outer voltage control loop	10	0.005

Table 4-8 Outer frequency control loop proportional gain

Description	$K_{p,\omega}$ **[pu]**
Frequency controller	-2.5

The platform system with control strategy 2, experiences a step change in the angular frequency reference from 1 pu to 1.1 pu, at time t = 0.2 s. The resulting responses of the system frequency and the dq-voltages can be seen in Figure 4-13.

The system angular frequency track its reference within 5 ms. The step change in the frequency makes the reference of the q-component voltage V_q, that is set to control the frequency, to change. The response of V_q has a small delay when it is tracking its reference, so that the drop of the reference can be seen to be larger than the actual drop in V_q. It can also be seen that the voltage d-component is not influenced by the step change in frequency. The voltage d-axis component is however influenced by the small oscillations about the reference frequency.

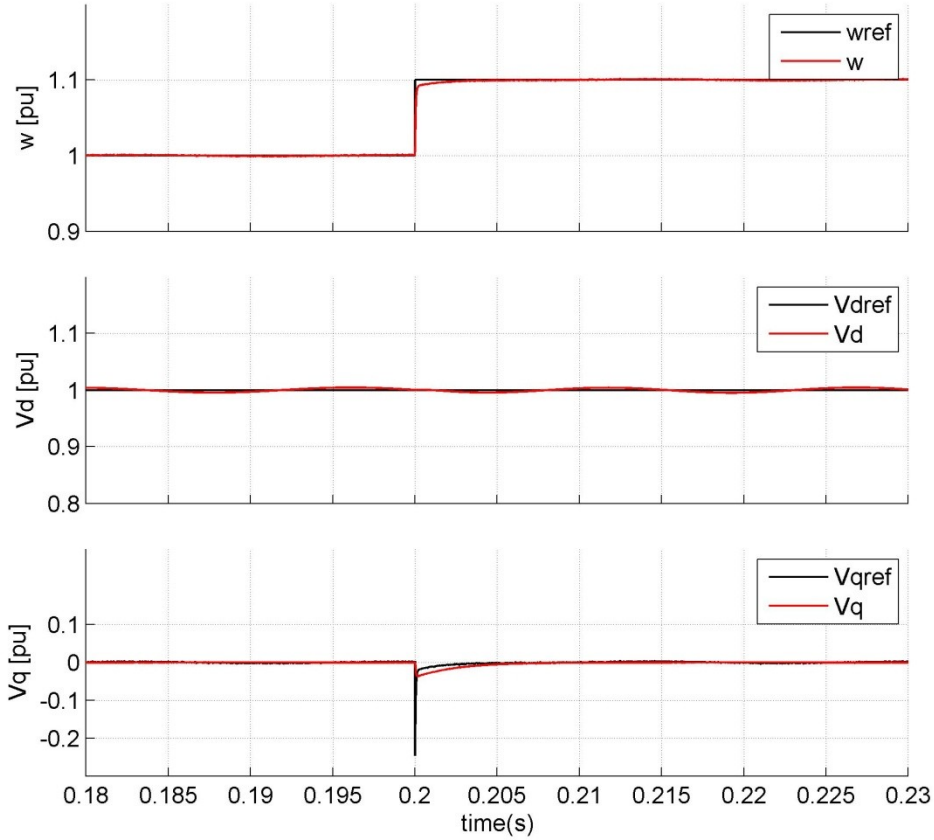

Figure 4-13 Platform voltage and frequency response for step change in angular frequency reference

The outer voltage loops provides the inner current control loops with its references, and the respective d-and q- current references are plotted with the measured d- and q-currents in Figure 4-14. The currents can be seen to track its reference perfectly, also during the step change in frequency.

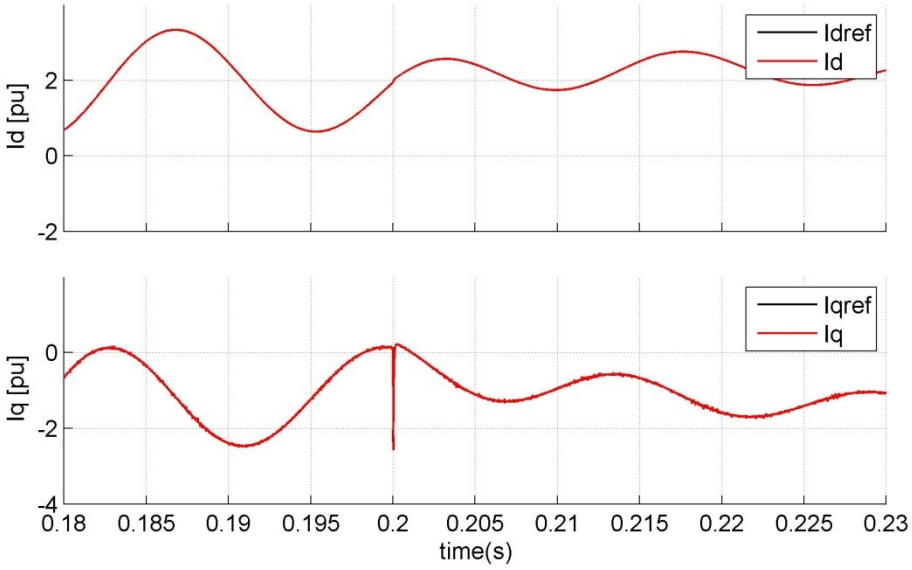

Figure 4-14 Current response for a step change in angular frequency

At time 0.4 s, the system experiences a step change in the d-axis voltage reference V_{pd}^{*} from 1 pu to 1.3 pu. The response of the measured d-axis voltage is plotted together with its reference in Figure 4-15. The d-axis voltage manages to track its reference in 14.9 ms, with a very small overshoot of 0.014 pu. The overshoot is assumed to be due to the small frequency variations in the system.

It can be seen that the voltage q-axis component is barely influenced by the step change in the d-axis voltage.

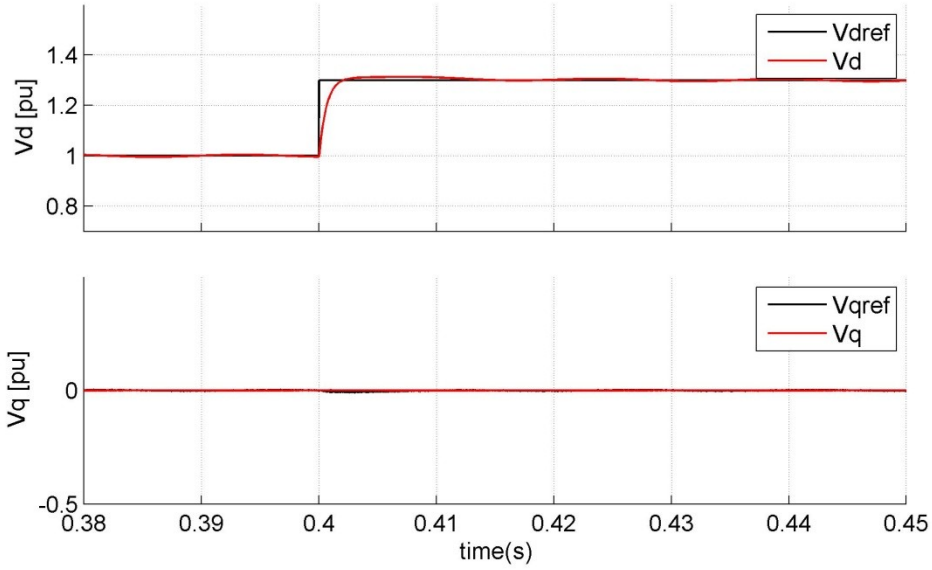

Figure 4-15 DQ-voltage response for a step change in the d-axis voltage reference

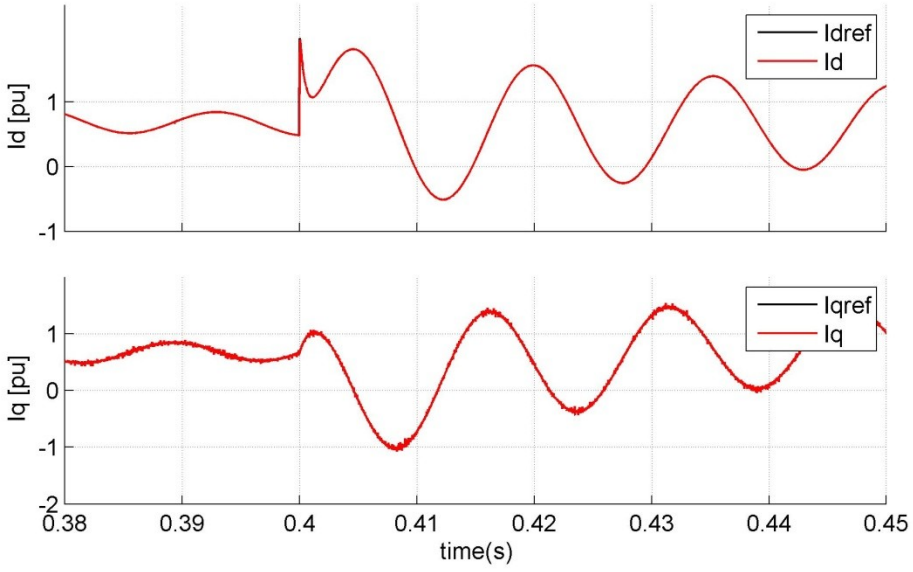

Figure 4-16 Current response for a step change in d-axis voltage

The step change in the voltage reference $V_{p,d}^{*}$ makes the reference of the d- and q-current components change. The response of the inner current control loops to the step change in the outer control loop d-axis voltage can be seen in Figure 4-16. The currents are perfectly tracking its reference, with only very small time delays. Both the d-and q-axis currents are influenced by the step change of $V_{p,d}$. This is expected due to the feed-forward terms with the measured q-and d-component voltages respectively.

Based on the step response tests for the cascaded controller it can be concluded that decoupled control of the d- and q-axis platform voltage has been successfully implemented. Changes in the d-axis voltage have very little influence on the q-axis voltage, and changes in the q-axis voltage have very little influence on the d-axis voltage.

Both the step change in the platform frequency reference and the platform voltage magnitude reference are tracked within 5 ms and 14.9 ms respectively.

5 Platform Voltage Estimation

For platform systems similar to the one studied in this thesis, measurements of voltages and currents on the platform will be available through a power management system (PMS). If the connection is lost and measurements from the platform are not longer available, the voltage control system should still be able to maintain the voltage at the platform at an acceptable level. For the platform system to be able to operate autonomously, the platform voltage has to be estimated for the control system to get feedback from the platform.

The measurements available for the estimator are the converter output voltage on shore and the current supplied to the platform system, measured at the beginning of the HVAC-cable on shore.

Close to exact parameters for real HVAC-cables can be available for a new cable installed, though there will still be variations in the cable parameters due to variations in temperature. As the lifetime of the cable passes, degrading of the cable performance will cause the cable dynamics to change [47]. A voltage estimator, measuring the current and voltage input to the cable, estimating the output voltage of the cable needs to have access to close to exact parameters to be able to provide an accurate estimate of the output voltage. A voltage estimator also needs to provide somehow accurate results for aberrations in cable parameters as well as for exact cable parameters available.

This chapter will provide the estimator mathematical model based on steady-state equations. The estimator will be simulated for load changes in chapter 6 when no platform voltage controller is implemented. The estimated platform voltage will then be applied as the input of control strategy 1, and used for testing for autonomous operation of the platform system, when exact cable system parameters are not available.

5.1 Equations Derived for Voltage Estimation

Sinusoidal currents and voltages can be represented by a phase vector also called a phasor. The phasor has an amplitude and angle, and it is time-invariant. Phasor representation can simplify calculations considerably, and is therefore used for this platform voltage estimation. They are only valid for sinusoidal voltages and currents in steady-state, and will therefore not be accurate during transients and changes in the system.

An HVAC-cable can be modeled by one or several pi-equivalents, as discussed in section 2.4. The cable is, as defined in section 2.4.3, as a single pi-equivalent

circuit. The system model can be seen in Figure 5-1, and the equations are developed based on this model.

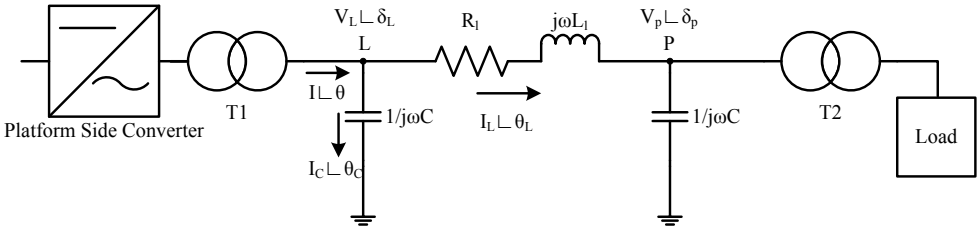

Figure 5-1, Equivalent circuit used for platform voltage estimation, with ideal transformers

To be able to estimate the platform voltage, the current flowing on the line, through the inductor and the resistor out from point L, must be known. This current can be found as follows

$$I_L \angle \theta_L = I \angle \theta - I_C \angle \theta_C \tag{5-1}$$

Where $I \angle \theta$ is the measured current flowing into point L, $I_C \angle \theta_C$ is the current absorbed by the capacitor and $I_L \angle \theta_L$ is the current running through the inductor and resistor. To be able to calculate $I_L \angle \theta_L$, $I_C \angle \theta_C$ must be found.

$$I_C \angle \theta_C = \frac{V_L \angle \delta_L}{-j\frac{1}{\omega C}} = (V_L * \omega C) \angle (\delta_L + 90^o) \tag{5-2}$$

This can be divided into a real and an imaginary part. Euler's law gives

$$I_C \angle \theta_C = V_L * \omega C * \cos(\delta_L + 90^0) + j * V_L * \omega C * \sin(\delta_L + 90^o) \tag{5-3}$$

Then $I_L \angle \theta_L$ can be written as

$$I_L \angle \theta_L = (I * cos\theta - V_L * \omega C * \cos(\delta_L + 90^0)) + j * (I * sin\theta - V_L * \omega C * \sin(\delta_L + 90^o)) \tag{5-4}$$

This can also be expressed by the phasor magnitude and angle, and is founds as follows

$$I_L^2 = (I * cos\theta - V_L * \omega C * \cos(\delta_L + 90))^2 + (I * sin\theta - V_L * \omega C * \sin(\delta_L + 90^o))^2 \quad (5\text{-}5)$$

The phase angle is given as follows

$$\theta_L = \arctan\left(\frac{I * cos\theta - V_L * \omega C * cos(\delta_L + 90)}{I * sin\theta - V_L * \omega C * sin(\delta_L + 90^o)}\right) \quad (5\text{-}6)$$

When $I_L \angle \theta_L$ is found, the platform voltage, that is the voltage in point P, can be calculated as follows

$$V_P \angle \delta_P = V_L \angle \delta_L - \omega L * I_L \angle (\theta_L + 90^o) - R * I_L \angle \theta_L \quad (5\text{-}7)$$

This can be rewritten as

$$V_P \angle \delta_P = (V_L cos\delta_L + \omega L * I_L * \cos(\theta_L + 90^o) - R * I_L * cos\theta_L) + j * (V_L sin\delta_L - \omega L * I_L * \sin(\theta_L + 90^o) - R * I_L * \sin\theta_L) \quad (5\text{-}8)$$

The platform voltage can also be expressed by the magnitude

$$V_P^2 = (V_L cos\delta_L + \omega L * I_L * \cos(\theta_L + 90^o) - R * I_L * cos\theta_L)^2 + (V_L sin\delta_L - \omega L * I_L * \sin(\theta_L + 90^o) - R * I_L * \sin\theta_L)^2 \quad (5\text{-}9)$$

and angle

$$\delta_P = \arctan\left(\frac{V_L cos\delta_L + \omega L * I_L * cos(\theta_L + 90^o) - R * I_L * cos\theta_L}{V_L sin\delta_L - \omega L * I_L * sin(\theta_L + 90^o) - R * I_L * sin\theta_L}\right) \quad (5\text{-}10)$$

The platform voltage equations do now only consist of known quantities, and the steady-state platform voltage can be estimated.
The equations provided here forms the basis for implementation of voltage estimation in MATLAB® Simulink™.

6 System Simulations

This chapter will present the simulations results for the systems. The simulations will be described in section 6.1. Section 6.2 will present the results from testing the voltage estimator; section 6.3 will present the results from testing control strategy 1for the different system configurations; section 6.4 presents the results from testing control strategy 2. These results will be further discussed in chapter 7

6.1 Simulation Description

6.1.1 Platform Voltage Estimator

The purpose of the platform voltage estimator simulations is to determine the accuracy of the platform voltage estimator during and after large changes in platform load.

The platform voltage estimator will be tested for the HVAC-cable model used for developing the equations given in section 5.1. Exact cable parameters, defined in Table 2-3, are used for the voltage estimator. The transformers are non-ideal, and the estimator uses measurements of voltage and currents onshore on the secondary side of the shore-based transformer. The voltage estimated is equivalent to the voltage of the primary-side platform transformer. This is done to eliminate the effect of the voltage drop over the non-ideal transformer in the initial estimator tests.

The system is initially operating in steady-state with a 4 MW passive load. Three load tests will be applied for the system: loss-of all-load, increase-of-passive-load and induction-motor-starting. The load tests are summarized in Table 6-1, but the values in first row of the table are not applicable for testing of this system. No platform voltage control system is implemented for the platform system, so the changes in voltage on the platform will be visible for changes in platform load.

6.1.2 Control Strategy 1 and 2

The main purpose of these simulations is to study the performance of control strategy 1 and 2, when regulating the platform voltage and frequency for worst-case changes in load.

The performance of the controller voltage and frequency regulation will be evaluated based on the requirements defined for the platform system, based on the IEC 61892 standard for fixed and floating offshore installations.

The initial load of all the systems to be tested is the 23 MVA accumulated induction motor model, operating in steady-state on the platform with a power factor of 0.8, and a 2 MW passive load. All the system configurations will be tested

for 3 different types of worst-case load changes: loss-of-all-load, induction-motor-start and increase-of-passive-load. The load tests are summarized in Table 6-1.

It should be noted that the voltage controlled to 1 pu by control strategy 1 is the line-to-neutral peak voltage, see the per unit system defined in section 2.6. When the estimated platform voltage is compared to the measured platform voltage in this section, the RMS-value of the line-to-neutral voltage will be plotted. This voltage value will be $\frac{1}{\sqrt{2}}$ pu when the line-to-neutral peak voltage is 1 pu.

Table 6-1 Platform load tests summarized

Load Test No.	Title	Description	Value
1	Loss of all load	At time t, all platform load is lost	-23 MVA, -2MW
2	Increase of passive load	At time t, there is an increase of passive platform load of 2 MVA	2 MVA, Pf = 0.9
3	Induction motor start	At time t, a 8 MVA induction machine is directly started on the platform	8 MVA

6.2 Platform Voltage Estimator

6.2.1 Loss of all load

The system is initially operating in steady-state with a 4 MW passive load. At time t = 0.5 s, all load is lost. The measured voltage plotted versus the estimated platform voltage can be seen in Figure 6-1. The results show that the estimated voltage is very accurate for steady-state operation. During the fast transients from the loss-of-all-load, the estimation error is larger.

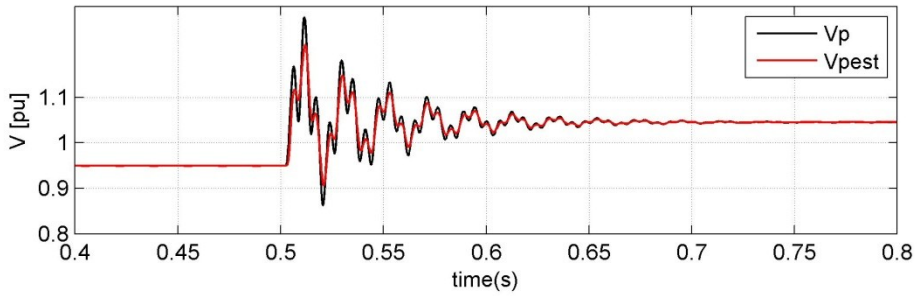

Figure 6-1 Measured platform voltage versus estimated platform voltage, for loss-of-all-load

6.2.2 Increase of passive load

The system is initially operating in steady-state with the 4 MW passive load, at time t = 0.5 s, there is an increase in passive load of 2 MVA, with a power factor of 0.9. The resulting measured platform voltage is plotted versus the estimated platform voltage in Figure 6-2. The estimated voltage can be seen to track the measured voltage very accurately, both for steady-state operation and for system transients.

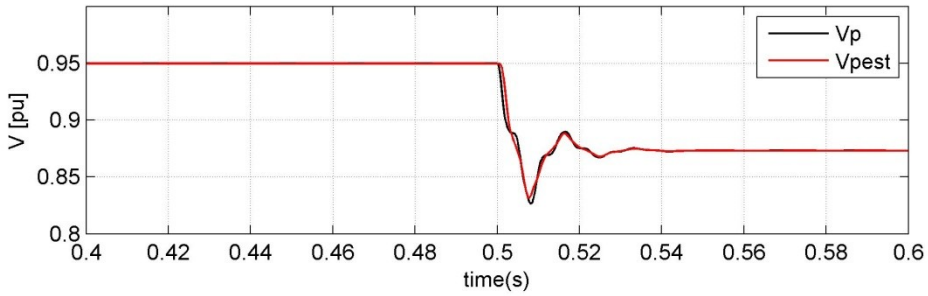

Figure 6-2 Measured platform voltage versus estimated platform voltage, for increase-of-passive-load

6.2.3 Induction motor start

The system is initially operating in steady-state with a 4 MW passive load, at time t = 0.5 s, an 8 MVA induction motor is directly started on the platform. The resulting measured platform voltage plotted versus the estimated platform voltage for the induction motor start is shown in Figure 6-3. The voltage estimator is tracking the platform voltage, for both transients and steady-state operation. When studying the waveforms very closely it can be seen that there are small errors in the estimated platform voltage oscillations. This is due to the mathematical being based on steady-state equations.

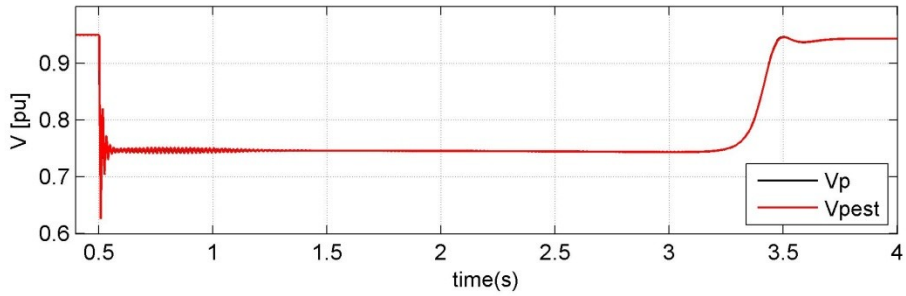

Figure 6-3 Measured platform voltage versus estimated platform voltage, for 8 MVA induction-motor-starting

6.3 Control Strategy 1

The platform system is first tested separately, when applied a constant DC-link voltage, with control strategy 1 controlling the platform voltage magnitude, while the frequency is fixed. Three load change tests, defined in Table 6-1, are run for both normal operation, when measured platform voltage is available, and for autonomous operation, when the estimated platform voltage is used as input to the controller. Control strategy 1 is also tested when the grid-side VSC is connected to the platform-side VSC, through the DC-link. When the system is connected in full B2B-configuration the DC-link voltage variations will influence the platform-side system, and hence the platform-side controller.

The results from the load change tests are evaluated based on the system requirements defined in Table 1-1, based on the IEC 61892 standard. The only requirements applicable for the systems tested with control strategy 1 are the ones for steady-state and transient platform voltage, and stable operation. These are summarized in Table 6-2.

It should be noted that the voltage controlled to 1 pu by control strategy 1 is the line-to-neutral peak voltage, see the per unit system defined in section 2.6.

All measurements from the plots are provided in tables in Appendix C.

Table 6-2 Control strategy 1, requirements for operation of platform system

Req. No.	Requirement Title	Value
1	Steady-state voltage	$+6\%, -10\% * V_n$
	Transient voltage	$\pm 20\% * V_n$ $t_{rec} < 1.5\ s$
3	Stable operation	Not Applicable

6.3.1 Platform System

6.3.1.1 Loss of all Load

The platform system is initially operating in steady-state, with the accumulated 23 MVA induction machine and a 2 MW passive load. At time t = 2 s, the platform-system experiences loss-of-all-load.

The platform voltage magnitude response to the loss of all loads can be seen in Figure 6-4. The moment all load is lost there is a large voltage transient that peaks at 1.62 pu. This is due to the sudden change of current through the transformer inductance, which would give a large voltage spike on the platform, as can be seen from the figure. The voltage controller is not fast enough to limit the voltage magnitude of this transient. The voltage controller manages to regulate the platform voltage back to its rated value within 0.45 s.

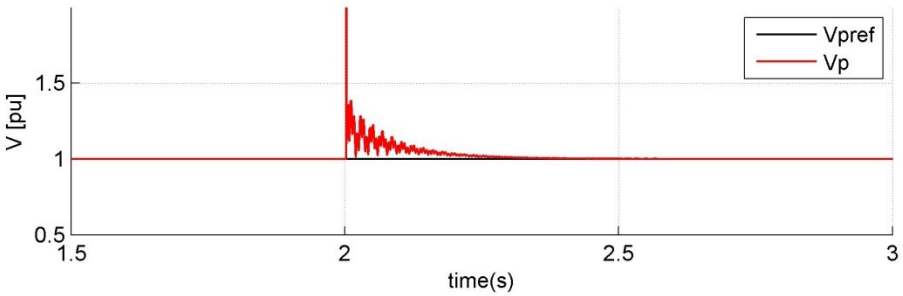

Figure 6-4 Platform voltage transient for sudden loss-of-all-load

Figure 6-5 shows the system response for loss-of-all-load, when the estimated voltage is applied to the system, and the operation is autonomous.

Compared to the platform system response during normal operation, shown above, the voltage transient peak is considerably lower for autonomous operation. It is still right above the allowable limit for voltage transients on the platform, that is 20.9 % over the platform rated voltage. The estimated voltage tracks the voltage reference within 0.6 seconds.

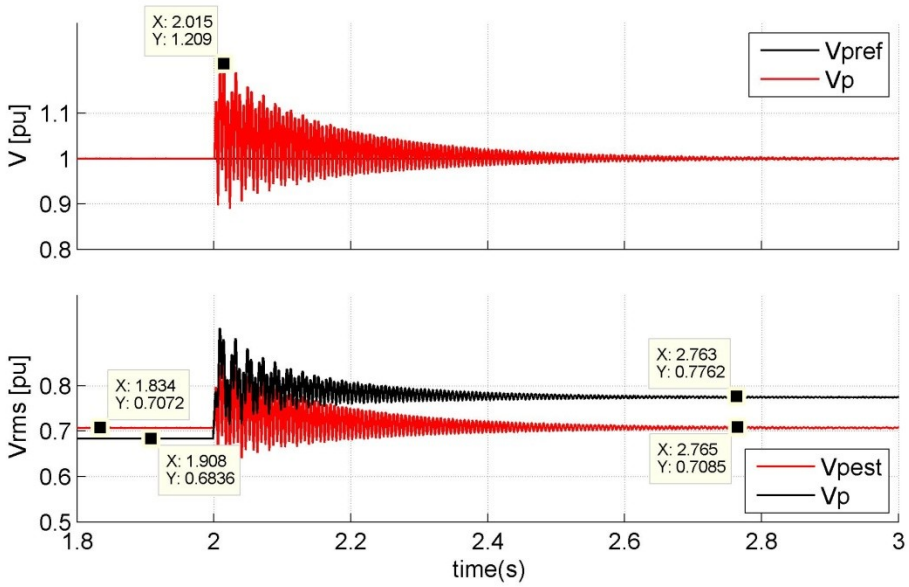

Figure 6-5 Platform voltage transient for sudden loss-of all-load during autonomous operation

The estimated voltage is plotted together with the actual platform voltage in the bottom graph of Figure 6-5. It can be seen that the initial estimated voltage is 0.0236 pu larger than the actual platform voltage. This is due to the voltage drop over the non-ideal transformer on the platform. This voltage difference is 3.3 % smaller than the desired line-to-neutral voltage of $\frac{1}{\sqrt{2}}$ pu.

The estimated voltage is regulated back to its initial value 0.6 seconds after all load is lost. The actual platform voltage increases to 0.0677 pu above the rated platform voltage, which is 9.4 % larger than the rated platform voltage, and is not acceptable as a steady-state voltage error for the system.

The estimator is estimating the platform transformer primary-side voltage, and does not include the voltage drop or increase across the transformer equivalent inductance and resistance. When all load is lost, the current flowing through the transformer inductance and resistance is changing. At that point no active power is drawn by the platform, so the active current goes to zero. The reactive power consumption on the platform also decreases, but the reactive current supplied by the platform-side pi-equivalent capacitance does not change, which makes the platform voltage to increase, while the primary-side voltage of the transformer is regulated back to its rated value of $\frac{1}{\sqrt{2}}$ pu.

6.3.1.2 *Increase of Passive Load*

The system is initially operating in steady-state with the large accumulated induction motor of 23 MVA and a passive load of 2 MW. At time t = 2 s, there is an increase in the platform load of 2 MVA, with a power factor of 0.9.

It can be seen from Figure 6-6 that the platform voltage has a dip of 1.4 % of the rated platform voltage during the increase of load. The platform voltage recovers within 0.4 seconds.

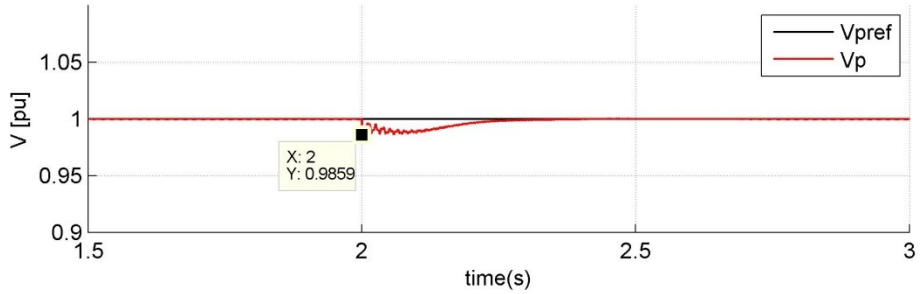

Figure 6-6 Platform system transient for increase of passive load of 2 MVA, with a power factor of 0.8

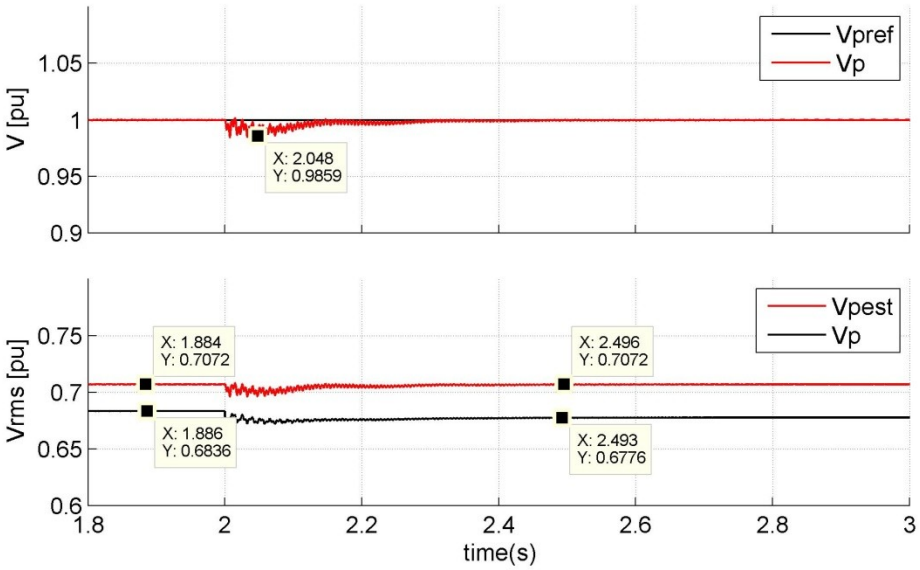

Figure 6-7 Platform voltage transient for increase-of-passive-load during autonomous operation

The increase of load test is applied to the system in autonomous operation, and the resulting system response is plotted in Figure 6-7. The estimated platform voltage transient during increase of passive load has the same peak and recovery time as for the system in normal operation. The estimation error of the platform voltage is still 3.3 % before the load change. The steady-state estimation error after the load change is 4.2 % below the rated platform voltage. This is acceptable according to the system requirements and the platform voltage controller and estimator provides acceptable operation for autonomous operation during and after an increase in passive platform load. The change in the actual platform after the increase of load is 0.8 % of the initial actual platform voltage value.

6.3.1.3 Induction Motor Starting

The platform system is operating in steady-state with the accumulated induction motor model of 23 MVA and a passive load of 2 MW on the platform. At time t = 2 se an 8 MVA induction motor is directly started on the platform. The resulting platform voltage magnitude and the reactive power consumed at the platform can be seen in Figure 6-8.

When the induction machine is starting it draws a large amount of reactive current and hence reactive power. This increased reactive power consumption makes the platform voltage drop to 0.7621 pu, which is 23.8 % lower than the rated platform voltage. The voltage controller manages to recover the platform voltage within 0.62 s.

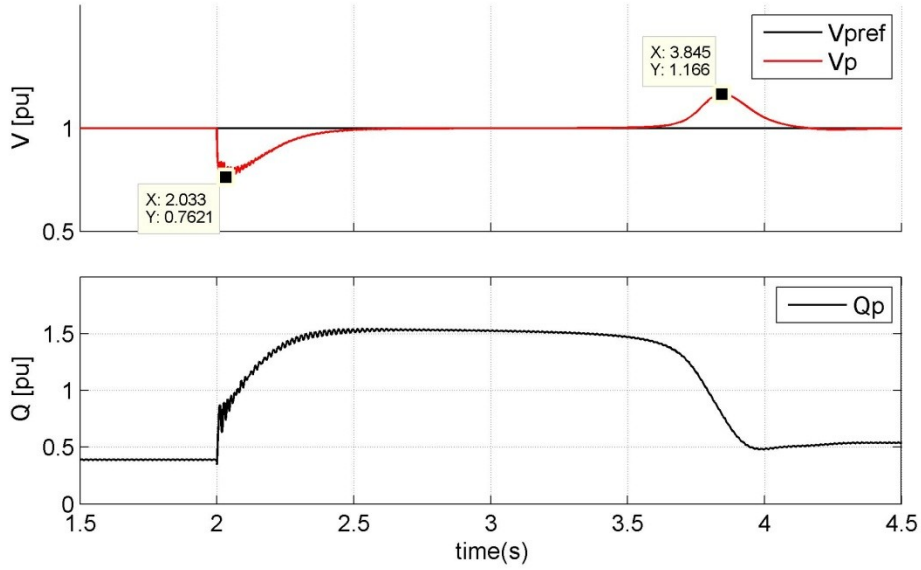

Figure 6-8 Platform system transient for 8 MVA direct induction motor start

When the induction motor is reaching the low slip region of operation, which is when the rotor speed is approaching the synchronous speed, the reactive power consumption of the induction machine decreases. This can be seen in the figure. When the reactive power consumption on the platform decreases, the voltage increases to 1.166 pu, which is 16.6 % larger than the rated platform voltage. The voltage controller recovers the platform voltage within 0.967 s, and the second induction motor starting platform voltage transient has an acceptable magnitude and recovery time.

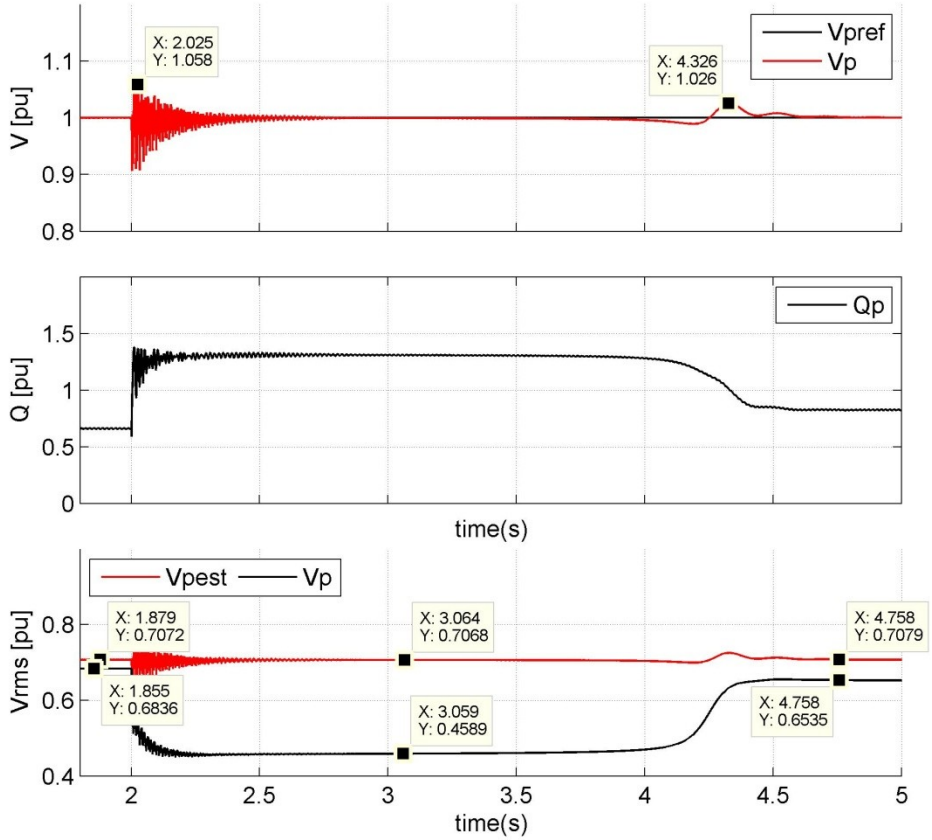

Figure 6-9 Platform voltage transient for induction motor start during autonomous operation

The results from the induction motor start for the platform-system operating autonomously can be seen in Figure 6-9. The platform voltage transient has considerably more oscillations in autonomous operation than for the normal operation, and the transient voltage peaks are approximately ± 6 % of the rated platform voltage during the induction motor start. The platform voltage recovers in approximately 0.62 s.

When the induction motor is reaching the low slip region, it draws less reactive power. This makes the voltage peak at 1.026 pu, 2.6 % larger than the rated voltage. The voltage recovers within 1.029 s.

The actual platform voltage is plotted in the bottom graph of Figure 6-9. The initial estimation error is 3.3 %. The induction motor start makes the load active and reactive current increase, which makes the voltage drop over the transformer inductance and resistance larger, and hence the voltage estimation error larger. The estimation error during the induction motor start is -35 % of the rated voltage. This large estimation error makes the actual platform voltage operate at 0.4589 pu for 2 s

during the motor start. When the induction motor is reaching low slip speed and the reactive power consumed decreases, the voltage estimation error decreases to -7.69 % of the rated platform voltage. The platform voltage is not within the limits defined by the system requirements for acceptable operation and control when the estimated platform voltage is applied.

6.3.2 Full B2B-VSC System

The grid-side system is connected with the platform side-system, and applied control strategy 1. The grid-side system is controlling the DC-link voltage and the reactive power drawn from the grid, while the platform-side system is controlling the platform voltage, while keeping the frequency fixed.

6.3.2.1 Loss of all Load

The full B2B-VSC system is operating in steady-state with control strategy 1. At time t = 2 s, all platform load is lost. The resulting platform voltage, DC-link voltage and reactive power drawn from the grid is shown in Figure 6-10.

The platform voltage has a peak of 1.424 pu, which is 42.2 % larger than the rated platform voltage, and hence not an acceptable voltage transient for the platform. The voltage recovers within 0.412 seconds.

The DC-link voltage can be seen to have a transient of 1.797 pu, which is 8 % larger than the rated DC-link voltage. The change in power drawn from the grid-side to the platform-side system makes the DC-current flow drop, which yields a DC-link transient voltage increase.

There are not defined any requirements for the DC-link voltage directly. It is apparent that fast tracking of DC-link voltage is essential for ensuring fast control of the platform voltage.

The reactive power drawn from the grid is not visibly influenced by the sudden loss-of-all-load on the platform.

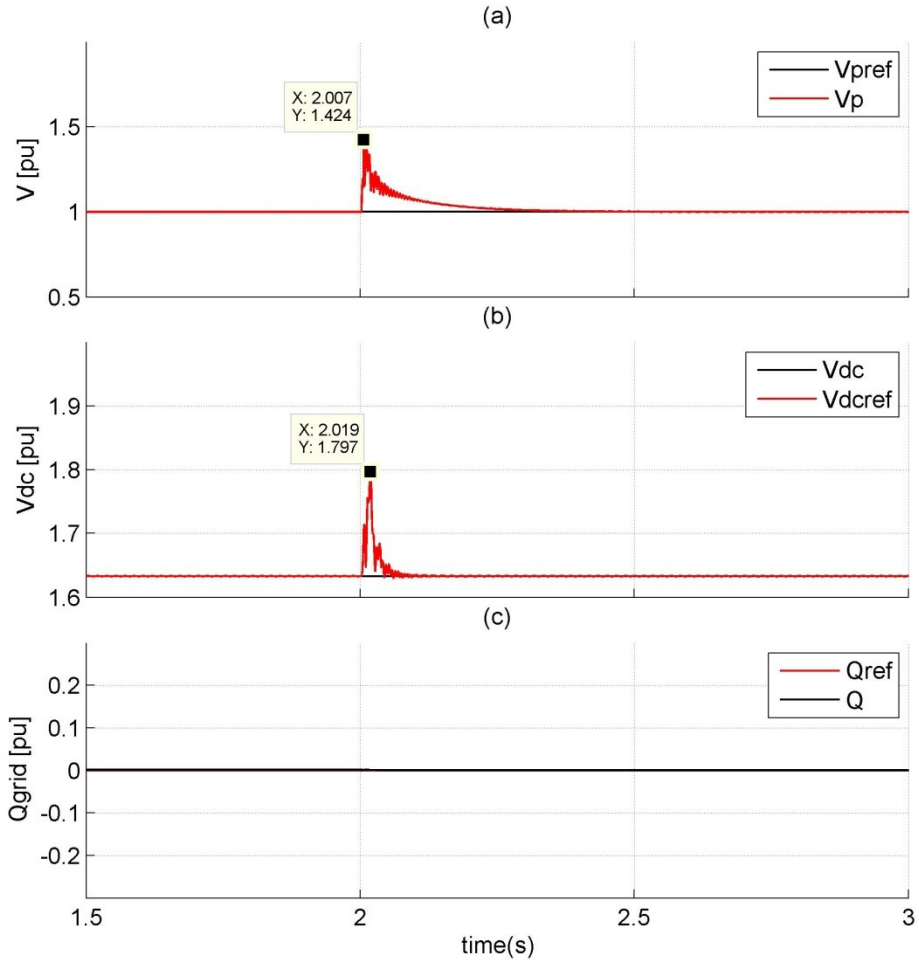

Figure 6-10 Full B2B-VSC experiences sudden loss-of-all-load

6.3.2.2 Increase of Passive Load

The full B2B-VSC system is operating in steady-state with the 23 MVA accumulated induction machine and a 2 MW load on the platform. At time t = 2 s, there is an increase of passive load of 2 MVA, with a power factor of 0.9. The platform voltage response to the load change can be seen in Figure 6-11, together with the load change influence in DC-link voltage and reactive power drawn from the grid.

The platform voltage can be seen to have a voltage drop of 3.4 % of the rated platform voltage. The voltage recovers within 0.39 seconds. The voltage transient is acceptable based on the requirements set for the system.

The figure also shows that the increase of platform load makes the DC-voltage drop, due to the increase of power consumed by the platform system, and hence an

increase of DC-link current drawn on the platform side. The DC-link voltage drop is 2.3 % of the rated DC-link voltage, and recovers within 0.228 seconds.

The reactive power consumed from the grid is not influenced by the sudden increase of passive load on the platform.

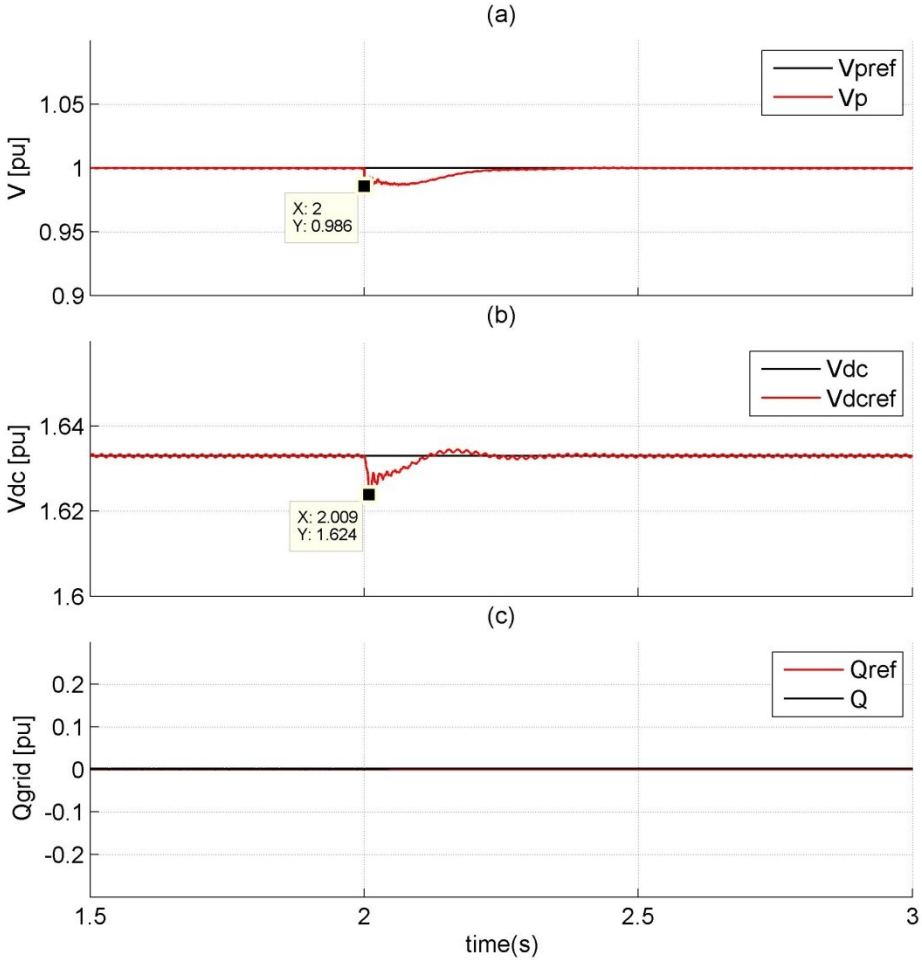

Figure 6-11 Full B2B-VSC system experiences increase of 2 MVA load with a power factor of 0.8

6.3.2.3 Induction Motor Starting

The full B2B-VSC system is operating in steady-state with the 23 MVA accumulated induction machine and a 2 MW load on the platform. At time t = 2 s, an induction machine of 8 MVA is directly started on the platform.

The resulting platform voltage, the platform reactive power consumed on the platform, DC-link voltage and the reactive power consumed by the grid can be seen in Figure 6-12.

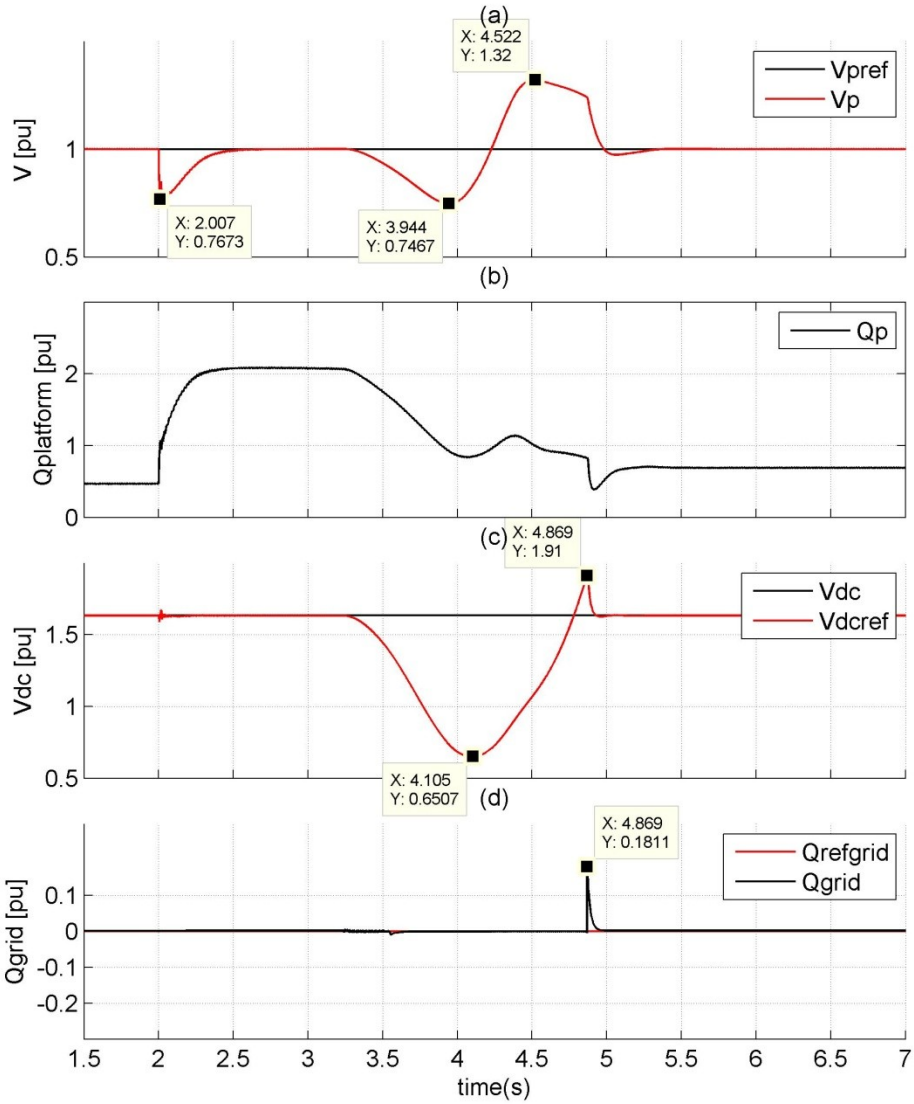

Figure 6-12 Full B2B-VSC system experiences DOL starting of an 8 MVA induction machine on the platform

When the induction motor starts the reactive power consumed on the platform increases, which makes the platform voltage drop. The platform voltage transient is 23.3 % lower than the rated platform voltage, which is below the lower allowable limit for a voltage transient, and hence not acceptable for the system. The platform voltage controller regulates the voltage within 0.686 seconds. At time 3.5 seconds there is another large voltage sag on the platform, right before the induction motor is about to reach the low slip operation region. The DC-link voltage has a large drop at this time, of about 60 % of the rated DC-link voltage.

The DC-link voltage is controlled by controlling the d-axis current in the grid-side system. Maintaining the DC-link voltage at its reference for the motor start requires a certain increase of d-axis current, and hence a lower voltage at the grid-side converter terminals. The limiter for the DC-voltage controller output d-axis current reference is set to 1 pu, and when this current value is reached, the d-axis current can no longer follow its reference. This limit is reached at time t = 3.5 s, and there is a large drop in DC-link voltage. The drop in DC-link voltage makes the platform-side VSC output voltage drop, which again makes the platform voltage drop 25 % of its rated value, to 0.7467 pu. As long as the d-axis current cannot track its reference, the DC-link voltage is not following its reference. At time t = 4.8 s, the d-axis grid current reference is no longer at its maximum value 1 pu, and the DC-link voltage and platform voltage is regulated to its reference.

Though the grid-side d-axis current is reaching its limit and the DC-link voltage and the platform voltage drops, the 8 MVA induction machine manages to start on the platform. The transients due to the induction motor starting, when the DC-link voltage cannot track its reference are not acceptable for the system.

The motor start for the full B2B-system shows gives a very clear picture of the relation between the converters in the configuration. The limitations on the grid currents set very specific limitations for the DC-link voltage regulation and hence the platform voltage regulation abilities.

6.4 Control Strategy 2

The platform system is tested separately, when applied a constant DC-link voltage, with control strategy 2 controlling the platform voltage magnitude and frequency. The system is tested for three worst-case load changes: loss-of-all-loads, increase-of-passive-load, and large induction-motor-start. The load tests are summarized in Table 6-1.

Control strategy 2 is evaluated based on the system requirements defined in Table 1-1, based on the IEC 61892 standard. Since it controls both the platform voltage magnitude and frequency, all the system requirements defined are applicable for the system tested in this section. The requirements are summarized in Table 6-2.

It should be noted, when studying the results provided in this section, that the reactive line current component, that is the q-axis current component, is defined as consuming reactive power when it is positive and it is defined as supplying reactive power when it is negative. The reactive power shown is defined as consuming reactive power when it is positive and supplying reactive power when it is negative.

The voltage controlled to 1 pu, by control strategy 2, is the line-to-neutral peak voltage, as defined in section 2.6.

Table 6-3 Control strategy 2, requirements for acceptable operation of platform system

Req. No.	Requirement Title	Value
1	Steady-state voltage	$+6\%, -10\% * V_n$
	Transient voltage	$\pm 20\% * V_n$ $t_{rec} < 1.5\ s$
2	Steady-state frequency	$\pm 5\% * f_n$
	Transient frequency	$\pm\ 10\% * f_n$ $t_{rec} < 5\ s$
3	Stable operation	Not Applicable

6.4.1 Loss of all Load

The platform system is operating in steady-state with a 23 MVA induction motor with a power factor of 0.8 and a passive load of 2 MW. At time t = 0.4 s, all platform load is lost. The resulting platform voltage magnitude and frequency can be seen in Figure 6-13. There are no visible transients in the platform voltage magnitude or frequency for loss-of-all-load. There are however some small periodic oscillations in the platform voltage magnitude, due to the small periodic oscillations in the system angular frequency. This is not due to the loss of load.

The changes in the line currents can be seen in Figure 6-14, and are very apparent at time 0.4 s when all load is lost. The feed-forward terms in the controller, described in section 3.2.2.3, compensates for the changes in load current, and the coupling of the platform d- and q-voltage components over the capacitor.

The active current component goes to zero when all load is lost since the platform is no longer consuming active power. The reactive current component increases, that is becomes more inductive, and absorbs the residual reactive power produced on the platform. This way the platform voltage is maintained at its reference value.

The reactive current can be seen to have considerable oscillations compared to the active current.

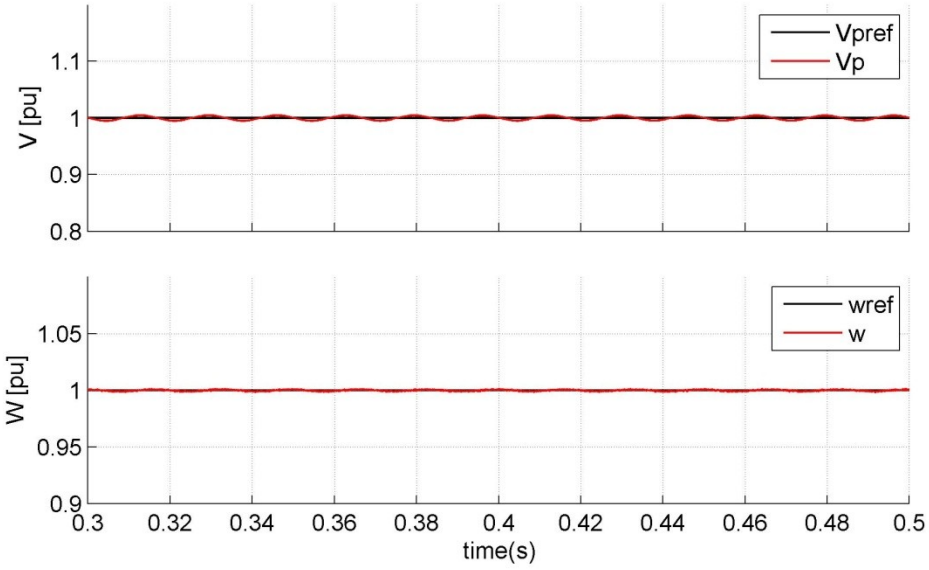

Figure 6-13 Platform voltage and frequency for sudden loss-of-all-load

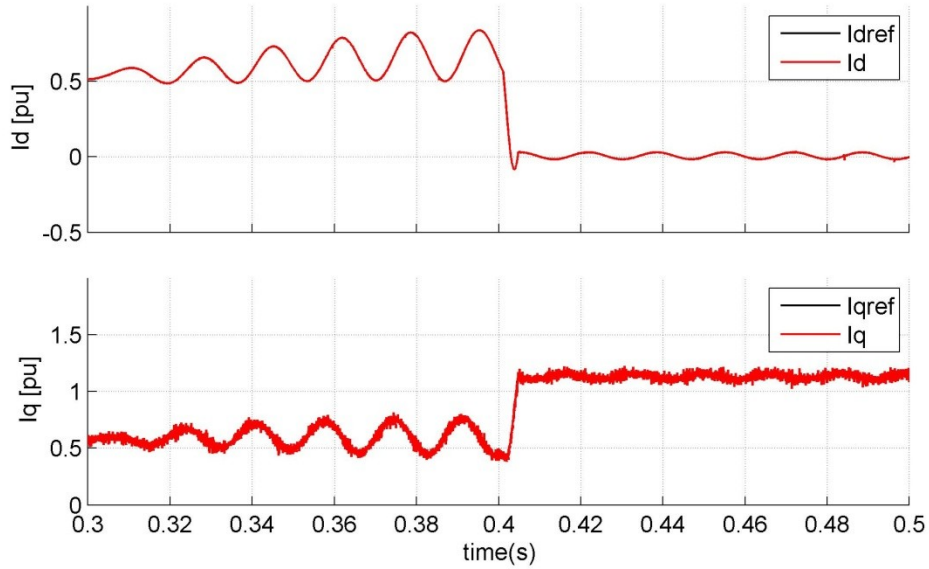

Figure 6-14 Controlled line currents for sudden loss-of-all-load

6.4.2 Increase of Passive Load

The platform system, controlled by control strategy 2, is operating in steady-state with a 23 MVA accumulated induction machine and a 2 MW passive load. At time t = 0.4 s, a 2 MVA passive load, with a power factor of 0.9, is connected to the platform.

The resulting platform voltage and frequency can be seen in Figure 6-15. There are no visible changes in platform voltage or frequency for the increase of the platform load.

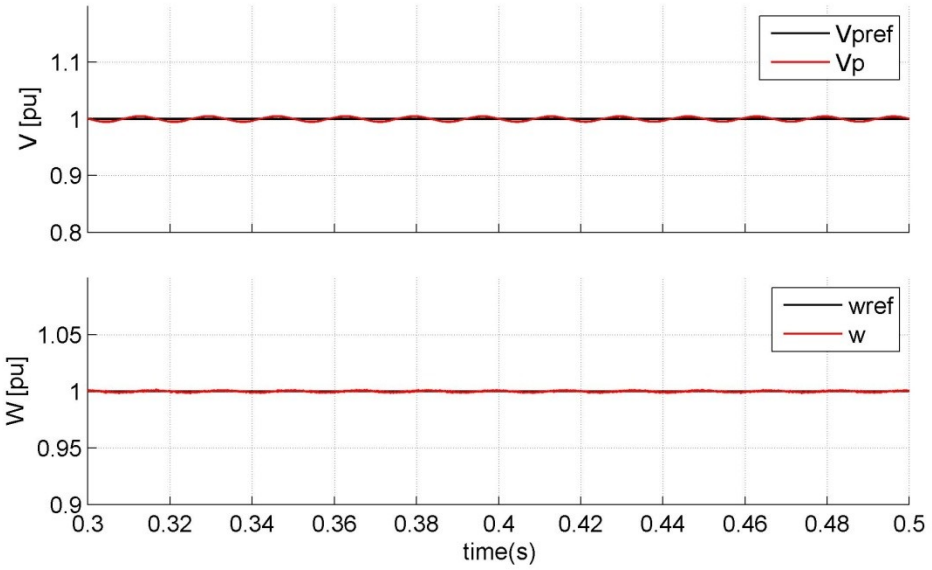

Figure 6-15 Platform voltage and frequency for increase of passive load of 2 MVA, with a power factor of 0.9

The controlled line currents are shown in Figure 6-16, where the passive load increase can be seen to visible influence the active current, while the influence in the reactive currents are small.

Both the active and reactive current components are oscillating, and the reactive current has noise in its signal.

The frequency oscillations on the platform are very small, and both transient and steady-state operation is acceptable according to the system requirements.

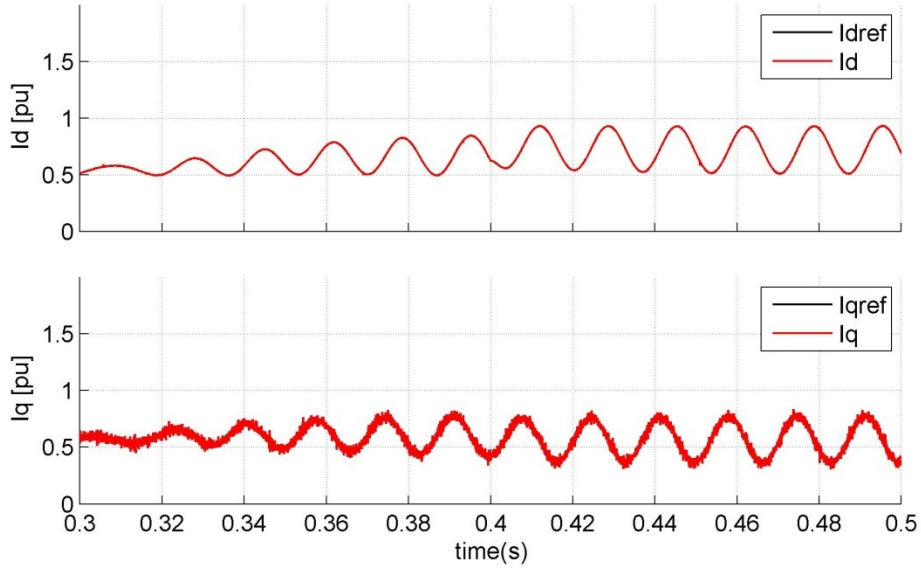

Figure 6-16 Controlled line currents for increase of passive load at time t = 0.4 s

6.4.3 Induction Motor Starting

The platform system is operating in steady-state with a 23 MVA accumulated induction motor with a power factor of 0.8 pu and a 2 MW passive load. At time 0.4 s, an 8 MVA induction motor is directly started on the platform.

The resulting platform voltage magnitude, reactive power consumption and angular frequency can be seen in Figure 6-17. There are some very small oscillations in the platform voltage magnitude when the large induction motor is starting on the platform, but they are damped after one second.

The reactive power consumption on the platform has the characteristic motor starting shape, and there are large oscillations in the reactive power consumed.

The angular frequency is not influenced by the induction motor start.

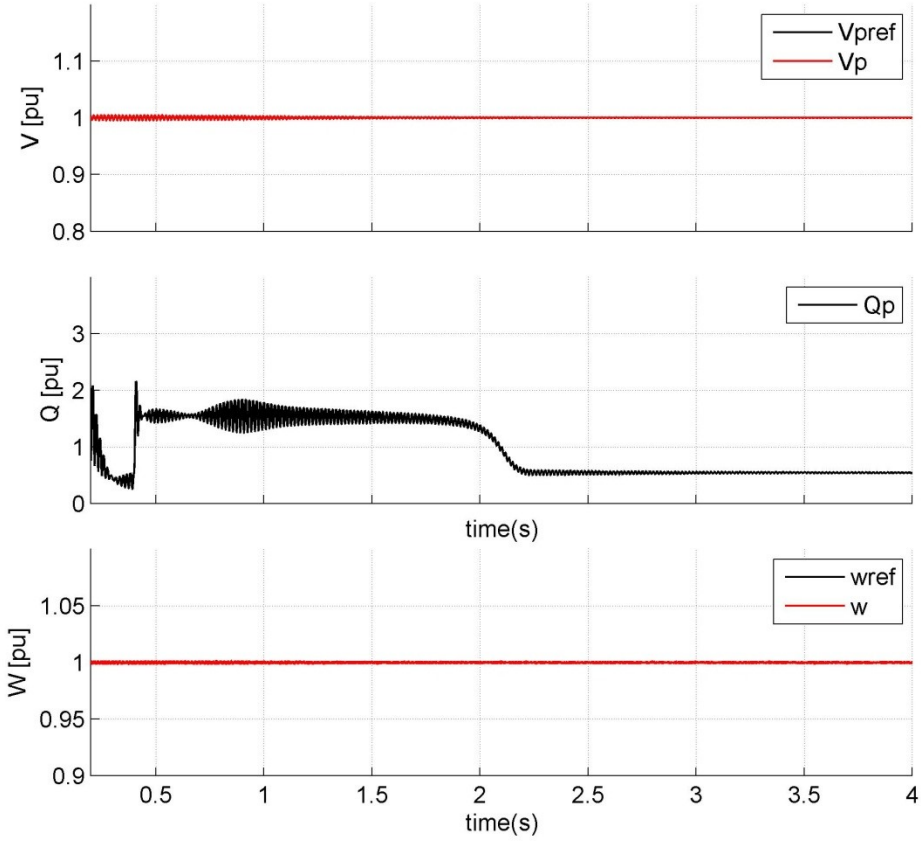

Figure 6-17 Platform voltage magnitude, reactive power and frequency for 8 MVA induction-motor-starting

Figure 6-18 shows that there are considerable amounts of oscillations in the active and reactive line currents. The oscillations in the active currents are damped after the induction motor start, while the reactive current still has a considerable amount of oscillations after the induction motor start.

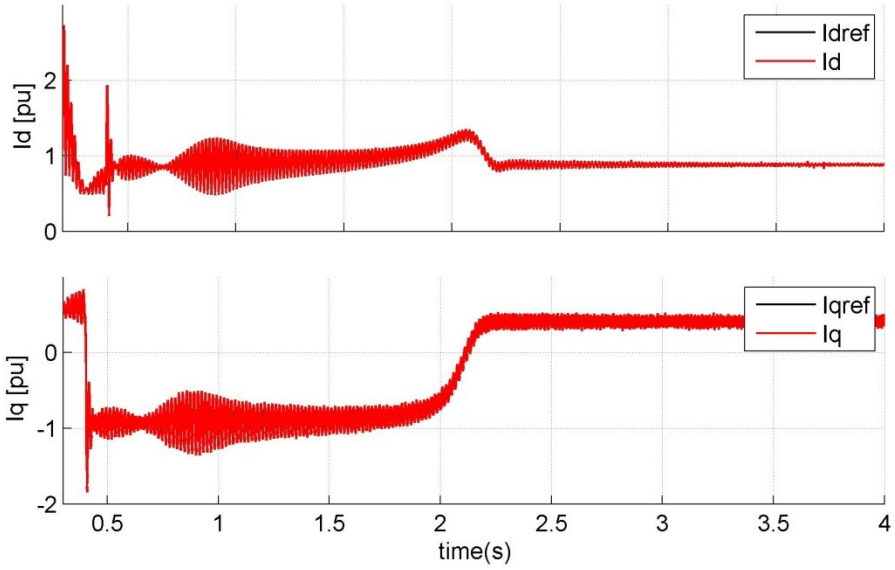

Figure 6-18 Line currents for 8 MVA induction-motor-starting

7 Discussion

7.1 Platform Voltage Estimator

The platform voltage estimator developed in section 5.1 is based on equations only valid for steady-state conditions. The results from testing the platform voltage estimator show that when the estimator is provided with accurate cable parameters, as in section 6.2, it is able to track the voltage perfectly in steady-state.

By comparing the results from the loss-of-all-load test, which has very fast transients, with the increase of passive load test, which has slower transients, it can be concluded that the voltage estimator tracks slow transients more accurately than fast transients. This is further validated by the results from the induction motor starting, where the transients are smaller and slower and the voltage estimator manages to track the platform voltage with reasonable accuracy.

It should be noted that all of these tests are done in a system with fixed frequency. This means that there are close to no frequency transients in this system. The voltage estimator is expected to show worse performance in a variable frequency system, due to the mathematical model only being valid for steady-state operation.

The cable model used in this thesis work, and for developing the voltage estimation equations, is very different from the 80 km HVAC-cable of a real system. Also in a real system the voltage and current estimation should be realized with equations valid for transients as well as for steady-state operation, to ensure proper autonomous operation of the system.

A dynamic voltage estimator should be based on a distributed parameters HVAC-cable model, or with a cable consisting of a considerably larger amount of pi-equivalents. Developing such a model for the voltage estimator is suggested as future work.

An accurate dynamic cable model used to estimate the current and voltage on the platform side of the cable would not only be interesting for usage during autonomous operation, but also for applying the control method suggested in section 3.2.2 to a real platform system.

7.2 Control Strategy 1

7.2.1 Autonomous Operation

In Control strategy 1, the platform voltage magnitude was regulated, while the frequency was kept fixed. The platform voltage estimator had access to the accurate parameters of the HVAC-cable model, but it did not compensate for the voltage

drop over the non-ideal transformers. Due to this, the results showed steady-state errors in the estimated platform voltage. The steady-state error varied with the load current, and hence the voltage drop over the transformer.

The controller tracked the estimated platform voltage within the required time and without violating the voltage transient upper and lower voltage limit for all three tests. However, due to the voltage estimation error, only the system with the increase of passive load satisfied the platform system requirements for both steady-state and transient operation.

The voltage estimation error was largest during the induction motor starting, when the actual platform voltage was 35 % lower than the rated platform voltage.

The voltage estimation accuracy could have been improved considerably by estimating the load current and calculating the actual platform voltage on the secondary side of the transformer. This is suggested as future work.

7.2.2 Constant and Variable DC-link Voltage

The platform system has been tested for operation with both constant and variable DC-link voltage, when control strategy 1 is regulating the platform voltage. The variable DC-link voltage can be seen in Figure 7-1 to have a very similar response to the system with applied constant DC-link voltage.

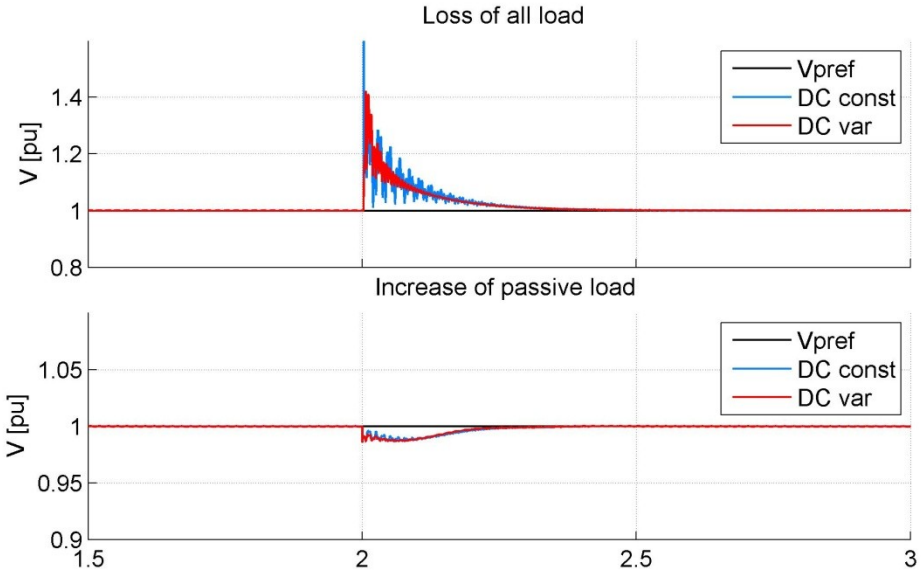

Figure 7-1 Platform system loss of all load and increase of passive load, tested for constant DC-link voltage and full B2B-VSC system with variable DC-link voltage

The transient in the DC-link voltage is small, and recovers fast for both the loss-of-all-load and increase-of-passive-load tests. The system with the variable DC-link voltage has fewer oscillations in the platform voltage during the transient.

The system with constant DC-link voltage can be seen to have a larger voltage spike when all loads are lost, while the system with the variable DC-link voltage has a smaller, but still not acceptable voltage transient when the load is lost.

The platform voltage plotted for both constant and variable DC-link voltage can be seen in Figure 7-2. The induction motor start transient is almost identical for the two systems as the motor is starting. When the induction motor is approaching the low slip region the DC-link voltage controller does not manage to track its reference, due to a limitation in the grid side current to its rated value of 1 pu. This leads to a voltage drop in the DC-voltage, and hence a voltage drop in the platform-side VSC output voltage, which again leads to the platform voltage drop.

At time t = 4.8 seconds, the grid current is again able to regulate the current because the applied DC-link voltage is below 1 pu, and hence the platform voltage reaches its reference after the large voltage transient. This could be avoided by increasing the grid-side current limit, trough increasing the grid-side system rated current. If the grid current limit was larger, the response of the full B2B-VSC system would be expected to have the same response for the induction motor start as the platform system operating alone with constant DC-link voltage.

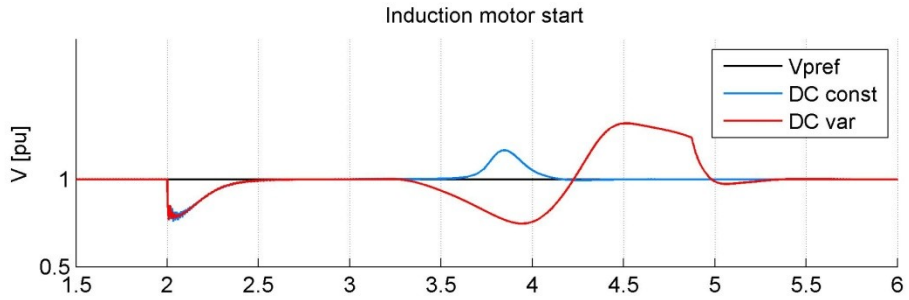

Figure 7-2 Platform system induction motor starting, tested for constant DC-link voltage, and full B2B-VSC system with variable DC-link voltage

7.2.3 Requirements Satisfied

Control strategy 1 has been tested for constant DC-link voltage, when both platform voltage measurements and estimated platform voltage has been available. It has also been tested with variable DC-link voltage, when it is connected in the full B2B-VSC configuration. Control strategy 1 controls the platform voltage magnitude, while the frequency is fixed.

If this control system was to be implemented for a real platform system, it needs to be able to regulate the platform voltage within the IEC 61892 standard limits for transient and steady-state peak voltage and recovery time. It also has to be able to maintain the voltage in steady-state within given boundaries. In addition to this, the system has to maintain stability for all normal system transients.

Table 7-1 Platform system requirements satisfied by control strategy 1

	Test no	Requirements	
		Steady-state voltage	Transient voltage
Platform system	1	X	
	2	X	X
	3	X	
Platform system, autonomous operation	1		
	2	X	X
	3		
Full B2B system	1	X	
	2	X	X
	3	X	

Control strategy 1 is not able to regulate the platform voltage within the specified voltage peak transient limit of $\pm$ 20 % of the rated platform voltage for any of the three different conditions it is tested for, that is: normal operation with constant DC-link voltage, autonomous operation, and full B2B-VSC operation, with variable DC-link voltage. A summary of the requirements satisfied for the three system configurations operating with the control strategy 1 is given in Table 7-1.

Loss-of-all-load and 8 MVA induction motor starting are worst-case load changes, and might not be representative for operation on all offshore platforms. Control strategy 1 shows good performance for the second load change test: the increase-of-passive-load test. Implementation and testing of control strategy 1 in systems with smaller expected load changes could be successful, and should be tested further.

Implementation of faster voltage magnitude control is expected to limit the voltage transient peaks, allowing the controller maintain the voltage at a more acceptable level. A faster voltage magnitude controller would make the system more likely to become unstable for large changes of platform load.

7.3 Control Strategy 2

Control strategy 2 regulates both the platform voltage magnitude and frequency. This strategy has been tested for three worst-case load changes when constant DC-link voltage is applied. The platform system was somehow modified to be able to apply the control strategy proposed in [41]. The modifications of the platform system included removing the shore-side pi-equivalent capacitance, and assuming the platform-side transformer to be ideal. Tests of this control strategy, in a system with high power and voltage levels, large line inductance and resistance, and with a load of 35 MVA, with load changes as those tested here, are not found in literature. Control strategy 2 shows excellent performance for platform voltage and frequency control. None of the load changes in the system are influencing the platform voltage and frequency visibly, and the system operation with controls strategy 2 satisfies all

the requirements for acceptable operation and control for all three load change tests. The requirements satisfied are summarized in Table 7-2.

Table 7-2 Platform system requirements satisfied by control strategy 2

	Test no	**Requirements**			
		Steady-state voltage	Transient voltage	Steady-state frequency	Transient frequency
Platform system	1	X	X	X	X
	2	X	X	X	X
	3	X	X	X	X

There are small oscillations in the frequency and platform voltage, but these are acceptable according to the requirements for platform system operation. The shore output voltage signal has considerable amounts of noise. This can be limited by placing a capacitor on shore, which would smooth the voltage out. There are also considerable oscillations in the line current. The SimPowerSystems™ inductances are modeled as current sources, and there are large inductances in both the induction motor and on the line. The platform transformer is modeled as an ideal transformer with a very large magnetizing inductance with almost no current flowing through it. Due to this, the cable inductor and the induction motor are nearly in series both before and after the increase of load. Having components as such in series has previously been shown to give oscillations in the three phase currents, which would introduce oscillations in the dq-currents. This is assumed to be part of the reason for the large oscillations in the system.

The dq-transform is referred to the platform angular frequency. Since the dq-currents are oscillating it can also be assumed that their frequency is somehow different from the frequency on the platform, which could be a sign of frequency variations throughout the system.

The noisy platform-side VSC output voltage is also assumed to draw distorted reactive power, and hence contribute to noise and oscillations in the reactive current component.

The results from testing control strategy 2 when applied to the full pi-equivalent circuit, including the shore based capacitor, are not provided here. Control strategy 2 is not able to regulate the platform voltage and frequency for load changes, in steady-state operation, with the large 23 MVA accumulate induction motor model, and the passive load of 2 MW, and hence was not able to regulate for load changes on the platform.

For control strategy 2 to be able to be implemented in the full platform system model presented in this thesis work, the current consumed or supplied by the shore pi-equivalent capacitor needs to be compensated for after the outer voltage control loops. The voltage drop over the non-ideal platform transformer would need to be compensated for after the inner current control loops.

A real 80 km HVAC-cable has more complex dynamics than the single pi-equivalent circuit that was used to model the cable model in this thesis work. The current flowing into the shore pi-equivalent capacitor would not be possible to measure as both the shore and offshore pi-equivalent cable capacitor would be non-existent.

A suggestion for how to implement this control strategy for a real system was presented in section 3.2.2. If a physical capacitor could be placed on the platform, the voltage at the capacitor node could be controlled based on the same principle as the one used for implementing control strategy 2. Implementation of a control system as such would require an accurate, dynamic current estimator. This current estimator should, based on the measured shore voltage and current and platform voltage, estimate the relation between the VSC output current on shore, and the current output of the HVAC-cable on the platform. The relation between these currents would have to be based on an accurate HVAC-cable model, and would clearly not be linear. This requires further research, but the results from the tests of control strategy 2 in this, modified platform system, shows a large potential for regulation of a real platform system with passive load.

If an active platform system was to be powered from shore, that is a platform system with a synchronous generator operating on the platform, supplying process heat and serving as a back-up device, control strategy 2 could be combined with the control system of the weak platform system controller, if implemented through the conventional weak grid control methods, summarized in section 2.3.3. The same controller components, that is the inner current control loop, the outer controllers could be used for the passive system control. This would increase the ability to disconnect the low efficiency gas turbine when it is not needed on the platform, which could reduce greenhouse gas emissions, gas turbine maintenance costs and it would make the gas previously used as fuel available for processing and sale, or reinjection to increase the oil production.

Implementation of the weak-grid controller and the interaction between the control modes for weak and passive grid is suggested as future work.

Testing of the full B2B-VSC configuration, that is operation of the system with variable DC-link voltage, is also suggested as future work.

8 Conclusion and Future Work

8.1 Conclusion

This thesis investigated the control of passive offshore platform voltage and frequency by means of a shore-based voltage source converter. The work completed in this thesis has contributed to the state of research by applying two existing control strategies in a novel manner, as described below.

An 80 km HVAC-cable and two transformers separate the shore-based B2B-VSCs from the passive platform installation to be controlled. Conventional stiff-grid controllers have been implemented for the grid-side VSC, controlling the DC-link voltage and reactive power drawn from the grid. The two platform voltage control methods implemented are denoted as control strategy 1 and 2. Control strategy 1 controls the platform voltage magnitude while keeping the frequency fixed, and is implemented by a simple PI-controller. Control strategy 2 controls both the platform voltage magnitude and frequency. This second control strategy is based on a cascaded control configuration, similar to a weak-grid controller. Both controllers were tested for three worst-case changes of platform load: loss of all loads, increase of passive load, and large induction motor starting. Testing and comparison of control strategy 1 and 2, for these types and magnitudes of load has not previously been conducted. The platform voltage and frequency transients of the system, and the steady-state voltage and frequency were evaluated based on the defined platform system requirements for acceptable operation and control.

Control strategy 1 was tested for both normal and autonomous operation, when a constant DC-link voltage was applied. In addition to this, it was tested in a full B2B-VSC configuration where the grid-side VSC was controlling the DC-link voltage and the flow of reactive power from the grid. In all of the three configurations, control strategy 1 failed to meet the system requirements defined by IEC 61892, for allowable voltage transient during loss of all load and large induction motor start. The worst system voltage transient was during motor start, when the platform system was operating autonomously, with the estimated platform voltage applied. This was partially due to estimation errors in the developed steady-state platform voltage estimator. Improvement of the platform voltage estimator is suggested as future work.

Control strategy 2 was tested with constant DC-link voltage, when platform voltage measurements were available. The simulation results show no visible voltage or frequency transients for any of the three load change tests applied, and the system operation satisfied the system requirements for all the tests. The platform voltage and frequency is independent of the load dynamics, which is a desirable quality when controlling the voltage on a complex platform configuration. The

platform-side VSC shore output voltage had noise which distorted the reactive line current waveform; a filter should be placed on shore to avoid this.

Control strategy 2 shows promising potential for controlling the platform voltage and frequency from shore. However, further research must be done before this control strategy can be utilized in a real system.

It should also be noted that control strategy 2 consists of the same components as a conventional weak-grid control system that would be implemented in a platform system supplied from shore, when a gas turbine driven synchronous generator is operating on the platform. This is very advantageous because expanding the weak-grid system control to include passive system control would allow the platform operator to more easily disconnect the low efficiency gas turbine when it is not needed on the platform. This could reduce greenhouse gas emissions and gas turbine maintenance costs and make the gas previously used as fuel available for processing and sale, or reinjection to increase the oil production.

8.2 Future work

Many specific improvements can be done for the models implemented in this thesis. The steady-state voltage estimation model needs to be expanded to include estimation of the load current, and hence the actual platform voltage on the secondary side of the platform transformer. For autonomous operation of an actual platform system, implementing dynamic voltage estimation should be considered. This would be more accurate for fast voltage transients but would require a more accurate mathematical model for the HVAC-cable.

The modified platform model used for implementation and testing of control strategy 2 should be extended to include the shore side pi-equivalent capacitor, and the non-ideal platform transformer. The current flowing through the shore capacitor should be measured and compensated for after the voltage control loop, while the voltage drop over the non-ideal transformer should be compensated for at the output of the inner current control loops. Control strategy 2 should also be tested for operation in the full B2B-VSC configuration with variable DC-link voltage. Implementation of the weak-grid system controller, and interaction between the control modes for weak and passive grid should also be done.

Further research on the possibility of implementing control strategy 2 for control of a real platform system, through control of the voltage at the node of a physical capacitor based on the platform, needs to be done. This would entail developing an accurate dynamic current estimator to provide the non-linear relation between the platform-side VSC output current, and the current output of the HVAC-cable on the platform, again requiring a more accurate mathematical model of the HVAC-cable.

Many improvements can be made to make the system more like that of a real one. The platform load can be modeled more accurately and a larger range of load changes can be applied to test the system, a full switching model for studying the effect of switching losses and harmonics in the system could be used, all of which is proposed as future work.

9 References

[1] N. P. D. (NPD). (2011, 19.04). *Utslipp til luft (Emissions to Air)*. Available: http://www.npd.no/publikasjoner/rapporter/miljoteknologi/5-utslipp-til-luft/#5

[2] Miljøverndepartementet. (2006-2007, 19.04). *Stortingsmelding no. 34, Norsk klimapolitikk, Petroleumssektoren*. Available: http://www.regjeringen.no/nb/dep/md/dok/regpubl/stmeld/2006-2007/Stmeld-nr-34-2006-2007-/13.html?id=473485

[3] Regjeringen. (2006-2007, 19.04). *Stortingsmelding no.34, Regjeringens klimapolitiske mål*. Available: http://www.regjeringen.no/nb/dep/md/dok/regpubl/stmeld/2006-2007/Stmeld-nr-34-2006-2007-/4.html?id=473434

[4] J. C. Myhre, "Electrical Power Supply to Offshore Oil Installations by High Voltage Direct Current Transmission," Dr.Eng, Electric Power Engineering, Power Conversion, NTNU, Trondheim, 2001.

[5] P. J. Lars Stendius, "The Challenges of Offshore Power System Construction Troll A, Electrical Power DeliveredSuccessfully to an Oil and Gas Platform in the North Sea," presented at the EWEC 2006, Athens, 2006.

[6] T. N. Nils Hörle, Asmund Maeland, Kjell Ericsson, "Electrical Supply for Offshore Installations made Possible by Use of VSC Technology," presented at the Cigrè Paris, France, 2002.

[7] Statoil. (2007, 20.04). *Facts about Ormen Lange*. Available: http://www.statoil.com/en/OurOperations/ExplorationProd/partneroperatedfields/OrmenLange/Pages/default.aspx

[8] H. Gedde*, et al.*, "Ormen Lange Long Step-out Power Supply," 2009.

[9] T. E. Moen, "Status, fordeler og utfordringer ved elektrifisering innen olje og gass," unpublished.

[10] ABB. (2011-02, 19.04). *Submarine Power Cables, Cables for offshore platforms and wind farms*. Available: http://www05.abb.com/global/scot/scot245.nsf/veritydisplay/7c2c265ecc997719c125783900465af2/$file/submarine%20power%20cables%20for%20offshore%20wind%20farms%20and%20platforms%202gm5010-gb%20oil%20rev%202011-02.pdf

[11] O. L. (OLF), "Elkraft fra land til norsk sokkel," 2003.

[12] ABB. (2004, 20.04). *Powering Abu Safah offshore oil-field in Saudi Arabia*. Available: http://www05.abb.com/global/scot/scot245.nsf/veritydisplay/4fef53c03527

7594c12571fb0033d8ba/$file/project%20saudi%20aramco%20115%20kv%20xlpe%20subm.pdf

[13] P. Kundur, *Power System Stability and Control*: McGraw-Hill Professional 1994.

[14] Siemens. (2007, 26.04). *HVDC PLUS, - Technology, Benefits and Applications*. Available: http://www.siemens.com/annual/08/pool/04_produkte_loesungen/03_energy/07_power_transmission/hvdc_plus.pdf

[15] G. Asplund*, et al.*, "DC transmission based on voltage source converters," 1997.

[16] N. M. T.M.Undeland, W.P.Robbins, *Power Electronics, Converters, Applications and Design*, 3 ed.: John Wiley and Sons, Inc, 2003.

[17] K. Meah and S. Ula, "Comparative Evaluation of HVDC and HVAC Transmission Systems," in *Power Engineering Society General Meeting, 2007. IEEE*, 2007, pp. 1-5.

[18] H. Brakelmann, "Efficiency of HVAC power transmission from offshore-windmills to the grid," in *Power Tech Conference Proceedings, 2003 IEEE Bologna*, 2003, p. 6 pp. Vol.2.

[19] T. M. Haileselassie, "Control of Multiterminal VSC-HVDC (MTDC) Systems," Norwegian University of Science and Technology, 2008.

[20] A. Å. Kristin Høvik, Professor Tore Undeland, Kamran Sharifabadi, "Kraftelektronikkens rolle ved elektrifisering av eksisterende offshore installasjoner, med kraft fra offshore vindpark ok kraft fra land," presented at the NEF Teknisk Møte 2011, Trondheim, NTNU, 2011.

[21] IEC, "IEC 61892: Mobile and fixed offshore units – Electrical installations " in *Part 1: General requirements and conditions*, 2010.

[22] N. Mohan, *Advanced electric drives: analysis, control and modeling using simulink*: Mnpere, 2001.

[23] P. C. Krause*, et al.*, *Analysis of electric machinery and drive systems*: IEEE press, 2002.

[24] J. A. W. Suul, "Control of Variable Speed Pumped Storage Hydro Power Plant for Increased Utilization of Wind Energy in an Isolated Grid," Master of Science Mater Thesis, Electric Power Engineering, NTNU, Trondheim, 2006.

[25] N. Mohan, *First course on power systems*: MNPERE, 2006.

[26] C. Du, *VSC-HVDC for industrial power systems* vol. 68, 2007.

[27] C. Du, "The control of VSC-HVDC and its use for large industrial power systems," Licenciate of Eengineering, Chalmers University of Technology, 2003.

[28] C. Bajracharya, "Control of VSC-HVDC for wind power," Master of Science, Energi Conversion NTNU, Trondheim, 2008.

[29] N. Mohan, *First Course on Power Electronics*. Minneapolis: MNPERE, 2007.

[30] D. O. Neacsu, "Space Vector Modulation - An Introduction, Turtorial at IECON 2001," presented at the IECON'01, 2001.
[31] ABB, "XLPE Submarine Cable Systems, Attachment to XLPE Land Cable Systems, User's Guide," 2010.
[32] E. A. P. L. a. Electrix, "Connection to 200 kV Main Grid," 2008.
[33] S. Rahimi, *et al.*, "Identification of problems when using long high voltage AC cable in transmission system I: switching transient problems," in *Transmission and Distribution Conference and Exposition, 2008. T&D. IEEE/PES*, 2008, pp. 1-7.
[34] Mathworks. (2011, 18.05). *PI Section Line*. Available: http://www.mathworks.com/help/toolbox/physmod/powersys/ref/pisectionline.html
[35] Mathworks. (2011, 28.04). *Asynchronous Machine*. Available: http://www.mathworks.com/help/toolbox/physmod/powersys/ref/asynchronousmachine.html
[36] DanfossA/S, *Værd at vide om frekvensomformere*: Danfoss, 1991.
[37] C. Bajracharya, *et al.*, "Understanding of tuning techniques of converter controllers for VSC-HVDC," 2008.
[38] G. Li, *et al.*, "Modeling of VSC-HVDC and control strategies for supplying both active and passive systems," 2006, p. 6 pp.
[39] Z. Guibin, *et al.*, "Supply passive networks with VSC-HVDC," in *Power Engineering Society Summer Meeting, 2001. IEEE*, 2001, pp. 332-336 vol.1.
[40] C. Hairong, "Research on the control strategy of VSC based HVDC system supplying passive network," in *Power & Energy Society General Meeting, 2009. PES '09. IEEE*, 2009, pp. 1-4.
[41] M. B. Delghavi and A. Yazdani, "A control strategy for islanded operation of a Distributed Resource (DR) unit," in *Power & Energy Society General Meeting, 2009. PES '09. IEEE*, 2009, pp. 1-8.
[42] A. K. Moharana, *et al.*, "VSC Based HVDC System for Passive Network with Fuzzy Controller," in *Power Electronics, Drives and Energy Systems, 2006. PEDES '06. International Conference on*, 2006, pp. 1-4.
[43] H. Karimi, *et al.*, "A Linear Quadratic Gaussian Controller for a Stand-alone Distributed Resource Unit-Simulation Case Studies," in *Power Engineering Society General Meeting, 2007. IEEE*, 2007, pp. 1-6.
[44] C. Se-Kyo, "A phase tracking system for three phase utility interface inverters," *Power Electronics, IEEE Transactions on,* vol. 15, pp. 431-438, 2000.
[45] K. Young and R. A. Dougal, "SRF-PLL with dynamic center frequency for improved phase detection," in *Clean Electrical Power, 2009 International Conference on*, 2009, pp. 212-216.
[46] R. MIZERA, "Modification of Symmetric Optimum Method," 2005.
[47] R. H. Nigel HAMPTON, Hakan LENNARTSSON, Harry ORTON, Ram RAMACHANDRAN, "Long life XLPE Insulated Power Cable," presented at the Jicable, Paris, France, 2007.

References

A Additional Parameters

A.1 System Base Values

Table 9-1 System base apparent power, voltages and currents

Parameter	Value	Unit
System rated apparent power [$S_{T1,rated}$]	40	MVA
Grid-side rated voltage [V_{base1}]	3.3	kV-LLrms
Platform-side converter voltage [V_{base1}]	3.3	kV-LLrms
Rated cable voltage [V_{base2}]	66	kV-LLrms
Rated platform voltage [V_{base3}]	6.6	kV-LLrms
Grid-side rated current [I_{base1}]	7698	A-rms
Platform-side converter rated current [I_{base1}]	7698	A-rms
Rated cable current [I_{base2}]	349.91	A-rms
Rated platform current [I_{base3}]	3499.1	A-rms

A.2 Transformer parameters

Table 9-2 Shore-based transformer, T1 parameters

Parameter	Value	Unit
Rated power [$S_{T1,rated}$]	40	MW
Rated primary voltage [$V_{T1,p}$]	3	kV
Rated secondary voltage [$V_{T1,s}$]	66	kV
Primary side resistance [$R_{T1,p}$]	0.002	pu
Secondary side resistance [$R_{T1,s}$]	0.002	pu
Primary side leakage inductance [$L_{T1,p}$]	0.1	pu
Secondary side leakage inductance [$L_{T1,s}$]	0.1	pu
Magnetizing resistance [$L_{T1,m}$]	500	pu
Magnetizing inductance [$R_{T1,m}$]	500	pu

Table 9-3 Platform-side transformer T2 parameters

Parameter	Value	Unit
Rated power [$S_{T2,rated}$]	40	MW
Rated primary voltage [$V_{T2,p}$]	66	kV
Rated secondary voltage [$V_{T2,s}$]	6.6	kV
Primary side resistance [$R_{T2,p}$]	0.002	pu
Secondary side resistance [$R_{T2,s}$]	0.002	pu
Primary side leakage inductance [$L_{T2,p}$]	0.1	pu
Secondary side leakage inductance [$L_{T2,s}$]	0.1	pu
Magnetizing resistance [$L_{T2,m}$]	500	pu
Magnetizing inductance [$R_{T2,m}$]	500	pu

Table 9-4 Platform-side ideal transformer T2 parameters

Parameter	Value	Unit
Rated power [$S_{T2,rated}$]	40	MW
Rated primary voltage [$V_{T2,p}$]	66	kV
Rated secondary voltage [$V_{T2,s}$]	6.6	kV
Primary side resistance [$R_{T2,p}$]	0	pu
Secondary side resistance [$R_{T2,s}$]	0	pu
Primary side leakage inductance [$L_{T2,p}$]	0	pu
Secondary side leakage inductance [$L_{T2,s}$]	0	pu
Magnetizing resistance [$L_{T2,m}$]	500	pu
Magnetizing inductance [$R_{T2,m}$]	500	pu

A.3 Induction Motor Parameters

Table 9-5 Accumulated induction motor parameters

Parameter	Value	Unit
Rated apparent power [$S_{ind,rated}$]	23	MVA
Rated voltage [$V_{ind,rated}$]	6.6	kV
Stator resistance [R_s]	0.009	pu
Rotor resistance [R_r]	0.020	pu
Stator leakage inductance[L_{sl}]	0.196	pu
Rotor leakage inductance [L_{rl}]	0.026	pu
Magnetizing inductance [L_m]	2	pu
Inertia coefficient [H]	0.65	

Friction factor [F]	0.05479	
Number of poles [p]	2	
Starting torque [$T_{m,start}$]	0.05	pu

Table 9-6 Induction motor parameters, for induction motor starting

Parameter	**Value**	**Unit**
Rated apparent power [$S_{ind,rated}$]	8	MVA
Rated voltage [$V_{ind,rated}$]	6.6	kV
Stator resistance [R_s]	0.009	pu
Rotor resistance [R_r]	0.020	pu
Stator leakage inductance[L_{sl}]	0.196	pu
Rotor leakage inductance [L_{rl}]	0.026	pu
Magnetizing inductance [L_m]	2	pu
Inertia coefficient [H]	0.65	
Friction factor [F]	0.05479	
Number of poles [p]	2	
Starting torque [$T_{m,start}$]	0.05	pu

B MATLAB® Simulink™ SimPowerSystems™ Model

B.1 Voltage Estimator Model

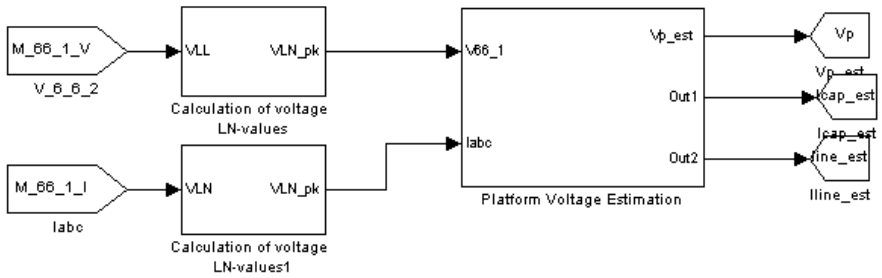

Figure 9-1 Voltage estimator overview of inputs and outputs

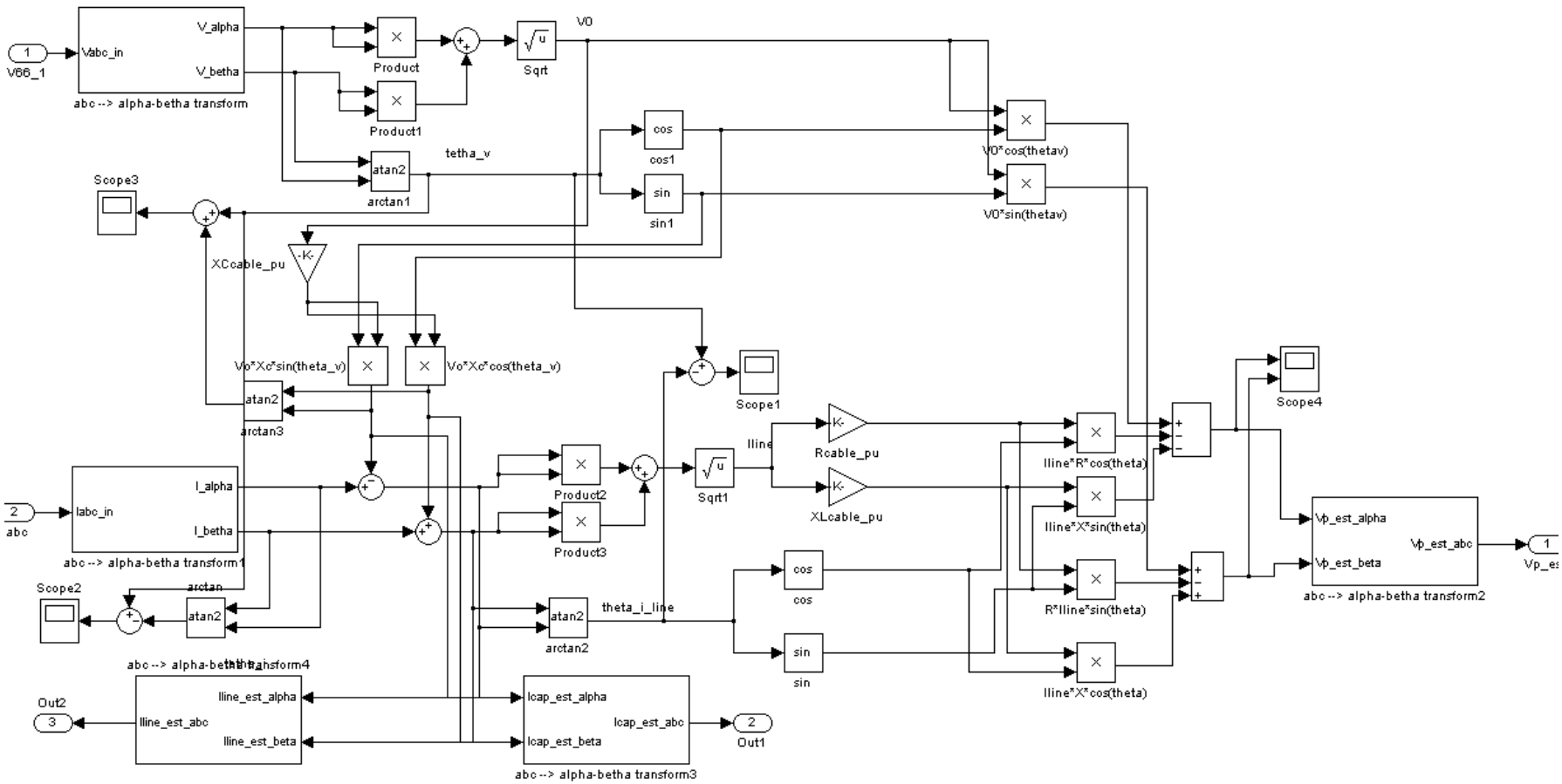

Figure 9-2 Voltage estimator Simulink™ model

B.2 Grid Side Model

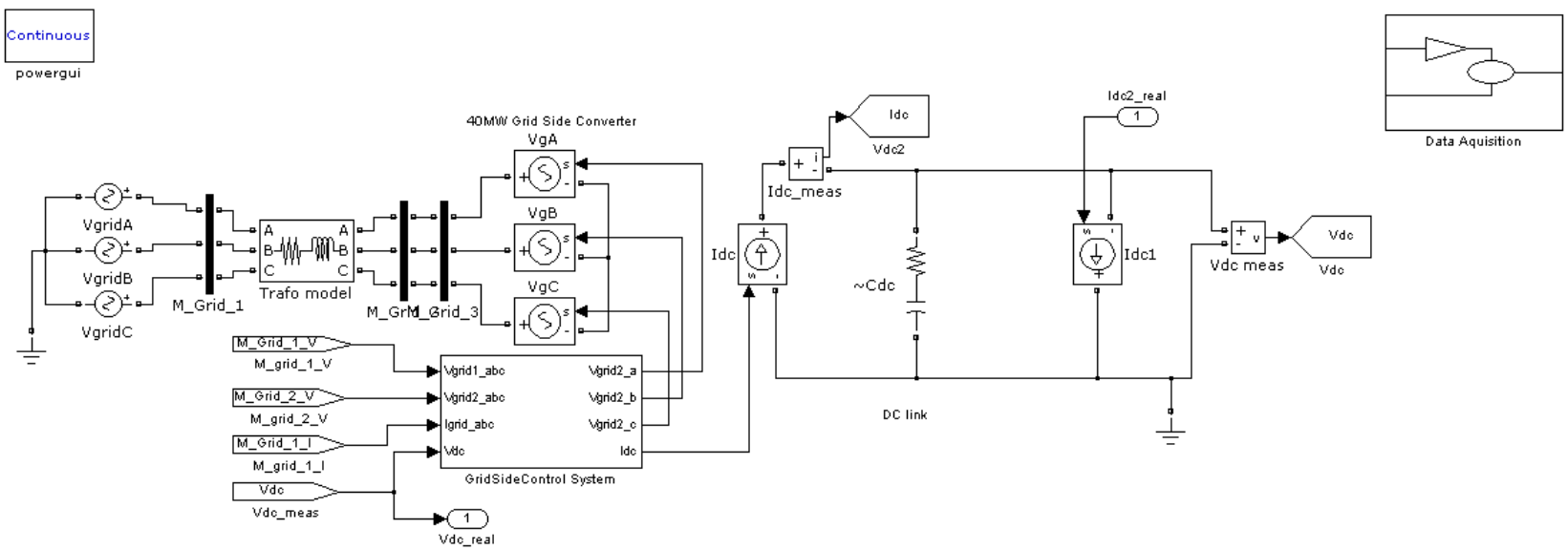

Figure 9-3 Overview of grid-side model connected to DC-link

B.2.1 Grid Side Controllers

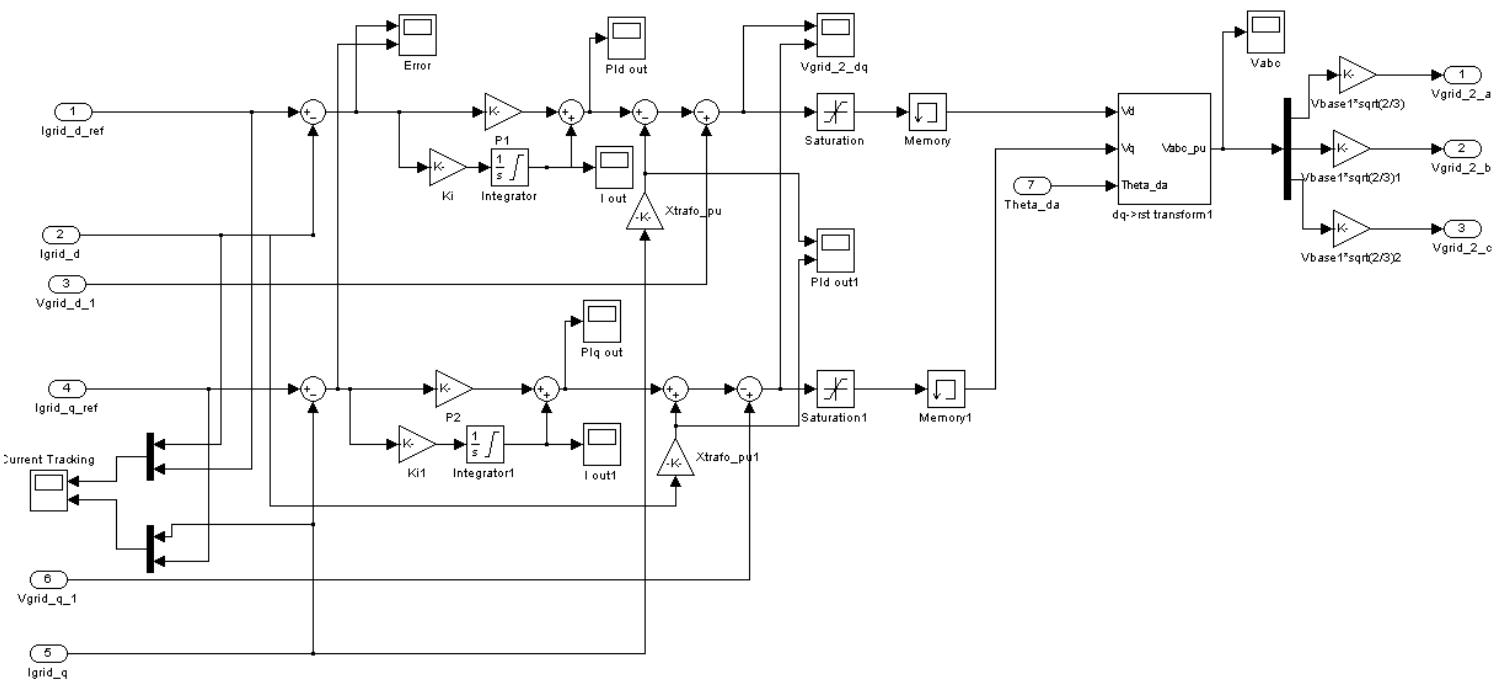

Figure 9-4 Inner current control loop, grid-side system

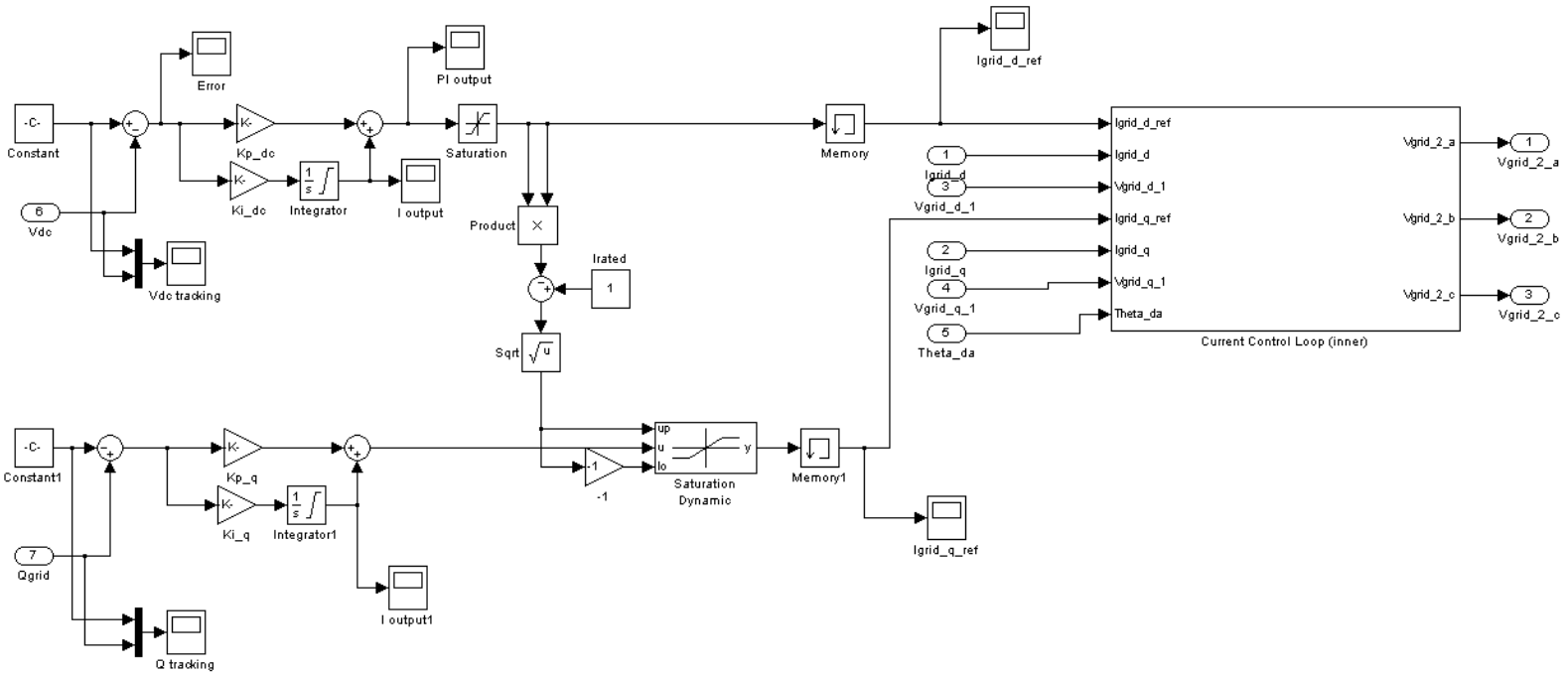

Figure 9-5 Outer control loops for DC-link voltage control and reactive power control

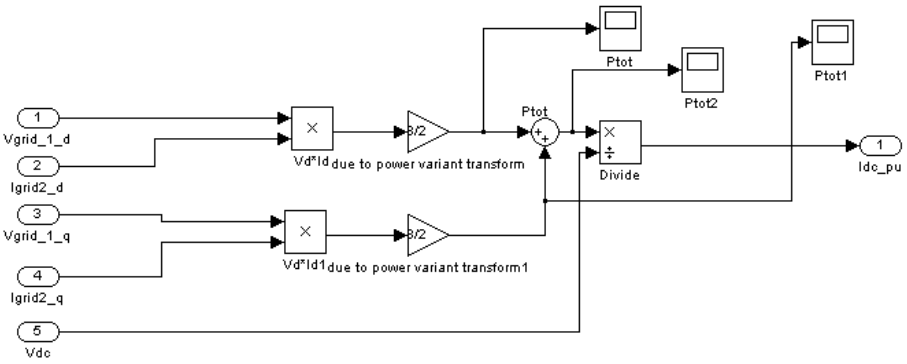

Figure 9-6 Power conservation block diagram

B.4 Platform System Model

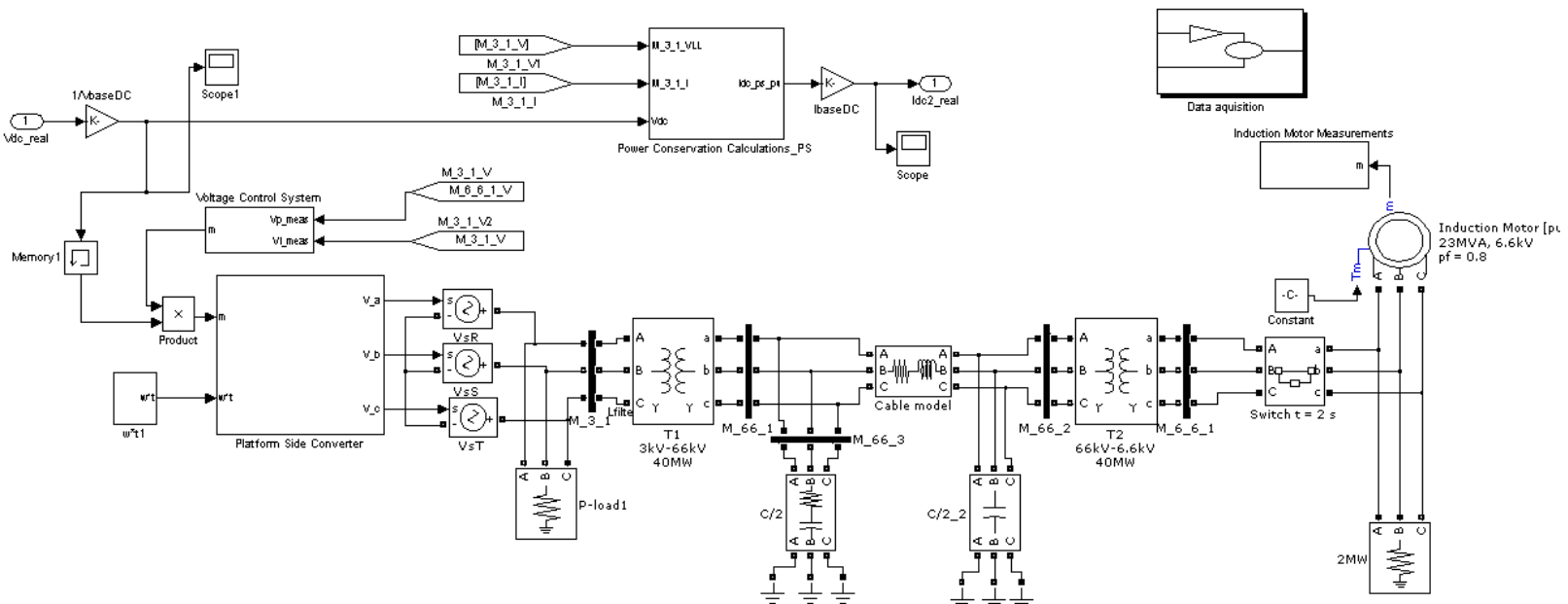

Figure 9-7 Overview of platform-system model used for tests with control strategy 1

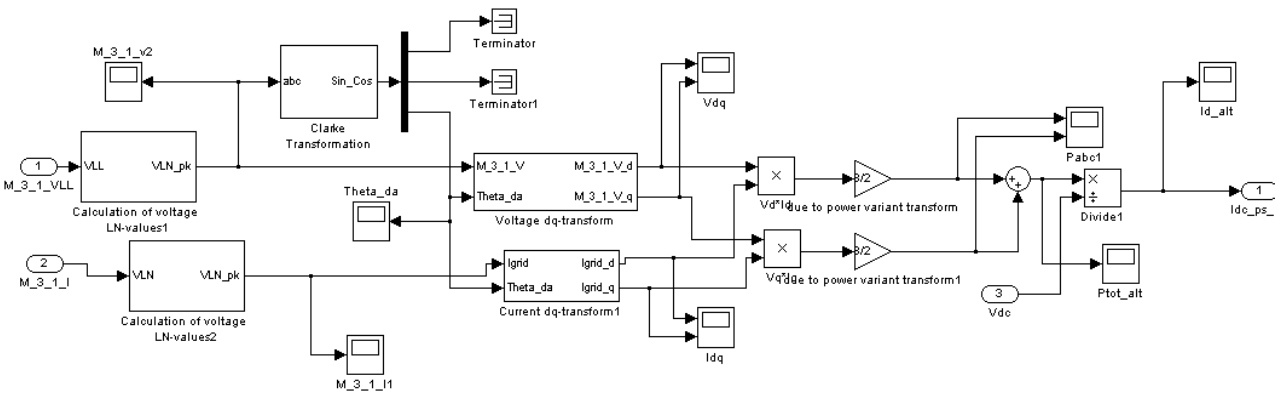

Figure 9-8 Platform-side system connection to grid-side system through power conserved equations

B.4.1 Control Strategy 1

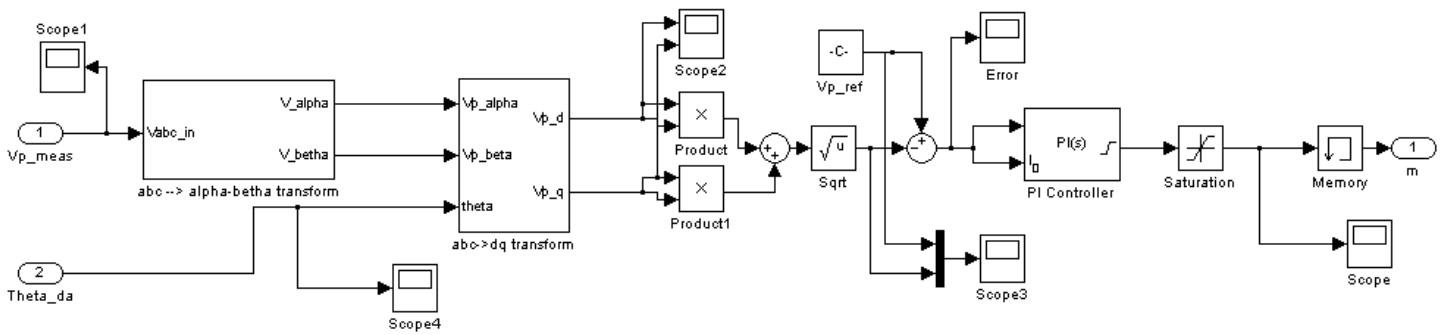

Figure 9-9 Block diagram of control strategy 1

B.4.2 Control Strategy 2

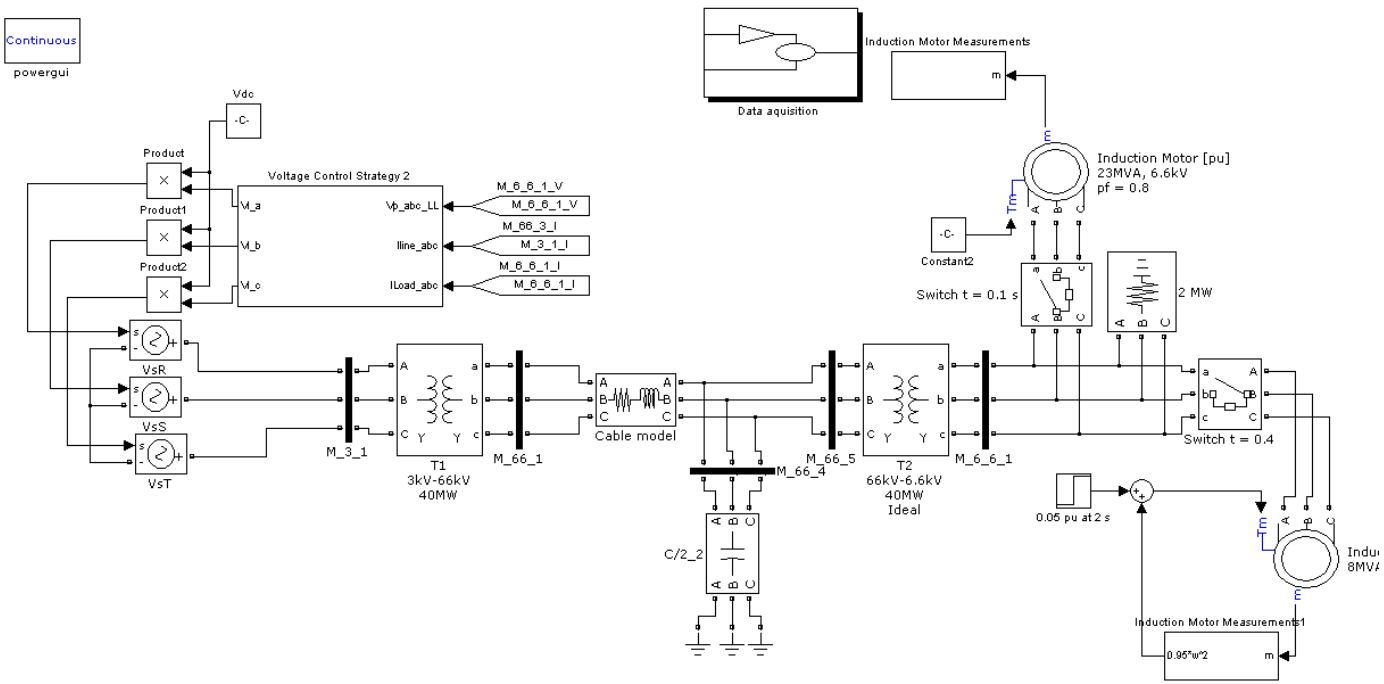

Figure 9-10 Platform system model, used for testing of control strategy 2

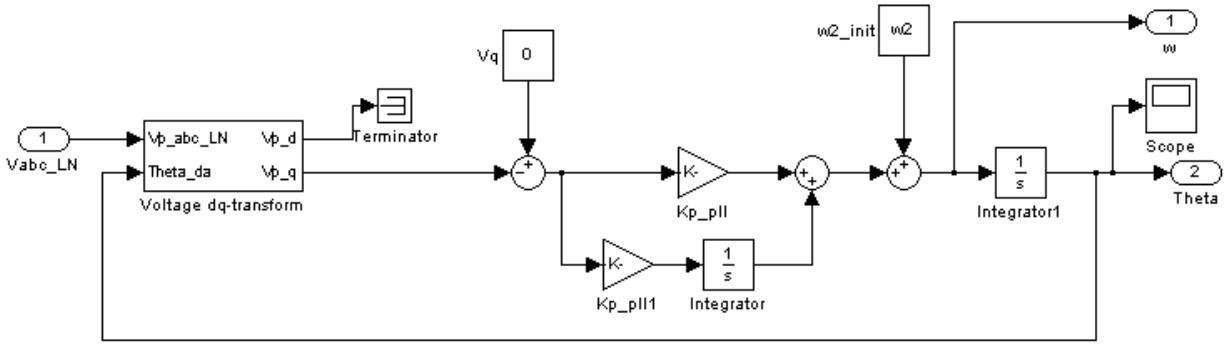

Figure 9-11 Phase lock loop implemented in control strategy 2

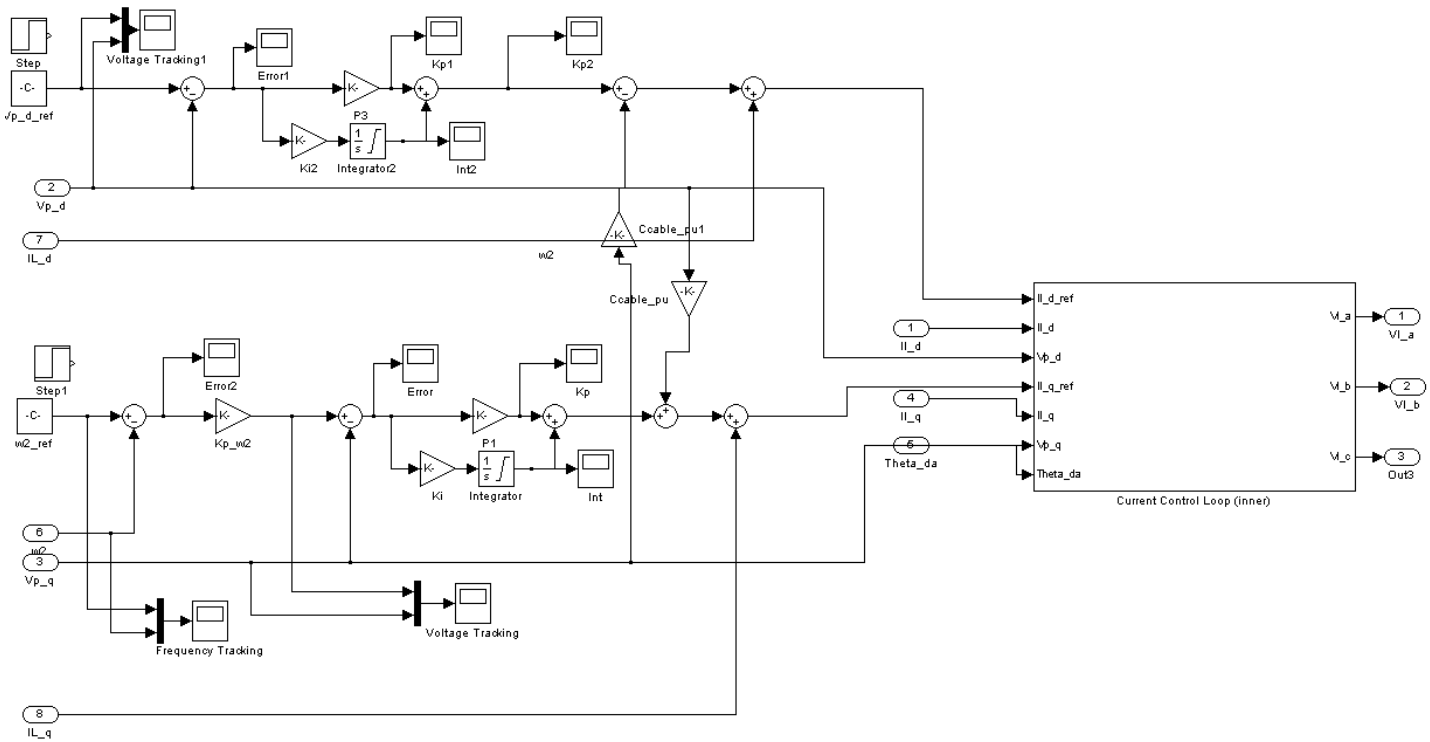

Figure 9-12 Outer voltage and frequency control loops, implemented for control strategy 2

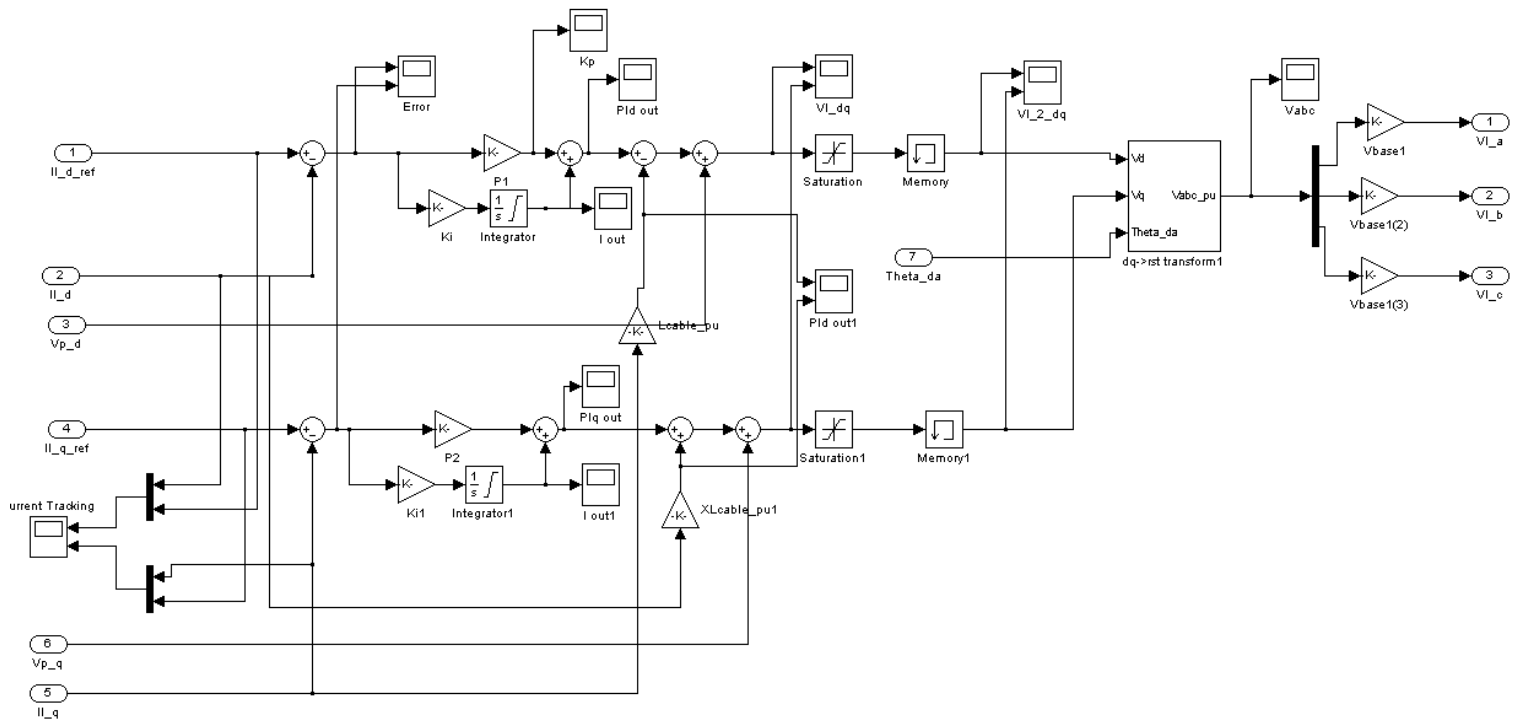

Figure 9-13 Inner current control loop, implemented for control strategy 2

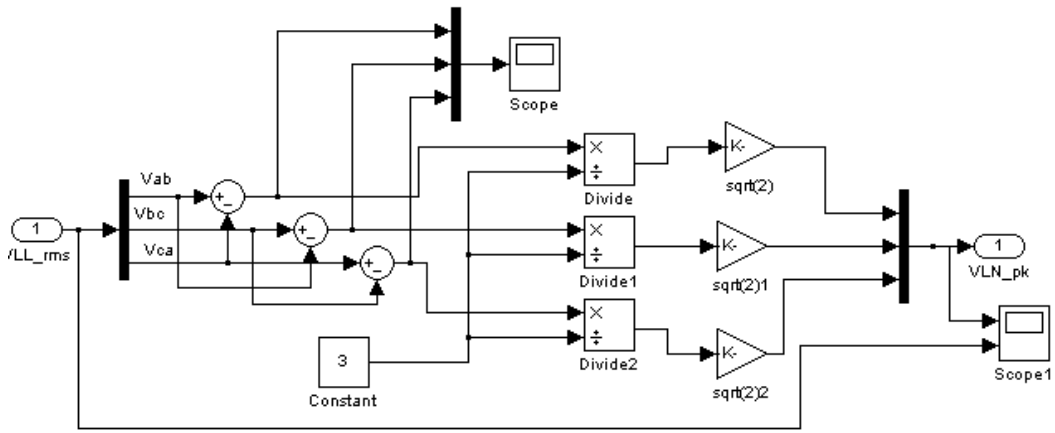

Figure 9-14 Conversion between line-to-line RMS-values and line-to-neutral peak values

C Additional Simulation Results

C1. Control Strategy 1

C.1.1 Platform System Tests

C.1.1.1 Loss of all loads

Table 9-7Results from control strategy 1, loss of all load test

Description	$\|V_p\|$	%	t_{rec}
Control Strategy 1	1.62	+62	0.45
Control Strategy 1, autonomous	1.209	+20.9	0.6

Table 9-8 Results from voltage estimation, loss of all load test

Description	Error	%
Estimation error before loss of all load	- 0.0236 pu	3.3
Estimation error after loss of all load	+ 0.0677 pu	9.4
Platform voltage error after loss of all load	+ 0.0926 pu	14.1

C.1.1.2 Increase of passive load

Table 9-9Results from control strategy 1, increase of load

Description	$\|V_p\|$	%	t_{rec}
Control Strategy 1, real voltage applied	0.986	-1.4	0.4
Control Strategy 1, estimated voltage applied	0.986	-1.4	0.4

Table 9-10 Results from voltage estimation, increase of load

Description	Error	%
Estimation error before increase of load	- 0.0236 pu	3.3
Estimation error after increase of load	- 0.296 pu	4.2
Platform voltage error after increase of load	-0.006 pu	0.8

C.1.1.3 Induction motor starting

Table 9-11Results from control strategy 1, induction motor start

Description	$\|V_p\|$	**%**	t_{rec}
Control Strategy 1, Transient 1	0.7621	-23.8	0.62
Control Strategy 1, Transient 2	1.166	+16.6	0.967
Control Strategy 1, estimated voltage applied, Transient 1	1.058	+5.8	0.62
Control Strategy 1, estimated voltage applied, Transient 1	1.026	+2.6	1.029

Table 9-12 Results from voltage estimation, induction motor start

Description	**Error**	**%**
Estimation error before motor start	-0.0236	3.3
Estimation error during motor start	-0.2479	35
Estimation error after motor start	0.0544 pu	7.69
Platform voltage error after motor start	0.031 pu	4.4

C.1.2 Full B2B-VSC configuration

C.1.2.1 Loss of all load

Table 9-13 Result from full B2B-VSC system loss of all load test

	Peak	**%**	t_{rec}
$\|V_p\|$	1.424	+42.4	0.412
V_{dc}	1.797	+8	0.145
Q	0	0	0

C.1.2.2 Increase of passive load

Table 9-14 Result from full B2B-VSC system increase of passive load

	Peak	**%**	t_{rec}
$\|V_p\|$	0.966	-3.4	0.39
V_{dc}	1.624	-2.3	0.228
Q	0	0	0

C.1.2.3 Induction motor starting

Table 9-15 Full B2B-VSC system, induction motor starting

	Peak 1	**%**	t_{rec1}	**Peak 2**	**%**	t_{rec2}	**Peak 3**	**%**	t_{rec3}
$\|V_p\|$	**0.7673**	**-23.3**	**0.686**	**0.7467**	**-25.24**	**0.957**	**1.32**	**32**	**1.08**
V_{dc}	**1.672**	**2.3**	**0.06**	**0.6507**	**-60**	**1.53**	**1.91**	**6.3**	**0.22**
Q	**0.1811**	**18.11**	**0.097**	**-**	**-**	**-**	**-**	**-**	**-**

D NEF-Paper

KRAFTELEKTRONIKKENS ROLLE VED ELEKTRIFISERING AV EKSISTERENDE OFFSHORE INSTALLASJONER, MED KRAFT FRA OFFSHORE VINDPARK OG KRAFT FRA LAND

Av *Atle Rygg Årdal og Kristin Høvik, Prof. Tore M. Undeland (NTNU), Dr. Ing Kamran Sharifabadi (Statoil)*

Sammendrag:

Gassturbindrevne synkrongeneratorer med lav virkningsgrad dekker offshore plattformers kraftbehov, og utgjør en stor del av Norges CO_2-utslipp. Dette kan reduseres ved kraftforsyning fra mindre utslippsintensive kilder.

Denne artikkelen diskuterer motivasjonen bak elektrifisering, og gir en oversikt over eksisterende prosjekter. Ulike teknologier som benyttes blir presentert, med hovedfokus på bruk av kraftelektronikk. Videre beskrives to alternativer til kraftforsyning av offshore oiljeplattform: Tilknyttning av kraft fra land og tilknytting av kraft fra offshore vindkraft. Systemet med kraft fra land til plattformen simuleres for tap av synkrongenerator på plattformen for å belyse problemer som kan oppstå i forbindelse med dette. Systemet med kraft fra offshore vindpark tilknyttet plattformen simuleres for start av en stor direktekoblet induksjonsmotor. Her illustreres det hvordan reaktiv effektkompensasjon fra frekvensomformere i vindturbiner kan redusere spenningsvariasjoner ved hendelser på plattformen. Simuleringer er utført i PSCAD® og MATLAB® Simulink™ SimPowerSystems™.

1 INTRODUKSJON

Global oppvarming er en stor utfordring for verdens befolkning. Konsekvensene kan bli fatale hvis det ikke iverksettes tiltak for å redusere utslippene av CO_2 og andre klimagasser. En stor del av verdens CO_2-utslipp kommer fra elektrisitetsproduksjon, og det er et sterkt fokus på både å forbedre ekstisterende produksjonsmetoder og på nye fornybare energikilder. Landbasert elektrisitetsproduksjon i Norge er i all

hovedsak utslippsfri vannkraft, men gjennom overføringskabler til utlandet importeres det store mengder kullkraft i år med lite nedbør.

Olje- og gassinstallasjoner i Nordsjøen er tradisjonelt forsynt av gassturbiner. Driftstekniske krav og restriksjoner på arealbruk gjør at disse har en lav virkningsgrad, og dermed høye CO_2-utslipp per produsert energienhet. Virkningsgraden er rundt 35 % for en vanlig offshore gassturbin [1]. Den norske kontinentalsokkelen er estimert til å stå for 29 % av Norges totale CO_2-utslipp, hvorav 90 % kommer fra elektrisitetsproduksjon [2]. En reduksjon i utslipp fra petroleumssektoren kan være en viktig bidragsyter til å nå målene som Norge har forpliktet seg til gjennom Kyotoavtalen og Gøteborgprotokollen [3].

For at elektrifisering av oljeplattformer skal føre til reduksjoner i CO_2-utslipp må den alternative energien komme fra en kilde med mindre utslipp enn det eksisterende kraftverket på plattformen. Et moderne kombinert gass- og dampkraftverk på land kan ha virkningsgrad rundt 60 %, og produserer dermed renere elektrisitet enn gassturbinene på plattformer. Flere momenter påvirker imidlertid regnestykket. Det er knyttet overføringstap til elektrifisering, og overskuddsvarme fra gassturbiner på sokkelen blir i dag utnyttet til oppvarming. Konklusjonen i [1] er at plattformer må elektrifiseres fra fornybare energikilder for å oppnå store reduksjoner i CO_2-utslipp.

Blant fornybare energikilder blir ofte offshore vindkraft trukket frem som et lovende alternativ. Potensialet er stort, men det kreves mye arbeid for å redusere de høye kostnadene som er assosiert med offshore vindkraft i dag. Få vindparker er blitt bygget, men mange prosjekter er i planleggingsfasen. 4,5 GW er meldt til NVE i norske havområder [4]. Det er gjort forskning på å koble en offshore vindpark til oljeinstallasjoner. [5] presenterer simuleringer og beregninger på et slikt system uten tilkobling til land.

CO_2-avgift på gassen som blir brukt til å lage elektrisitet er den viktigste økonomiske drivkraften til offshore elektrifisering. I

tillegg representerer gassen en tapt kostnad siden den kan selges til markedet i de fleste tilfeller. På den andre siden må det kjøpes elektrisitet i en situasjon med elektrifisering fra land.

Denne artikkelen har som mål å studere elektrifisering av offshore plattformer for å på lang sikt kunne redusere bruken av gassturbiner til elektrisitetsproduksjon på oljeplattformer. Hovedfokus er på rollen til kraftelektronikk ved elektrifisering av eksisterende oljeplattformer. I avnsitt 2.1 gis det en beskrivelse av teknologien som benyttes i HVDC- og HVAC-overføring. Hvordan kraftelektronikk kan utnyttes i offshore vindturbiner diskuteres i avsnitt 0. Avsnitt 3 gir en beskrivelse av de to systemene som undersøkes, med referanser til to masterprosjekter ved NTNU. I avsnitt 4 presenteres simuleringer av systemene, for å belyse utfordringer og muligheter ved elektrifisering. Avsnitt 5 oppsummerer og konkluderer resultatene fra simuleringene, og den generelle diskusjonen i artikkelen.

2 KRAFTELEKTRONIKK I OFFSHORE SYSTEMER

Bruk av kraftelektronikk ved elektrifisering av plattformer øker kontrollmulighetene fra land og fra vindparken. Dette kapittelet gjennomgår grunnleggende omformerprinsipper, bruk av omformere i elektrifisering av plattformer via HVDC eller HVAC-kabler, og drøfter til slutt kraftelektronikk som benyttes i vindturbiner.

2.1 Kraftelektronikk ved tilknytting av HVDC og HVAC til oljeplattform

Kraftelektronikk har en sentral rolle i elektrifisering av oljeplattformer, og i flere av de dominerende generatorteknologiene i en vindpark. AC/DC-omformere er en nødvendighet i alle HVDC-anlegg, og stadig flere vindturbinprodusenter benytter frekvensomformere i sine generatorer. Det benyttes i dag hovedsakelig to teknologier for frekvensomformere. Den tradisjonelle strømstyrte omformeren, eller ”current source converter” (CSC), er det billigste alternativet og den har minst tap. Begrensingene til CSC er at den krever et sterkt AC-nett for å fungere, og den tar mye plass. Dette gjør at den ikke er så attraktiv i offshore applikasjoner. Spenningsmatet omformer, også kalt ”voltage source converter” (VSC), har bedre egenskaper. Figur 1 viser en prinsippskisse av VSC. Dagens teknologi muliggjør overføring av maksimalt 1200 MW ved en spenning på ± 320 kV [6].

VSC baserer seg på transistorer av typen IGBT. Med en svitsjefrekvens på 1-2 kHz er det mulig å oppnå rask kontroll og et minimum av lavfrekvente harmoniske komponenter. Videre har VSC den fordelen at den kan styre aktiv og reaktiv effekt uavhengig av hverandre, og den har bedre egenskaper under feil i AC-nettet. Valg av kontrollstrategier er sterkt tilpasset bruksområdet, og generelt er VSC en svært fleksibel komponent i kraftsystemet.

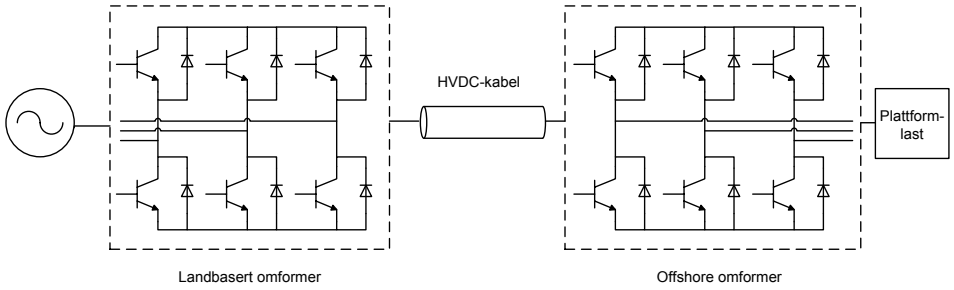

Figur 1: Voltage Source Converter i HVDC-system

Tilknyttning av kraft fra land gjennom HVDC-kabel, hvor omformerene er av CSC-type omtales med et samlebegrep ”HVDC Classic”. Det er to teknologier som benytter VSC, ”HVDC Light™” og ”HVDC Plus™” [7].

Figur 2 viser en prinsippskisse av kostnader ved å elektrifisere en plattform med kraft fra land. HVDC har større oppstartskostnader på grunn av omformere. HVAC blir dyrest for lange avstander på grunn av problemer knyttet til reaktiv kompensering. Krysningspunktet er avhengig av avstand fra land, frekvens på plattformen, plass på plattform og kostnader. For korte avstander, og kraftoverføring mellom 30-50 MVA kan HVAC anses som den mest kostandseffektive løsningen. For de lengste avstandene benyttes HVDC [8]. Krysningspunktet ligger vanligvis rundt 50-100km.

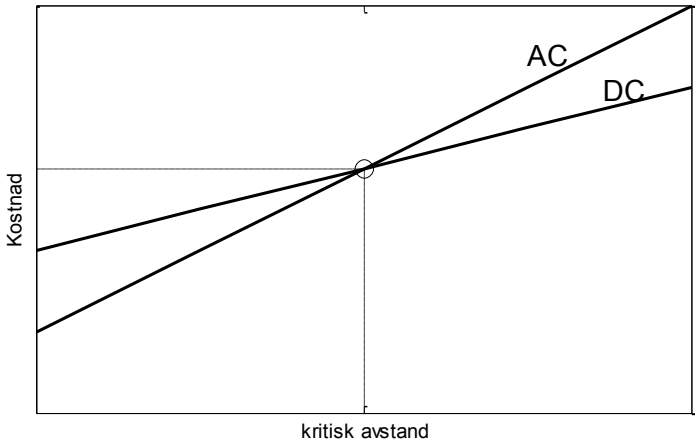

Figur 2: Kostnad for HVAC vs. HVDC

”HVDC Classic”-teknologi ble brukt da den 240 km lange HVDC-kabelen mellom Kristiansand i Norge til Tjele i Danmark ble lagt i 1977 [9]. Denne teknologien ble også benyttet da den 580 km lange HVDC-kabelen ble lagt mellom Norge og Nederland, i NorNed-prosjektet [10].

HVDC Light™ har blitt brukt til forsyning av flere eksisterende plattforminstallasjoner, blant annet til elektrifisering av kompressorer på Troll A-plattformen i 2005 [11]. Da Valhallfeltet ble elektrifisert ble det bygget en ny plattform for omformeren, som gjorde elektrifisering gjennom HVDC Light™ mulig [12].

HVAC har nylig blitt brukt til elektrifisering av den nye offshore installasjonen Gjøa [13], og er planlagt for Goliatfeltet [13].

2.2 Kraftelektronikk i Offshore Vindparker

Direkte tilkoblede induksjonsgeneratorer er enkel og etablert teknologi i vindturbiner, men de har sine begrensinger i offshore vindkraft. For det første er det ønskelig å kunne variere rotorens omdreiningshastighet med vindfarten. Dette gir høyere effekt ved moderat vind, og beskytter det mekaniske systemet under feil. Videre er det ønskelig med en teknologi som har mer styrbarhet mot kraftnettet. Girboks i vindturbiner trenger mye vedlikehold, og må skiftes ut flere ganger i løpet av levetiden. En generator med et tilstrekkelig antall poler gjør et mekanisk girsystem overflødig.

Permanent magnet synkron generator (PMSG) med en frekvensomformer mellom turbinrotor og nett løser problemene nevnt over. Omformeren gir mulighet til å variere generatorfrekvensen og dermed omdreiningshastigheten til rotoren uavhengig av nettfrekvensen. En omformer av typen VSC gir en ekstra frihetsgrad til en rask kontroll av reaktiv effekt til nettet. Det er mulig å benytte frekvensomformere på både induksjonsgeneratorer og vanlige synkrongeneratorer, men PMSG er valgt for å fjerne girboksen fra systemet.

3 SYSTEMBESKRIVELSE

I denne artikkelen studeres to måter å elektrifisere en plattform på. I system 1 forsynes plattformen med kraft fra land og system 2 er et isolert system med plattform tilknyttet en offshore vindpark. Se Figur 3 og 4 for systemskisser. Systemene har utspring i to masteroppgaver ved NTNU.

Synkrongeneratorer med gassturbiner dekker vanligvis oljeplattformers kraftbehov alene. Eksiterings- og governorsystem regulerer henholdsvis spenningen på generatorterminalene og frekvensen i systemet [14]. Ved tilknytting av ekstern kraft er det ønskelig at synkrongeneratorens kraftproduksjon er så liten som mulig, på denne måten minimeres plattformens CO_2-utslipp.

Frekvensen på plattformsystemet som studeres er 60 Hz, noe som er ganske vanlig i Nordsjøen siden mange av plattformene har hatt amerikanske operatorer.

Lasten på plattformen som er studert består hovedsakelig av en stor induksjonsmotor som er å betrakte som en akkumulert modell, og en liten passiv last som representerer lys og servicefunksjoner.

Se avsnitt 6 for verdier for spenning og merkeeffekter.

3.1 System 1: Elektrifisering fra land

System 1 er basert på et lignende system studert i [15]. Ulik frekvens på land og på plattform gjør en frekvensomformer nødvendig. VSC plasseres i dette tilfellet på land, og plattformen forsynes med HVAC-kabler, se Figur 3 for systemskisse. Dette gir kontrollmulighetene som VSC-HVDC introduserer, samtidig som den ikke tar opp plass på plattformen.

Simuleringene fokuserer på å vise systemets svakheter før VSC-kontroll er implementert, og simuleringsmodellen består av en stiv spenningskilde på land, tilknyttet plattformen gjennom en HVAC-kabel.

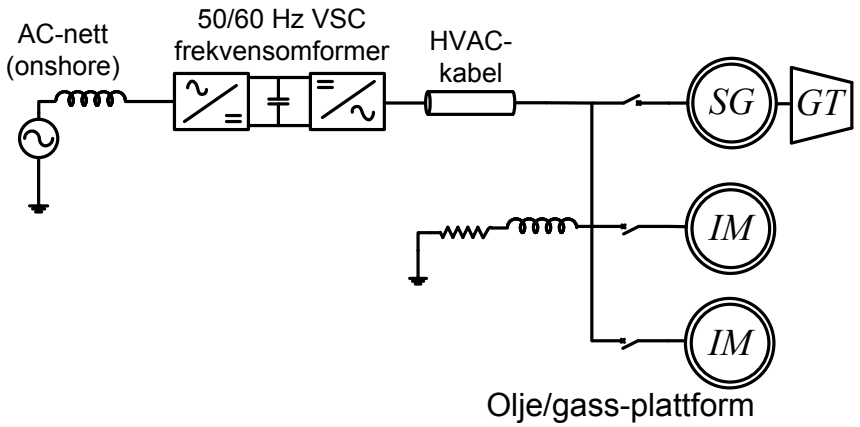

Figur 3: System 1, Elektrifisering av plattform med kraft fra land

3.2 System 2: Elektrifisering fra offshore vindpark

Systemet er basert på [16]. En offshore vindpark er koblet til en oljeplattform uten forbindelse til land som vist i Figur 4. Dette gir flere utfordringer. Energiproduksjonen fra en vindpark er variabel og vanskelig å kontrollere. Gassturbinene med sine synkrongeneratorer må balansere aktiv og reaktiv effekt for å unngå for store avvik i spenning og frekvens.

Simuleringene som presenteres skal illustrere kontrollmulighetene i vindturbinene sine frekvensomformere. De har mulighet til rask kontroll av reaktiv effekt uavhengig av aktiv effektflyt. Kontrollen er implementert med spennings-droop (V-

droop), der vindturbinene leverer reaktiv effekt proporsjonalt med avviket mellom terminalspenning og en referansespenning [17].

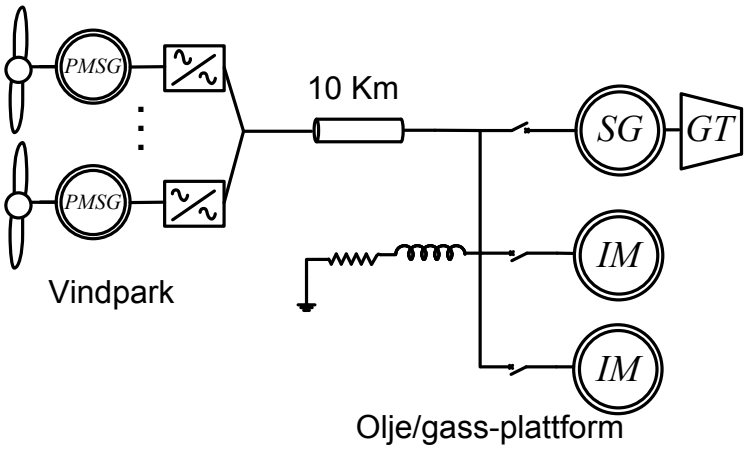

Figur 4: System 2, Elektrifisering fra offshore vindpark

4 SIMULERINGER

System 1 og 2 er modellert i henholdsvis MATLAB® Simulink™ SimPowerSystems™ og PSCAD®. Under følger simuleringsresultater fra hvert system. For system 1 simuleres tap av synkrongenerator. For system 2 simuleres start av en stor direktekoblet induksjonsmotor på plattformen.

4.1 System 1: Frakobling av synkrongenerator

En akkumulert modell av induksjonsmaskiner og en liten passiv last drives på plattformen som initielt er i stasjonær tilstand. Synkrongeneratoren på plattformen frakobles ved t = 4 s. Systemet som simuleres har HVAC-kabler på henholdsvis 10 km, 50 km og 80 km. Figur 5 viser spenningsendringene på plattformen før, under og etter frakobling av synkrongeneratoren.

For alle lengdene på HVAC-kabelen viser resultatene tydelig at spenningsfallet på plattformen etter tap av synkrongenerator er høyere enn hva som aksepteres av IEC-standarden gitt i [18]. Dette betyr at det være nødvendig med en

form for kontroll av spenningsnivået på plattformen ved en eventuell frakobling av synkrongeneratoren.

Elektromagnetisk moment for induksjonsmaskiner er tilnærmet proposjonalt med spenning [19]. Et spenningsfall vil dermed medføre at induksjonsmotoren får et lavere elektromagnetisk moment. For kabelen på 10 km stabiliserer induksjonsmotoren seg på et lavere mekanisk og elektromagnetisk moment, som fremdeles er innenfor et akseptabelt arbeidsområde for motoren. På tross av dette er spenningen for lav i følge [18]. Når kabelen er 50 km og 80 km er spenningsfallet så stort at induksjonsmotoren ikke greier å opprettholde et elektromagnetisk moment som kan drive motorlasten. Dette gjør at motoren bremses ned og stopper.

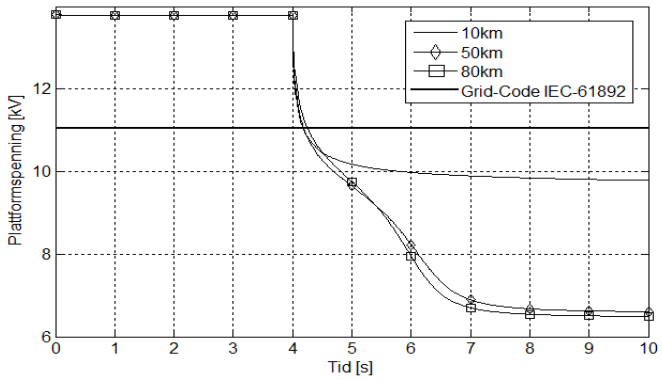

Figur 5: Frakobling av synkrongenerator i system 1

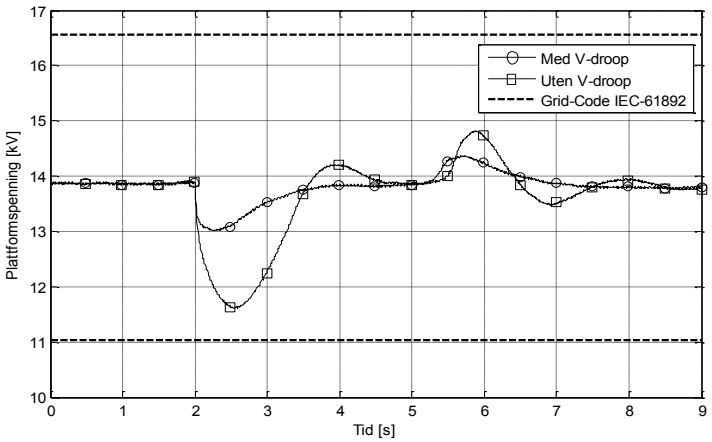

Figur 6: Motorstart med og uten V-droop i system 2

4.2 System 2: Motorstart

En direkte tilkoblet 5 MW induksjonsmotor blir startet i systemet som er vist i Figur 4. Figur 6 viser simuleringer med og uten V-droop i vindturbinene. Resultatene viser en stor reduksjon i spennings-transienten under oppstart når V-droop er implementert. VSC-omformere har kortere tidsforsinkelser enn AVR-eksiteringssytem, slik at de responderer fortere under forstyrrelser. Begge resultatene er innenfor grensene til offshore grid-code for transiente forstyrrelser [18], men start av en noe større motor kan gi problemer for tilfellet uten V-droop.

5 KONKLUSJON

For å redusere CO_2-utslippene fra gassturbiner som benyttes til elektrisitetsproduksjon på oljeplattformer, må andre og renere kilder tilknyttes. I denne artikkelen har forsyning med HVAC-kabler tilkoblet land og kraft fra offshore vindkraft blitt studert.

Artikkelen påpeker hvordan kraftelektronikk muliggjør elektrifisering av oljeplattformer, og kan bidra til et mer driftssikkert elektrisk system.

Simuleringene av system 1 viser at kraftelektronikk er helt nødvendig for kontroll av plattformspenning og aktiv og reaktiv effektforsyning hvis plattformens synkrongenerator faller ut eller kobles fra. Simuleringene viser også hvordan spenningsfallet på plattformen varierer med lengden på HVAC-kablene.

Simuleringene av system 2 viser at spenningsvariasjoner ved direkte start av induksjonsmotor reduseres betraktelig hvis reaktiv effektkompensasjon implementeres i vindturbinens frekvensomformer.

En kombinasjon av tilknyttning av kraft fra land til plattform, og kraft fra offshore vindpark til plattform vil kunne eliminere behovet for synkrongeneratoren på plattformen, og dermed redusere utslipp ved elektritetsproduksjon ytteligere gjennom at kraft fra land er produsert fra fornybare energikilder.

Et studie av et slik kombinert system foreslås som fremtidig arbeid, hvor samordning mellom kraftelektronikk er nødvendig for kontroll av spenning og frekvens i systemet.

6 VEDLEGG

Table 6-1, Systemverdier brukt ved simulering

	Verdi	**Enhet**
Plattformspenning	13,8	kV
Synkrongenerator merkeeffekt, system 1	20	MVA
Synkrongenerator merkeeffekt, system 2	50	MVA
Stor induksjonsmotor merkeeffekt	28	MVA
Induksjonsmotor brukt til motorstart	5	MVA
Passiv last	2	MW

Et typisk plattformsystem i nordsjøen er i størrelsesorden 20 MVA og opp mot 100 MVA.

7 TAKK TIL

Forfatterene ønsker å takke PhD-studentene Sverre Skalleberg Gjerde og Raymundo Torres-Olguin, samt Dr.Eng Jan Wiik (ABB) for deres støtte ved utarbeiding av prosjektene og artikkelen.

8 REFERANSER

[1] O. L. (OLF), "Elkraft fra land til norsk sokkel," 2003.

[2] Regjeringen. (2006-2007, 2011-01-31). *Stortingsmelding nummer 34, Om norsk klimapolitikk*.

[3] K.-o. forurensningsdirektoratet. (2010, 02.17). *Gjøteborgprotokollen*. Available: http://www.miljostatus.no/Tema/Luftforurensning/Sur-nedbor/Goteborgprotokollen/

[4] NVE. (2011, 2011-01-31). *Vindkraft*. Available: http://www.nve.no/no/Konsesjoner/Konsesjonssaker/Vindkraft/

[5] G. J. W. He, T. Anderson, F. Olsen, T. Hanson, M. Korpås, T. Toftevaag, J. Eek, K. Uhlen, E. Johansson, "The Potential of Integrating Wind Power with Offshore Oil and Gas Platforms," Sintef Energy Research, T2010.

[6] ABB. (2010, 16.02.2011). *HVDC Light is the most interesting power transmission system developed for several decades*. Available: http://www.abb.com/industries/us/9AAC30300394.aspx

[7] R. Rudervall*, et al.*, "High voltage direct current (HVDC) transmission systems technology review paper," *Energy week,* pp. 7–8, 2000.

[8] N. Hörle*, et al.*, "Electrical supply for offshore installations made possible by use of VSC technology," in *Cigré 2002 Conference*, Paris, France, 2002.

[9] ABB. (2011). *Skagerrak 1-3 HVDC Interconnections* Available: http://www.abb.com/industries/ap/db0003db004333/e9c890cb41ffa3d5c125774a0044be37.aspx

[10] ABB. (2008, 17.02.11). *The NorNed HVDC Connection, Norway – Netherlands*. Available: http://www05.abb.com/global/scot/scot245.nsf/veritydisplay/2402665447f2d054c12571fb00333968/$file/project%20norned%20450%20kv%20dc%20mi%20sub.pdf

[11] ABB. (2010, 22.11.2010). *Power from shore: ABB technologies at Troll A platform* Available: http://www.abb.cl/industries/ap/db0003db004333/8c3aa401373d6f9cc125774a0049a015.aspx

[12] S. Gilje and L. Carlsson, "Valhall Re-development project, power from shore," Energex, 2006.

[13] ABB. (2010, 04.12.2010). Submarine Power Cables, Cables for offshore platforms and wind farms. Available: http://www05.abb.com/global/scot/scot245.nsf/veritydisplay/796660a22284a381c125777c00448c08/$File/Submarine%20power%20cables%20for%20offshore%20wind%20farms%20and%20platforms%202GM5010-gb%20oil%20rev%202010-08.pdf

[14] P. Kundur, *Power System Stability and Control*: McGraw-Hill Professional 1994.

[15] K. M. Høvik, "Study on Shore Converter Operated in Parallel with Platform Synchronous Generator," NTNU, Institute of Electric Power Engineering, Department of Energy Conversion, Trondheim2010.

[16] A. R. Årdal, "Modeling and Simulation of an offshore wind farm connected to an oil platform as an islanded system," NTNU, Institute of Electric Power Engineering, Department of Energy Conversion, Trondheim2010.
[17] F. Katiraei and M. R. Iravani, "Power Management Strategies for a Microgrid With Multiple Distributed Generation Units," *Power Systems, IEEE Transactions on,* vol. 21, pp. 1821-1831, 2006.
[18] IEC, "IEC 61892: Mobile and Fixed Offshore Units," in *Internasjonal grid-code*: IEC, 2010.
[19] J. Stephen, *Chapman, Electric Machinery Fundamentals*: McGraw-Hill, 2005.